

---

# Chapter 2

---

# MTI Radar

---

**William W. Shrader**

*Shrader Associates, Inc.*

**Vilhelm Gregers-Hansen**

*Naval Research Laboratory*

---

## 2.1 PREFACE

---

This chapter addresses surface-based radars; e.g., radars sited on land or installed onboard ships. For airborne radar, rapid platform motion has a significant effect on design and performance as discussed in Chapters 3, 4, and 5 of this *Handbook*.

The fundamental theory of moving target indication (MTI) radar, as presented in the previous editions of the *Radar Handbook*, has not materially changed. The performance of MTI radar, however, has been greatly improved, due primarily to four advances: (1) increased stability of radar subsystems such as transmitters, oscillators, and receivers; (2) increased dynamic range of receivers and analog-to-digital converters (A/D); (3) faster and more powerful digital processing; and (4) better awareness of the limitations, and therefore requisite solutions, of adapting MTI systems to the environment. These four advances have made it practical to use sophisticated techniques that were considered, and sometimes tried, many years ago but were impractical to implement. Examples of early concepts that were well ahead of the available technology were the velocity indicating coherent integrator (VICI)<sup>1</sup> and the coherent memory filter (CMF).<sup>2,54</sup>

Although these improvements have enabled much improved MTI capabilities, there are still no perfect solutions to all MTI radar problems, and the design of an MTI system is still as much of an art as it is a science. Examples of current problems include the fact that when receivers are built with increased dynamic range, system instability limitations will cause increased clutter residue (relative to system noise) that can cause false detections. Clutter maps, which are used to prevent false detections from clutter residue, work quite well on fixed radar systems, but are difficult to implement on, for example, shipboard radars, because as the ship moves, the aspect and range to each clutter patch changes, creating increased residues after the clutter map. A decrease in the resolution of the clutter map to counter the rapidly changing clutter residue will preclude much of the interclutter visibility (see later in this chapter), which is one of the least appreciated secrets of successful MTI operation.

MTI radar must work in the environment that contains strong fixed clutter, birds, bats and insects, weather, automobiles, and ducting. The ducting, also referred to as *anomalous propagation*, causes radar returns from clutter on the surface of the Earth to appear

### 2.1

at greatly extended ranges, which exacerbates the problems with birds and automobiles, and can also cause the detection of fixed clutter hundreds of kilometers away.

The clutter models contained in this chapter are approximations of the types of clutter that must be addressed. The exact quantitative data, such as precise spectrum and amplitude of each type of clutter, or the exact number of birds or point reflectors (e.g., water towers or oil-well derricks) per unit area, is not important, because the MTI radar designer must create a robust system that will function well no matter the actual deviation from the clutter models of real clutter encountered.

MTI radars may use rotating antennas or fixed apertures with electronic beam scanning (phased arrays). The rotating antenna may use a continuous waveform processed through either a finite-impulse-response (FIR) filter or an infinite-impulse-response (IIR) filter, or may use a batch waveform consisting of coherent processing intervals (CPIs) that are processed in FIR filters in groups of  $N$  pulses. (The term *MTI filter*, used often in this chapter, is a generic nomenclature that includes both FIR and IIR filters.) The finite time-on-target dictates the need for a batch processing approach.

There are many different combinations of successful MTI techniques, but any specific MTI radar system must be a total concept based on the parameters of the antenna, transmitter, waveform, signal processing, and the operational environment.

A number of plan-position-indicator (PPI) photographs, taken years ago, are included in this chapter to provide a better understanding of the environment that is difficult to appreciate with many modern radars. These photographs show MTI operation, birds, insects, and ducting better than can be described in words.

Attention is especially directed to the final section in this chapter, “Considerations Applicable to MTI Radar Systems,” which provides insight into both hardware and environmental lessons learned during many decades of MTI system development.

## 2.2 INTRODUCTION TO MTI RADAR

---

The purpose of MTI radar is to reject returns from fixed or slow-moving unwanted targets, such as buildings, hills, trees, sea, and rain, and retain for detection or display signals from moving targets such as aircraft. Figure 2.1 shows a pair of photographs of a PPI, which illustrates the effectiveness of such an MTI system. The distance from the center to the edge of the PPI is 40 nmi. The range marks are at 10-nmi intervals. The picture on the left is the normal video display, showing mainly the fixed-target returns. The picture on the right shows the effectiveness of the MTI clutter rejection. The camera shutter was left open for three scans of the antenna; thus, aircraft show up as a succession of three returns. MTI radar utilizes the doppler shift imparted on the reflected signal by a moving target to distinguish moving targets from fixed targets. In a pulse radar system, this doppler shift appears as a change of phase of received signals between consecutive radar pulses. Consider a radar that transmits a pulse of radio frequency (RF) energy that is reflected by both a building (fixed target) and an airplane (moving target) approaching the radar. The reflected pulses return to the radar a certain time later. The radar then transmits a second pulse. The reflection from the building occurs in exactly the same amount of time, but the reflection from the moving aircraft occurs in less time because the aircraft has moved closer to the radar in the interval between transmitted pulses. The precise time that it takes the reflected signal to reach the radar is not of fundamental importance. What is significant is whether the time changes between pulses. The time change, which is of the order of a few nanoseconds for an aircraft target, is determined by comparing the phase of the received signal with

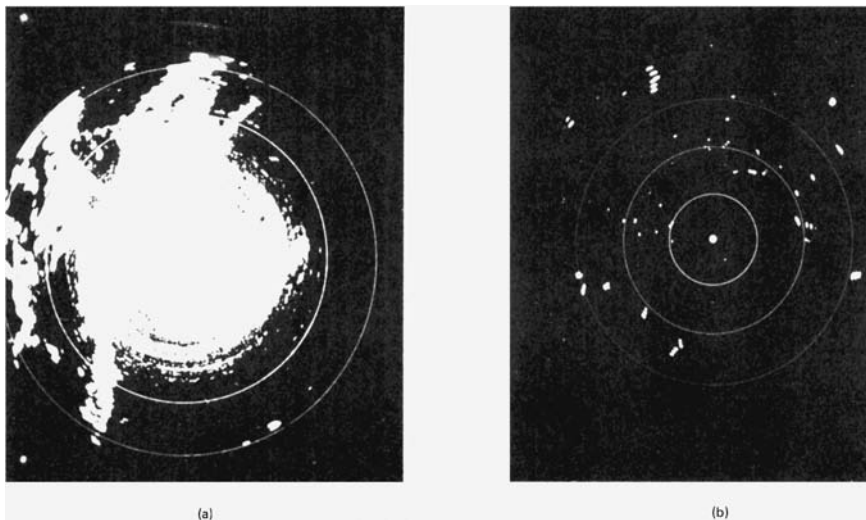


**FIGURE 2.1** (a) Normal video and (b) MTI video: These PPI photographs show how effective an MTI system can be. Aircraft appear as three consecutive blips in the right-hand picture because the camera shutter was open for three revolutions of the antenna. The PPI range is 40 nmi.

the phase of a reference oscillator in the radar. If the target moves between pulses, the phase of the received pulse changes.

Figure 2.2 shows a simplified block diagram of a coherent MTI system. The RF oscillator feeds the pulsed amplifier, which transmits the pulses. The RF oscillator

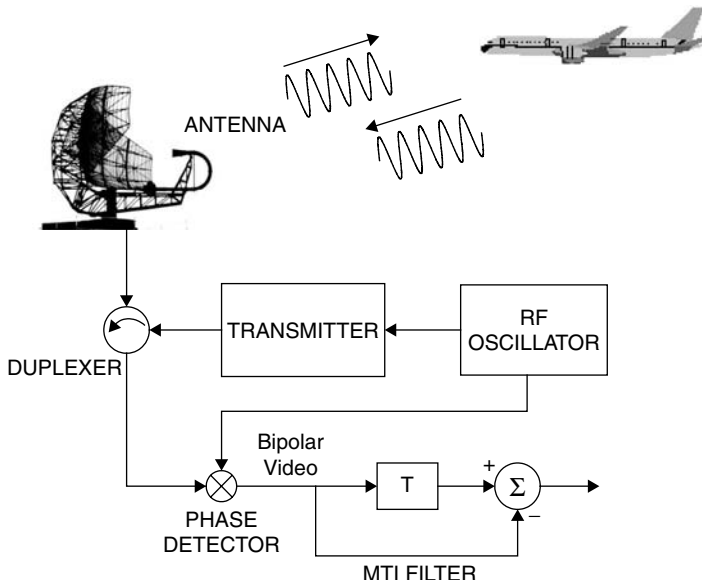


**FIGURE 2.2** Simplified block diagram of a coherent MTI system.

is also used as a phase reference for determining the phase of reflected signals. The phase information is stored in a pulse repetition interval (PRI) memory for the period,  $T$ , between transmitted pulses, and is subtracted from the phase information from the current received pulse. There is an output from the subtractor only when a reflection has occurred from a moving target.

**Moving-Target Indicator (MTI) Block Diagram.** A more complete block diagram of an MTI radar is shown in Figure 2.3. This block diagram is representative of a modern air traffic control radar operating at L or S band with a typical interpulse period of 1–3 ms and a CW pulse length of a few  $\mu\text{s}$  when the transmitter employs a vacuum tube amplifier such as, for example, a klystron, or tens of  $\mu\text{s}$  for a pulse compression waveform when a solid-state transmitter is used. The received signals are amplified in a low-noise amplifier (LNA) and subsequently downconverted through one or more intermediate frequencies (IF) by mixing with stable local oscillators. A bandpass IF limiter at the receiver output protects the A/D converter from damage but also prevents limiting from taking place in the A/D converter. In early MTI systems, the IF limiter served the purpose of deliberately restricting the dynamic range to reduce clutter residues at the MTI output. The received signals are then converted into in-phase and quadrature components (I & Q) through the A/D converter, either using a pair of phase detectors or through direct sampling as discussed in Section 2.13. The in-phase (I) and quadrature (Q) outputs are a function of the amplitude and phase of the IF signal and

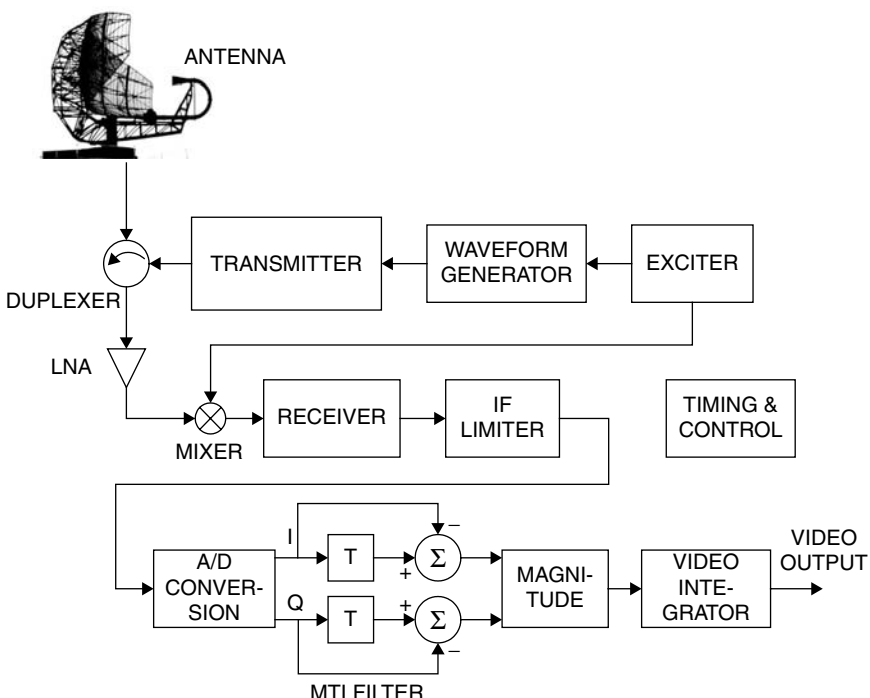
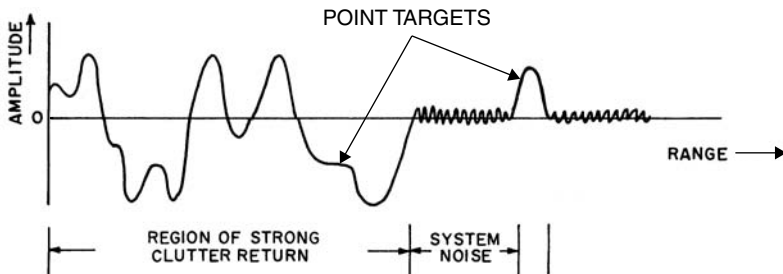


FIGURE 2.3 MTI system block diagram



**FIGURE 2.4** Bipolar video: return from single transmitter pulse

have in the past been referred to as bipolar videos, but a more correct terminology is that of the complex envelope of the received signals. An example of such a bipolar video (either I or Q), received from a single transmitted pulse and including both clutter and point targets is sketched in Figure 2.4. If the point targets are moving, the superimposed bipolar video from several transmitted pulses would appear as in Figure 2.5.

The remainder of the block diagram in Figure 2.3 shows the remaining processing required so that the moving targets can be displayed on a PPI or sent to an automatic target extractor. The in-phase and quadrature outputs from the A/D converter are stored in a PRI memory and also subtracted from the output from the previous transmitted pulse. This implementation represents the most basic two-pulse MTI canceler implemented as a finite impulse response (FIR) filter. As discussed in Section 2.8, MTI cancelers used in practical radars use higher-order filters, and these are sometimes implemented as infinite impulse response (IIR) filters.

The output of the subtractors is again a bipolar signal that contains moving targets, system noise, and a small amount of clutter residue if the clutter cancellation is not perfect. The magnitudes of the in-phase and quadrature signals are then computed ( $\sqrt{I^2 + Q^2}$ ) and converted to analog video in a digital-to-analog (D/A) converter for display on a PPI. The digital signal may also be sent to automatic target detection circuitry. The dynamic range (peak signal to rms noise) is limited to about 20 dB for a PPI display.

A key distinction, sometimes lost in the complexities of the systems that follow, is that an MTI radar system eliminates fixed clutter because the phase of signals returned from consecutive transmitted pulses do not (appreciably) change. The fixed clutter is removed after as few as two transmitted pulses by the subtraction process described

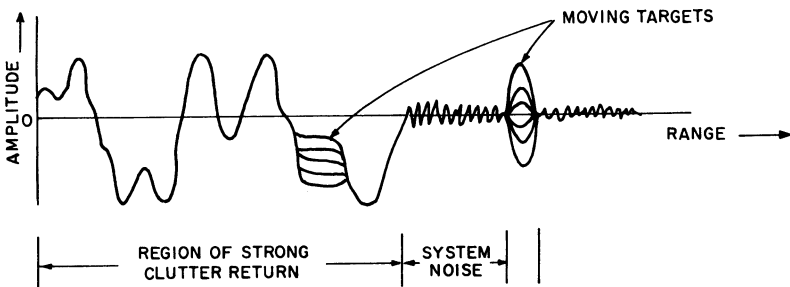


**FIGURE 2.5** Bipolar video: from consecutive transmitted pulses

above, even if each transmitted pulse has frequency modulation or other artifacts, as long as the artifacts are identical pulse-to-pulse. The point being made here is that MTI system operation does not depend on the frequency resolution of targets from clutter. To provide frequency resolution would require much longer dwell times on target than two pulses separated by a single PRI. Such extended dwell times is one of the fundamental characteristics of the moving target detector.

**Moving-Target Detector (MTD) Block Diagram.** Progress in digital signal processing technology by the mid-1970s made it practical for the first time to improve the performance of the classical MTI by (1) implementing a parallel bank of FIR filters to increase the output signal-to-clutter ratio and (2) replacing the IF limiter used in the past with a high-resolution clutter map for effective false alarm control. Although these concepts had been explored many years earlier using the Velocity Indicating Coherent Integrator (VICI)<sup>1</sup> or the Coherent Memory Filter (CMF)<sup>2,54</sup> to implement a doppler filter bank, and storage tubes or magnetic drum memory to implement clutter maps, it was the work at the MIT Lincoln Laboratory to improve the performance of airport surveillance radars that resulted in one of the first working examples of what has become known as the Moving Target Detection (MTD) radar.<sup>3,4</sup> The theory and expected benefits of this approach were described in two reports in 1972,<sup>5</sup> which provided the mathematical foundation for the understanding and the practical implementation of the MTD concept.

The predicted subclutter visibility improvement for the ASR-7 airport surveillance radar, when the three-pulse MTI processor was replaced by the second-generation MTD II processor, is shown in Figure 2.6.

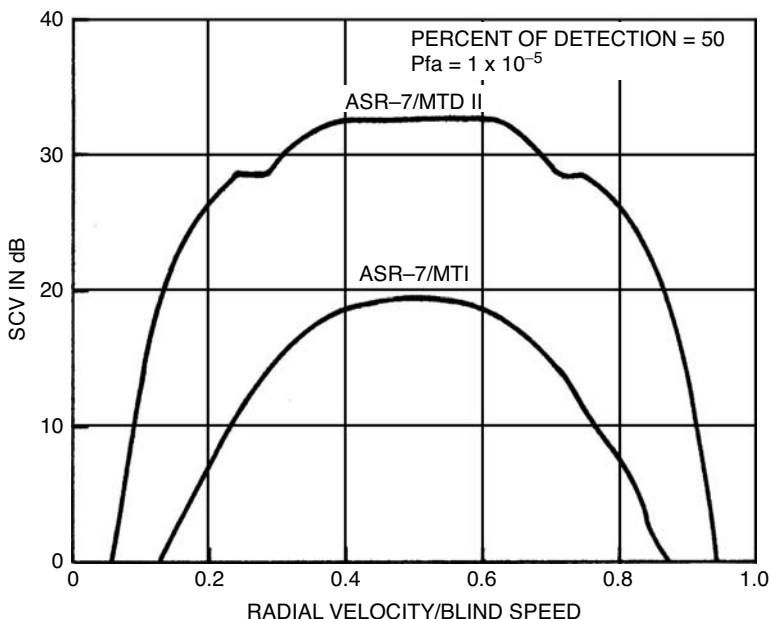
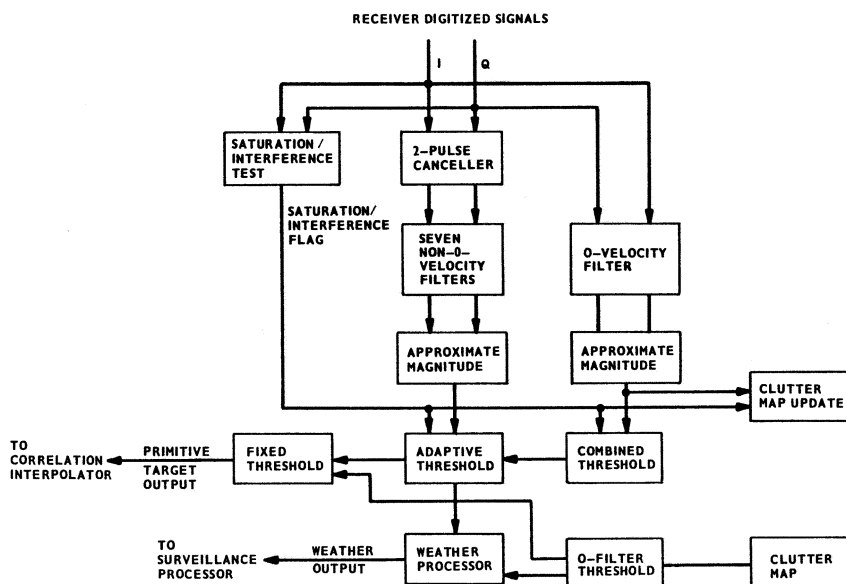


FIGURE 2.6 Subclutter visibility comparison between three-pulse MTI and MTD II

Part of this improvement was due to the use of doppler filter designs utilizing eight pulses, instead of just three for the MTI, and part was the result of allowing a larger dynamic range into the MTD processor and relying on a clutter map to suppress residues in regions where the clutter level exceeds the maximum clutter suppression of the radar.

The block diagram of the MTD II signal processor is shown in Figure 2.7. Parallel processing channels are provided for moving targets through the two-pulse MTI canceller and the seven-pulse doppler filter bank, and for nonmoving (“zero-doppler”) targets through the 0-Velocity Filter. A high resolution clutter map is built from the “0-Velocity Filter” output, and the clutter map content is used for thresholding in the two processing channels. In the moving target channel, the threshold obtained from the clutter map content is scaled down by the expected clutter attenuation. In addition to the clutter map thresholding, conventional constant false alarm rate thresholding is utilized against moving clutter (rain) and interference. Detection outputs, named *Primitive Target Outputs*, are obtained through this processing for each individual processed CPI. Figure 2.8 shows the additional processing required to generate centroided Target Reports and the processing of these Target Reports to obtain track outputs for display to the air traffic control system.

The MTD radar transmits a group of  $N$  pulses at a constant pulse repetition frequency (PRF) and at a fixed radar frequency. This set of pulses is usually referred to as the *coherent processing interval (CPI)* or *pulse batch*. Sometimes one or two additional fill pulses are added to the CPI in order to suppress range-ambiguous clutter returns, as might occur during periods of anomalous propagation. The returns received during one CPI are processed in the bank of  $N$ -pulse finite-impulse-response (FIR) filters. Then the radar may change its PRF and/or RF frequency and transmit another CPI of  $N$  pulses. Since most search radars are ambiguous in doppler, the use of different



**FIGURE 2.7** Block diagram of MTD II signal processor

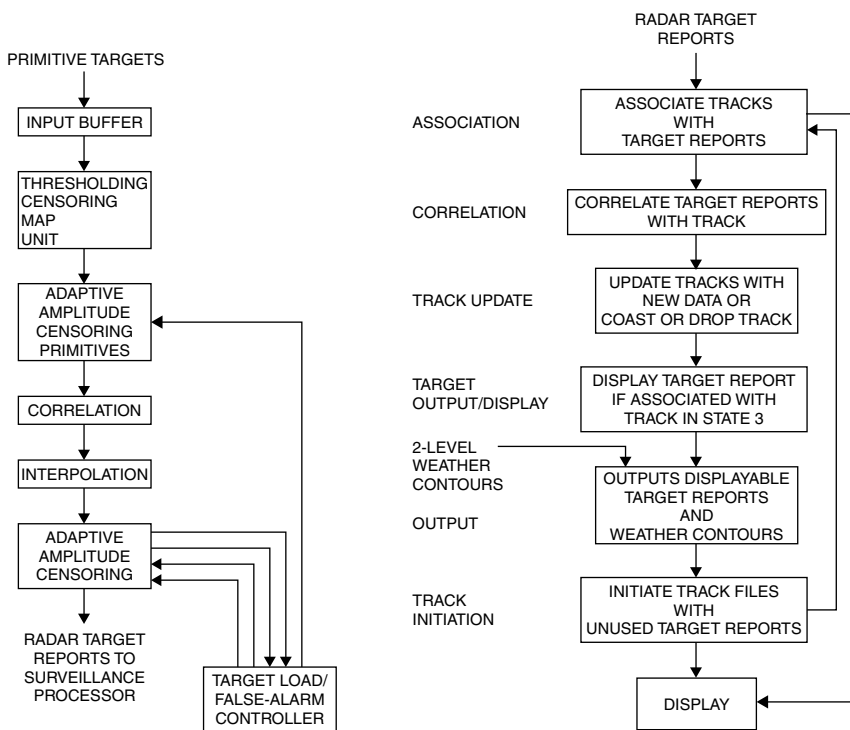


**FIGURE 2.8** Processing of Primitive Target detections and Radar Target Reports in MTD II

PRFs on successive coherent dwells will cause the target response to fall at different frequencies of the filter passband on the successive opportunities during the time on target, thus eliminating blind speeds.

Each doppler filter is designed to respond to targets in nonoverlapping portions of the doppler frequency band and to suppress sources of clutter at all other doppler frequencies. This approach maximizes the coherent signal integration in each doppler filter and provides clutter attenuation over a larger range of doppler frequencies than achievable with a single MTI filter. Thus, one or more clutter filters may suppress multiple clutter sources located at different doppler frequencies. An example of the use of an MTD doppler filter bank against simultaneous land and weather clutter ( $W_x$ ) is illustrated in Figure 2.9. It can be seen that filters 3 and 4 will provide significant suppression of both clutter sources.

The output of each doppler filter is envelope-detected and processed through a cell-averaging constant false alarm rate (CA-CFAR) processor to suppress residues due to range-extended clutter that may not have been fully suppressed by the filter.

As will be discussed later in this chapter, the conventional MTI detection system often relies on a carefully controlled dynamic range in the IF section of the radar receiver to ensure that clutter residues at the MTI output are suppressed to the level of the receiver noise or below. This limited dynamic range, however, has the undesirable effect of causing additional clutter spectral broadening, and the achievable clutter suppression is consequently reduced.

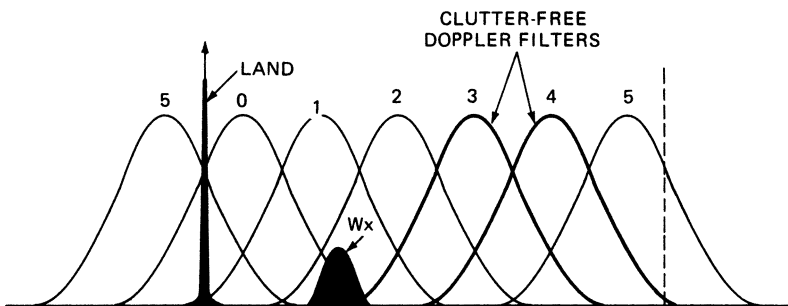


**FIGURE 2.9** Suppression of multiple clutter sources by using a doppler filter bank

In the MTD, one or more high-resolution clutter maps are used to suppress the clutter residues, after doppler filtering, to the receiver noise level (or, alternatively, to raise the detection threshold above the level of the residues). This in turn eliminates the need to restrict the IF dynamic range, which can then be set to the maximum value supported by the A/D converters. Thus, a system concept is obtained that provides a clutter suppression capability that is limited only by the radar system stability, the dynamic range of the receiver-processor, and the spectrum width of the returns from clutter. The concept of a high-resolution digital clutter map to suppress clutter residues is related to earlier efforts to construct analog area MTI systems using, for example, storage tubes.

Also included in the MTD implementation are "...area thresholds maintained to control excessive false alarms, particularly from bird flocks. Each area of about 16 square nautical miles is divided into several velocity regions. The threshold in each region is adjusted on each scan to achieve the desired limit on false alarms without raising the threshold so high that small aircraft are prevented from being placed in track status."<sup>4</sup>

In subsequent sections, specific aspects of the design of an MTD system will be discussed. Thus, Section 2.10 will discuss the design and performance of doppler filter banks, and a detailed discussion of clutter maps will follow in Section 2.15. Since the original work at Lincoln Laboratory to develop the MTD concept, a number of MTD systems have been developed that vary in detail from the original concept. Also, the use of clutter maps to inhibit excessive clutter residue, instead of controlling clutter residue with intentionally restricted dynamic range, has been adopted in newer MTI systems.

### 2.3 CLUTTER FILTER RESPONSE TO MOVING TARGETS

---

The response of an MTI system to a moving target varies as a function of the target's radial velocity. For the MTI system described above, the response, normalized for unity noise power gain, is shown in Figure 2.10. Note that there is zero response to stationary targets and also to targets at  $\pm 89$ ,  $\pm 178$ ,  $\pm 267$ , . . . knots. These speeds, known as *blind speeds*, are where the targets move 0,  $1/2$ , 1,  $1\frac{1}{2}$ , . . . wavelengths between consecutive transmitted pulses. This results in the received signal being

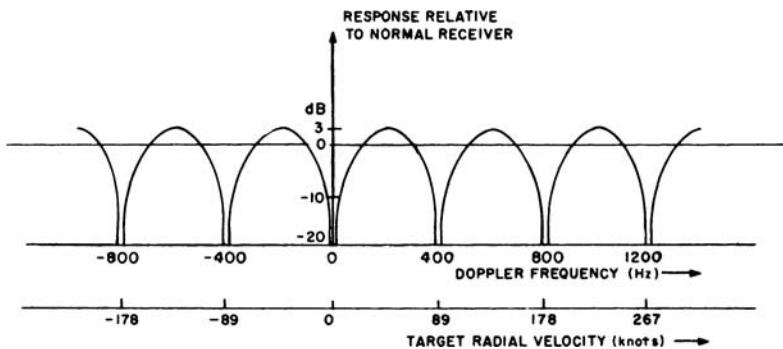


**FIGURE 2.10** MTI system response for 1300-MHz radar operating at 400 pps

shifted precisely  $360^\circ$  or multiples thereof between pulses, which results in no change in the phase-detector output. The blind speeds can be calculated

$$V_B = k \cdot \frac{\lambda \cdot f_r}{2} \quad k = \pm 0, 1, 2, \dots \quad (2.1)$$

where  $V_B$  is the blind speed, in meters per second;  $\lambda$  is the transmitted wavelength, in meters; and  $f_r$  is the PRF, in hertz. A convenient set of units for this equation is

$$V_B \text{ (knots)} = k \cdot \frac{0.29 \cdot f_r}{f_{\text{GHz}}} \quad k = \pm 0, 1, 2, \dots \quad (2.2)$$

where  $f_r$  is the PRF (pulse repetition frequency) in hertz; and  $f_{\text{GHz}}$  is the transmitted frequency, in gigahertz. Note from the velocity response curve that the response to targets at velocities midway between the blind speeds is greater than the response for a normal receiver.

The abscissa of the velocity response curve can also be labeled in terms of doppler frequency. The doppler frequency of the target can be calculated from

$$f_d = \frac{2 \cdot V_R}{\lambda} \quad (2.3)$$

where  $f_d$  is the doppler frequency, in hertz;  $V_R$  is the target radial velocity, in meters per second; and  $\lambda$  is the transmitted wavelength, in meters. It can be seen from Figure 2.10 that the doppler frequencies for which the system is blind occur at multiples of the pulse repetition frequency.

## 2.4 CLUTTER CHARACTERISTICS

The clutter suppression needed from an MTI or MTD radar depends on the characteristics of the clutter environment, the specific radar target detection requirements, and the major radar design characteristics such as range and angle resolution as well as operating frequency. The ability of a radar to suppress clutter is determined by radar

waveform and processing, available dynamic range, and the overall radar system stability. In this section, some of the key characteristics of radar clutter and its influence on MTI radar design will be summarized.

**Spectral Characteristics.** The spectral characteristics of clutter, as discussed in most references, implicitly assumes that the radar transmits a continuous, constant PRF waveform. The spectrum of the output of a pulsed transmitter using a simple rectangular pulse of length  $\tau$  is shown in Figure 2.11. The spectral width of the  $(\sin U)/U$  envelope is determined by the transmitted pulse width, the first nulls occurring at a frequency of  $f_0 \pm 1/\tau$ . The individual spectral lines are separated by a frequency equal to the PRF. These spectral lines fall at precisely the same frequencies as the nulls of the MTI filter response shown in Figure 2.10. Thus, a canceler will, in theory, fully reject clutter with this ideal line spectrum. In practice, however, the spectral lines of the clutter returns are broadened by motion of the clutter (such as windblown trees or waves on the sea surface) as well as by the motion of the antenna in a scanning radar or due to platform motion. This spectral spread prevents perfect cancellation of clutter in an MTI system.

Often, in the past, the assumption has been made that the returns from clutter have a gaussian power spectral density, which may be characterized by its standard deviation  $\sigma_v$  and mean velocity  $m_v$ , both in units of m/s.<sup>6</sup> Using this gaussian model, each of the spectral lines in Figure 2.11 will be convolved with the spectrum:

$$S_G(f) = \frac{1}{\sqrt{2\pi}\sigma_f} \cdot \exp\left(-\frac{(f - m_f)^2}{2\sigma_f^2}\right) \quad (2.4)$$

This spectrum is normalized to have unit power, and the velocity parameters have been converted to Hz using the doppler equation:

$$\begin{aligned} m_f &= \frac{2 \cdot m_v}{\lambda} \\ \sigma_f &= \frac{2 \cdot \sigma_v}{\lambda} \end{aligned} \quad (2.5)$$

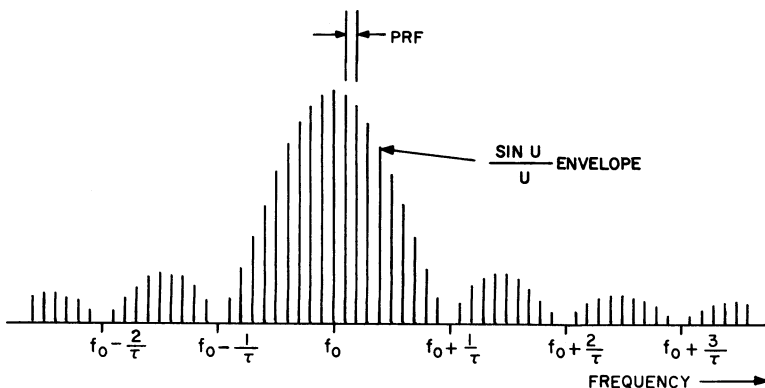


FIGURE 2.11 Pulse transmitter spectrum

## 2.12

## RADAR HANDBOOK

where  $\lambda$  is the radar wavelength. Instead of the standard deviation  $\sigma_f$ , the power spectrum can be defined by its 3-dB width  $B_3$ , as follows:

$$S_G(f) = \frac{\sqrt{4 \cdot \ln(2)}}{\sqrt{\pi} \cdot B_3} \cdot \exp\left(-\frac{4 \cdot \ln(2) \cdot f^2}{B_3^2}\right) \quad (2.6)$$

where

$$B_3 = \sqrt{8 \cdot \ln(2)} \cdot \sigma_f = 2.3548 \cdot \sigma_f \quad (2.7)$$

The early experimental results that led to the general adoption of the gaussian model<sup>6</sup> were obtained with radar equipment of limited stability, and the spectral shape was sometimes derived from video spectra computed using square-law detected returns.

By the mid-1970s, new experimental results were obtained,<sup>7,8</sup> which showed that the spectrum fall-off was slower than predicted by the gaussian model. This led to new models based on polynomial representations of the spectrum using an equation of the form:

$$S_{\text{POLY}}(f) = \frac{n \cdot \sin\left(\frac{\pi}{n}\right)}{\pi \cdot B_3} \cdot \frac{1}{1 + \left(\frac{2|f|}{B_3}\right)^n} \quad (2.8)$$

The spectrum shape is determined by the integer  $n$ , which must be 4 or larger in order for the two first spectral moments to exist. A typical value used for this spectrum is  $n = 4$  which results in

$$S_{\text{POLY}}(f) = \frac{\sqrt{8}}{\pi \cdot B_3} \cdot \frac{1}{1 + \left(\frac{2|f|}{B_3}\right)^4} \quad (2.9)$$

The relationship between the standard deviation of this spectrum and its 3-dB width is given by

$$B_3 = 2 \cdot \sigma_f \quad (2.10)$$

A potential issue with this model is that the skirts of the spectrum correspond to very large radial velocity components of the clutter internal motion.

During the 1990s, an extensive measurement program conducted at the MIT Lincoln Laboratory obtained more accurate data on land clutter spectra using a very stable radar equipment and data was collected under well-controlled conditions.<sup>9</sup> These new results led to the following exponential model for land clutter spectra:

$$S_{\text{EXP}}(f) = \frac{\ln(2)}{B_3} \cdot \exp\left(-\frac{2 \cdot \ln(2)}{B_3} \cdot |f|\right) \quad (2.11)$$

Here the 3-dB spectrum width can be expressed in terms of the standard deviation by

$$B_3 = \sqrt{2} \cdot \ln(2) \cdot \sigma_f = 0.9803 \cdot \sigma_f \quad (2.12)$$

Billingsley<sup>9</sup> used the parameters  $g$ ,  $v_c$ , and  $\beta$ , respectively, for the gaussian, the polynomial, and the exponential spectrum models. In addition, the exponent  $n$  is needed for the polynomial model. These parameters were chosen to simplify the functional description of the spectrum shape. In terms of the standard deviation of the spectral width in m/s, these parameters can be defined as follows:

$$\begin{aligned} g &= \frac{1}{2 \cdot \sigma_v^2} && - \text{gaussian spectrum} \\ v_c &= \sqrt{2 \cdot \ln(2)} \cdot \sigma_v && - \text{polynomial spectrum with } n = 4 \\ \beta &= \frac{\sqrt{2}}{\sigma_v} && - \text{exponential spectrum} \end{aligned} \quad (2.13)$$

Assuming a value of  $\sigma_v = 0.25$  m/s, corresponding to windy condition, the three-clutter spectrum models are compared in Figure 2.12. As noted in Billingsley<sup>9</sup> all three models are in reasonable agreement for the upper 30–40 dB of their range but differ appreciably at the lower values of clutter spectral density.

Estimated values of the spectral spread of land clutter from forested regions and for different wind speeds are shown in Table 2.1. The values in the table are based on Billingsley's parameter  $\beta$ , but columns have been added with the corresponding rms spectral spread in m/s. An example of a measured land clutter spectrum is shown in Figure 2.13. The spectral shape parameter  $\beta$  can be estimated as the slope of the (upper) skirt of the spectrum in dB per m/s divided by  $10/\ln(10)$ . These values of  $\beta$  were added in this figure.

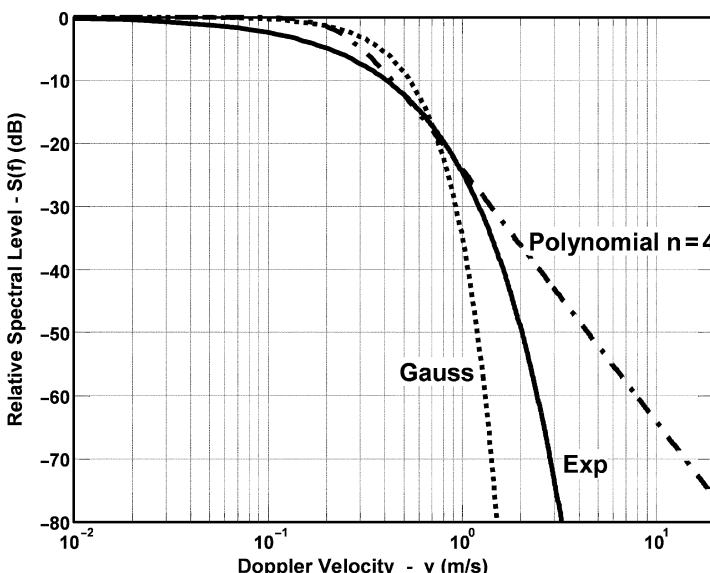


**FIGURE 2.12** Comparison of gaussian, exponential, and polynomial spectra for an rms spectral spread of  $\sigma_v = 0.25$  m/s

**TABLE 2.1** Measured Spectral Spread for Different Wind Conditions (after J.B.Billingsley<sup>9</sup>  
© William Andrew Publishing Inc. 2002)

Wind Conditions	Wind Speed (mph)	Exponential ac Shape Parameter $\beta$ (m/s) <sup>-1</sup>		RMS Spectral Width $\sigma_v$ (m/s)	
		Typical	Worst Case	Typical	Worst Case
Light air	1–7	12	—	0.12	—
Breezy	7–15	8	—	0.18	—
Windy	15–30	5.7	5.2	0.25	0.27
Gale force (est.)	30–60	4.3	3.8	0.33	0.37

The values of rms spectral spread of land clutter as derived from the data in Billingsley<sup>9</sup> agree quite well with previous studies. It can probably safely be stated that the polynomial model of land clutter spectra is far too pessimistic at spectral values below -40 dB and should be avoided for radar analysis requiring a large clutter attenuation value.

The case for the exponential model, as presented by Billingsley, is quite convincing, and this model has been widely accepted as being the most accurate for radar performance predictions.

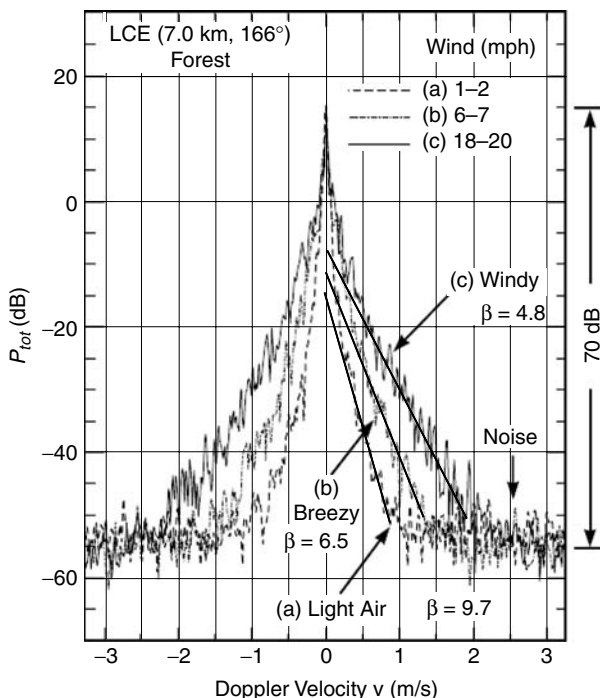


**FIGURE 2.13** Measured spectra of clutter from forest. Several wind speeds and an estimated value of  $\beta$  have been added. (after J.B. Billingsley<sup>9</sup>  
© William Andrew Publishing Inc. 2002)

A comparison between the gaussian and the exponential models on a linear scale, as shown in Figure 2.14, indicates that the difference in spectral width at even very low levels ( $-80$  dB) is no more than about a factor of 2. For many analyses, this would most likely be insignificant compared to the added clutter spectral spreading caused by scanning modulation. Thus, in many cases, the simple gaussian model can continue to be used in MTI and MTD performance analysis. In case of doubt, the spectral spread of the gaussian model could be doubled to assess the available margin.

Nathanson and Reilly<sup>10</sup> have shown that the clutter spectral width of rain is primarily due to a turbulence and wind shear (change in wind velocity with altitude). Measurements show a typical average value of  $\sigma_{vt} = 1.0$  m/s for turbulence and  $\sigma_{vs} = 1.68$  m/(s/km) for wind shear. A convenient equation is  $\sigma_{vs} = 0.04 \cdot R \cdot \theta_{el}$  m/s for the effect of wind shear, provided the rain fills the vertical beam. Here  $R$  is the range to the weather, in nautical miles, and  $\theta_{el}$  is the one-way half-power vertical beamwidth, in degrees. Thus, for example,  $\sigma_{vs}$  of rain viewed at 25 nmi with a vertical beamwidth of  $4^\circ$  would be  $\sigma_{vs} = 4.0$  m/s. The total spectral spread is then  $\sigma_v = \sqrt{\sigma_{vt}^2 + \sigma_{vs}^2} = \sqrt{1.0^2 + 4.0^2} = 4.1$  m/s. Rain and chaff also have an average velocity, in addition to the spectral spread noted above, which must be taken into account when designing an MTI system.

The clutter spectral width in meters per second is independent of the radar frequency. The standard deviation of the clutter power spectrum  $\sigma_f$ , in hertz, is

$$\sigma_f = \frac{2 \cdot \sigma_v}{\lambda} \quad \text{Hz} \quad (2.14)$$

where  $\lambda$  is the transmitted wavelength, in meters; and  $\sigma_v$  is the clutter standard deviation, in meters per second.

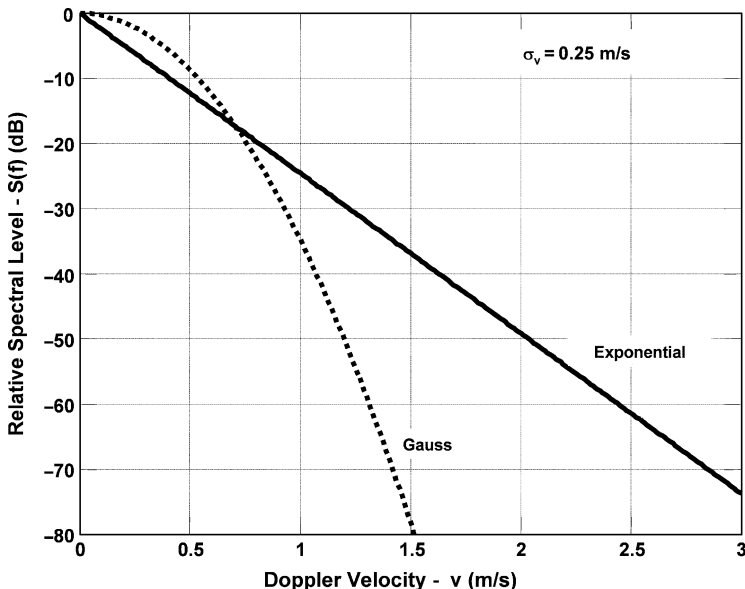


FIGURE 2.14 Comparison of gaussian and exponential spectra on linear velocity scale

Antenna scanning also causes a spread of the clutter power spectrum due to the amplitude modulation of the echo signals by the two-way antenna pattern.<sup>11</sup> The resulting clutter standard deviation is

$$\sigma_f = \frac{\sqrt{\ln 2}}{\pi} \cdot \frac{f_r}{n} = 0.265 \cdot \frac{f_r}{n} \text{ Hz} \quad (2.15)$$

where  $f_r$  is the PRF and  $n$  is the number of hits between the one-way 3-dB points of the antenna pattern. This equation was derived from a gaussian beam shape but is essentially independent of the actual beam shape or aperture illumination function used.

The clutter spectral spread due to scanning, normalized to the PRF, is

$$\sigma_f T = \frac{0.265}{n} \quad (2.16)$$

where  $T = 1/\text{PRF}$  is the interpulse period.

The combined spectral effects of internal clutter motion and antenna scanning modulation must be obtained as the convolution of the individual spectra. When both spectra are gaussian in shape, the resulting spectrum remains gaussian with a standard deviation that is the square-root of the sum of the squares of the individual standard deviations.

By integrating the two-sided tails of the gaussian and exponential spectra, outside a multiple,  $k$ , of the standard deviation of the spectra, a rough, but conservative, estimate can be found of how wide the MTI notch must be to achieve a required improvement factor  $I$ . Such a curve is shown in Figure 2.15 based on the clutter spectra shown in Figure 2.14. Although this approach would only be strictly correct for an ideal MTI filter with a step-function passband, it can serve as a preliminary guideline for the MTI filter design.

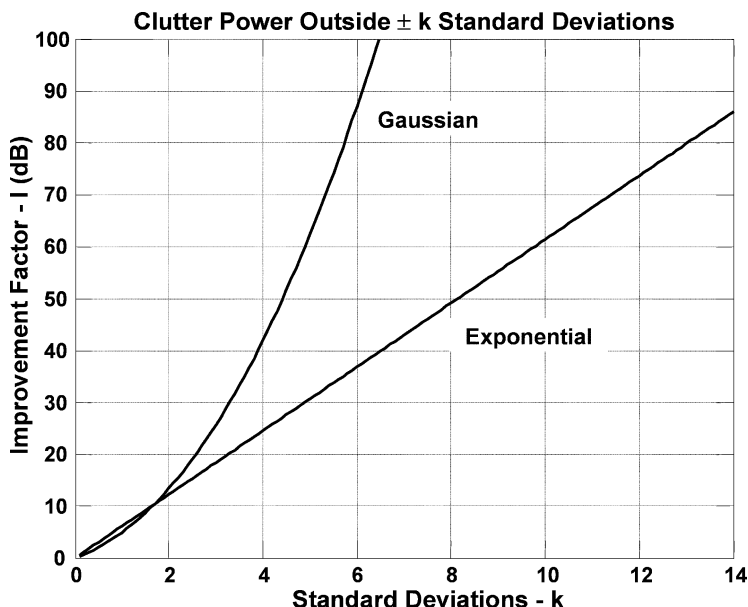


FIGURE 2.15 Clutter power in two-sided tails of spectrum vs. multiple of standard deviation

**Amplitude Characteristics.** To predict the performance of an MTI system, the power of the clutter returns with which a target must compete should be known. The amplitude of the clutter returns depends on the size of the resolution cell of the radar, the frequency of the radar, and the reflectivity of the clutter. The expected radar cross section of clutter can be expressed as the product of a reflectivity factor and the volume or area of the resolution cell.

For surface clutter, as viewed by a surface-based radar,

$$\bar{\sigma} = A_c \cdot \sigma^0 = R \cdot \theta_{az} \cdot \frac{c \cdot \tau}{2} \cdot \sigma^0 \quad (2.17)$$

where  $\bar{\sigma}$  is the average radar cross section, in square meters;  $A_c$  is the area of clutter illuminated, in square meters;  $R$  is the range to clutter, in meters;  $\theta_{az}$  is the one-way half-power azimuthal beamwidth, in radians;  $c$  is the speed of propagation, 300 million m/s;  $\tau$  is the half-power radar pulse length (after the matched filter), in seconds; and  $\sigma^0$  is the average clutter reflectivity factor, in square meters per square meter.

For volumetric clutter, such as chaff or rain, the average cross section is

$$\bar{\sigma} = V_c \cdot \eta = R \cdot \theta_{az} \cdot \theta_{el} \cdot H \cdot \frac{c \cdot \tau}{2} \cdot \eta \quad (2.18)$$

where  $V_c$  is the volume of clutter illuminated ( $m^3$ ) and  $\eta$  is the clutter reflectivity factor ( $m^2/m^3$ ). The volume  $V_c$  is computed from the height extent of clutter  $H$  (meters), the azimuth extent of the clutter  $R \cdot \theta_{az}$ , and the radar range resolution cell  $\tau$ . If the clutter completely fills the vertical beam, then  $H = R \cdot \theta_{el}$ , where  $\theta_{el}$  is the elevation beamwidth.  $R$  is the range to the clutter (meters) and  $c$  is the speed of propagation.

It should be noted that for land clutter  $\sigma^0$  can vary considerably from one resolution cell to the next. A typical distribution of  $\sigma^0$ , taken from Barton,<sup>12</sup> is shown in Figure 2.16. Typical values for  $\sigma^0$  and  $\eta$  from the same reference are given in Table 2.2. Additional results for clutter reflectivity are found in Billingsley.<sup>9</sup>

TABLE 2.2 Typical Values of Clutter Reflectivity\*

Clutter	Reflectivity, $\lambda$ , m $\eta, (m)^{-1}$	Conditions	Band $\lambda, m$	Clutter Parameters for Typical Conditions			
				L 0.23	S 0.1	C 0.056	X 0.032
Land (excluding point clutter)	$\sigma^0 = \frac{0.00032}{\lambda}$ (worst 10 percent)	.....	$\sigma^0$ dB	-29	-25	-22	-20
Point clutter	$\sigma = 10^4 m^2$	.....	$\sigma$ m <sup>2</sup>	$10^4$	$10^4$	$10^4$	$10^4$
Sea (Beaufort scale $K_B$ , angle $E$ )	$\sigma^0 dB = -64 + 6K_B + (\sin E)dB - \lambda dB$	Sea state 4 (6-ft waves, rough); $E = 1^\circ$	$\sigma^0$ dB	-51.5	-47.5	-44.5	-42.5
Chaff (for fixed weight per unit volume)	$\eta = 3 \times 10^{-8} \lambda$	.....	$\eta$ m <sup>-1</sup>	$7 \times 10^{-9}$	$3 \times 10^{-9}$	$1.7 \times 10^{-9}$	$10^{-9}$
Rain (for rate $r$ mm/h)	$\eta = 6 \times 10^{-14} r^{1.6} \lambda^{-4}$ (matched polarization)	$r = 4$ mm/h	$\eta$ m <sup>-1</sup>	$2 \times 10^{-10}$	$5 \times 10^{-9}$	$5 \times 10^{-8}$	$5 \times 10^{-7}$

\*From Barton<sup>12</sup>

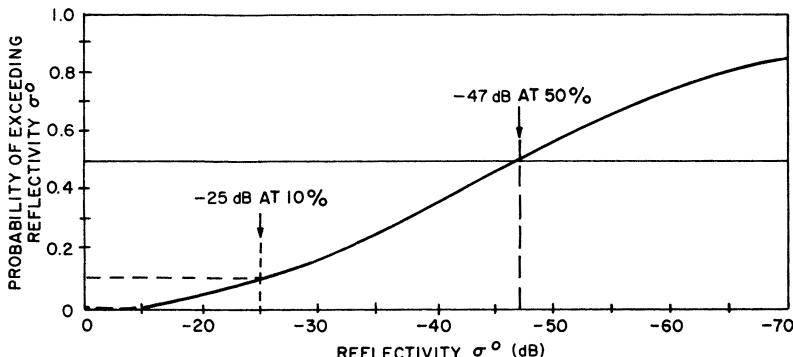


**FIGURE 2.16** Distribution of reflectivity for ground clutter typical of heavy clutter at S band (after D. K. Barton<sup>12</sup> © IEEE 1967)

Because of the imprecision in predicting  $\sigma^0$  and  $\eta$ , these equations do not include an antenna beam-shape factor. For the measurement of the reflectivity of rain, references on radar meteorology present more precise equations.<sup>13</sup>

In addition to distributed clutter targets, there are many targets that appear as *points*, such as radio towers, water tanks, and buildings. These point targets typically have a radar cross section of  $10^3$  to  $10^4 \text{ m}^2$  with typical densities as shown later in Figure 2.18. This graph is from Billingsley<sup>9</sup> and the additional points indicated by an asterisk are from Ward.<sup>14</sup>

Figure 2.17a shows a PPI display of all clutter observed with a surveillance radar with a  $1.3^\circ$  by  $2\text{-}\mu\text{s}$  resolution cell in the mountainous region of Lakehead, Ontario, Canada. (The PPI range is set for 30 nmi.) Clutter that exceeds the minimum-discriminable signal (MDS) level of the radar by 60 dB is shown in Figure 2.17b.

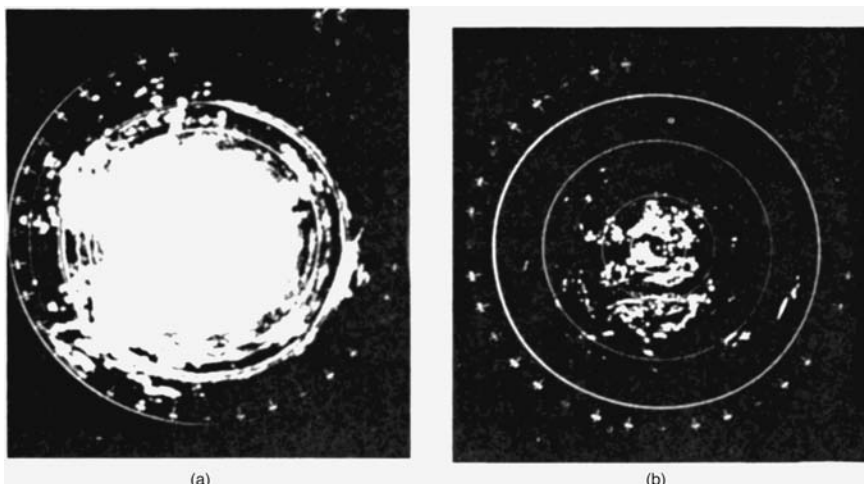


**FIGURE 2.17** PPI display, 30-nmi range of (a) all clutter at a mountainous site and (b) clutter that exceeds the system noise level by 60 dB

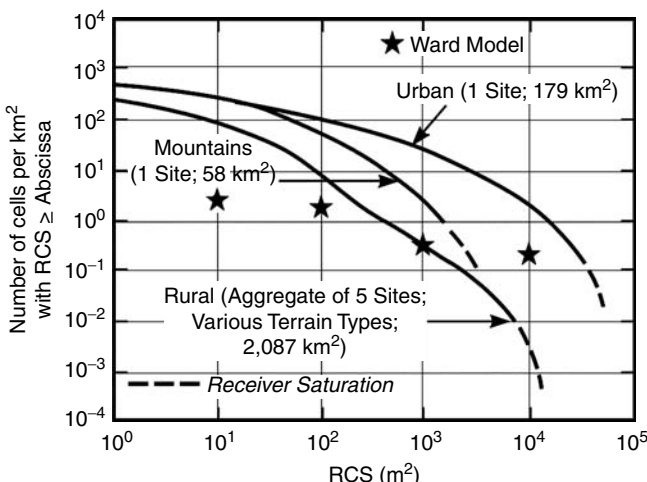


**FIGURE 2.18** Typical densities of point clutter scatterers (after J.B. Billingsley<sup>9</sup>)  
© William Andrew Publishing Inc. 2002)

Note that the clutter in Figure 2.17b is very spotty in character, including the strong fixed-point targets and returns from extended targets. It is significant that the extended targets are no longer very extended. The face of a mountain at 10 mi from 5 to 7 o'clock is only a line. If the MTI system were incapable of displaying an aircraft while it was over the mountain face, it would display the aircraft on the next scan of the antenna because the aircraft would have moved either farther or nearer. The PPI does not have a resolution that approaches the resolution of the signal processing circuits of this radar. Thus, the apparent extended clutter has many weak areas not visible in these photographs, where targets could be detected by virtue of an MTI radar's interclutter visibility (defined in Section 2.5).

## 2.5 DEFINITIONS

---

The IEEE Standard Radar Definitions<sup>15</sup> provide useful definitions for many of the quantities needed to quantify MTI and MTD performance, but in some cases, the vagueness of the original definition and the lack of distinction between performance against distributed clutter versus point clutter returns have led to ambiguous interpretations of several terms. In this section, the major definitions will be reviewed and annotated to attempt to clarify some of these potential ambiguities. For each term, the IEEE definition, when available, will be quoted along with a subsequent discussion.

**Improvement Factor** The IEEE definition of Improvement Factor reads:

**moving-target-indication (MTI) improvement factor:** The signal-to-clutter power ratio at the output of the clutter filter divided by the signal-to-clutter power ratio at the input to the clutter filter, averaged uniformly over all target radial velocities of interest. Synonym: **clutter improvement factor**.

This definition assumes that clutter is distributed homogeneously across many range cells. In this case, the above definition is equally valid before and after pulse compression. Against point clutter this definition only applies after pulse compression and may result in a different value of the improvement factor. The real difficulty with this definition is, however, the lack of a precise definition of the doppler velocity interval, which is to be used for the required “uniform” averaging. Originally, this averaging was assumed to involve multiple PRF intervals based on classical low PRF radars using a single MTI filter. It was for this reason that the MTI Improvement Factor definition (I) provided in the 2nd edition of this *Radar Handbook* used the noise gain of the doppler (MTI) filter as the normalizing factor. The increased use of pulse doppler filter banks in modern radar has, however, led to a use of the IEEE definition where the averaging of the signal-to-clutter ratio improvement is performed only across a narrow region around the peak of the doppler filter response. In this case, the coherent integration gain of the doppler filter is automatically added to the conventional MTI improvement factor value and much better radar performance is indicated.

Since a definition of clutter suppression is often needed, which quantifies the inherent radar stability limitations, apart from any additional coherent gain, it is sometimes preferable to use the IEEE definition of clutter attenuation. In this chapter, *improvement factor* and *clutter attenuation* will be used synonymously. When the coherent gain of the doppler filter is included, the term *signal-to-clutter ratio* improvement will be used.

### Clutter Attenuation

The IEEE definition reads

**clutter attenuation (CA):** In moving-target indication (MTI) or doppler radar, the ratio of the clutter-to-noise ratio at the input to the processor, to the clutter-to-noise ratio at the output. *Note:* In MTI, a single value of CA will be obtained, while in doppler radar the value will generally vary over the different target doppler filters. In MTI, CA will be equal to MTI improvement factor if the targets are assumed uniformly distributed in velocity. *See also: MTI improvement factor.*

Here, it will be assumed that “processor” refers to the MTI filter or a single doppler filter in a pulse doppler filter bank. Based on this definition, the clutter attenuation is given by

$$CA = \frac{P_{CIN}}{P_{COUT}} \cdot \frac{P_{NOUT}}{P_{NIN}} \quad (2.19)$$

where  $P_{CIN}$  and  $P_{COUT}$  are the clutter power at the input and output of the MTI filter, respectively, and  $P_{NIN}$  and  $P_{NOUT}$  are the corresponding noise powers. As noted in the IEEE definition, the value of CA will most likely differ from filter to filter in a doppler filter bank due to specific clutter and filter response characteristics.

In the discussion above, the assumption was implicitly made that clutter returns are stationary and distributed in range. The above definitions will be equally valid before and after pulse compression. For a single piece of point clutter, as often used in actual radar stability measurements, the definition of clutter attenuation would have to be changed as follows to provide identical results:

**clutter attenuation (CA), point clutter:** In moving-target indication (MTI) or Doppler radar, the ratio of the total energy in the received point clutter return at the input to the processor, to the total energy in the point clutter residue at the output of the processor, multiplied by the noise gain of processor.

The clutter attenuation against point clutter based on this definition will be the same before or after pulse compression and will also be identical to the value of CA obtained against distributed clutter with identical spectral characteristics.

For the practical measurement of CA against a single piece of point clutter (i.e., corner reflector), the total energy must be integrated, per the above definition, at the input and output of each doppler filter. The calculation of the energy is best performed prior to pulse compression since the precise duration of the uncompressed pulse, and therefore the integration window, is accurately known. If done after pulse compression, uncertainties in the integration of energy may arise due to the transient response of the pulse compression filter.

**Signal-to-Clutter Ratio Improvement ( $I_{SCR}$ )** For a system employing multiple doppler filters, such as the MTD, each doppler filter will also have a coherent gain,  $G_C(f)$ , which at the filter peak has a value  $G_{C,max}$ . The coherent gain of a doppler filter is equal to the increase in signal-to-thermal-noise ratio between the input and the output of the filter due to the coherent summation of individual target returns. Again these coherent gain values would usually differ from filter to filter due to potentially different doppler filter characteristics. These coherent gain values will include the filter mismatch loss but not the straddling losses between adjacent filters. The product of the clutter attenuation,  $CA_i$ , and the coherent gain,  $G_{C,max,i}$ , for the  $i$ 'th doppler filter becomes the definition of the signal-to-clutter ratio (SCR) improvement:

$$I_{SCR,i} = CA_i \cdot G_{C,max,i} \quad (2.20)$$

This quantity was not included in the *IEEE Dictionary*,<sup>15</sup> but the following definition is commonly used:

**signal-to-clutter ratio improvement: ( $I_{SCR}$ )**: The ratio of the signal-to-clutter ratio obtained at the output of the doppler filter bank to the signal-to-clutter ratio at the input to the filter bank computed as a function of target doppler frequency.

This definition does not include any doppler averaging across the individual filters, and the definition does not provide a single figure of merit for a radar doppler processor because each filter may have different values of clutter attenuation and coherent gain.

Since each doppler filter has a coherent gain that is a function of target doppler, an average value of signal-to-clutter improvement can be defined by averaging all filters over its respective range of target dopplers:

$$\bar{I}_{SCR} = \frac{1}{f_N - f_0} \left[ \int_{f_0}^{f_1} CA_0 \cdot G_{C,0}(f) \cdot df + \int_{f_1}^{f_2} CA_1 \cdot G_{C,1}(f) \cdot df + \dots + \int_{f_{N-1}}^{f_N} CA_{N-1} \cdot G_{C,N-1}(f) \cdot df \right] \quad (2.21)$$

The specific frequencies could logically be chosen as the crossover between individual doppler filters. This calculation will now include the effect of a target doppler

straddling loss and would represent a single figure-of-merit for a doppler processor. To simplify this calculation the *average signal-to-clutter improvement* may be defined as the finite sum

$$\bar{I}_{\text{SCR}} = \frac{1}{N} \sum_{i=0}^{N-1} CA_i \cdot G_{C_{\max,i}} \quad (2.22)$$

to which the doppler straddling loss would have to be added.

### **Subclutter Visibility (SCV)**

The IEEE definition of subclutter visibility is

**Subclutter visibility:** The ratio by which the target echo power may be weaker than coincident clutter echo power and still be detected with specified detection and false-alarm probabilities.

*Note:* Target and clutter powers are measured on a single pulse return and all target velocities are assumed equally likely.

The subclutter visibility (SCV) of a radar system is a measure of its ability to detect moving-target signals superimposed on clutter signals. A radar with 20 dB SCV can detect an aircraft flying over clutter whose signal return is 100 times stronger. Note that it is implicitly assumed in the above definition that signal and clutter are both observed after pulse compression. The SCV of two radars cannot necessarily be used to compare their performance while operating in the same environment, because the target-to-clutter ratio seen by each radar is proportional to the size of the radar resolution cell and may be a function of frequency. Thus, a radar with a 10-μs pulse length and a 10° beamwidth would need 20 dB more subclutter visibility than a radar with a 1-μs pulse and a 1° beamwidth for equal performance in a distributed clutter environment.

The subclutter visibility of a radar, when expressed in decibels, is less than the improvement factor by the clutter visibility factor  $V_{oc}$  (see definition below).

### **Interclutter Visibility (ICV)**

The IEEE definition is

**interclutter visibility:** The ability of a radar to detect moving targets that occur in resolution cells among patches of strong clutter; usually applied to moving target indication (MTI) or pulsed-Doppler radars. *Note:* The higher the radar range and/or angle resolution, the better the interclutter visibility.

The interclutter visibility (ICV) of a radar is a measure of its capability to detect targets between points of strong clutter by virtue of the ability of the radar to resolve the areas of strong and weak clutter. A radar with high resolution makes available regions between points of strong clutter where the target-to-clutter ratio will be sufficient for target detection even though the SCV of the radar (based on average clutter) may be relatively low. To achieve ICV, a mechanism must be furnished to provide CFAR operation against the residue from strong clutter. This CFAR is provided in older MTI system by IF limiting and, in the MTD implementation, through the use of high-resolution clutter maps. A quantitative definition of interclutter visibility has not yet been formulated.

### **Filter Mismatch Loss**

The IEEE definition is

**filter mismatch loss:** The loss in output signal-to-noise ratio of a filter relative to the signal-to-noise ratio from a matched filter.

The maximum signal-to-noise ratio available from an  $N$ -pulse filter is  $N$  times the signal-to-noise ratio of a single pulse, assuming all pulses have equal amplitude. When weighting is applied to reject clutter and control the filter sidelobes, the peak output signal-to-noise ratio is reduced. The filter mismatch loss is the amount by which the peak-output signal-to-noise ratio is reduced by the use of weighting. A three-pulse MTI filter using binomial weights has a filter mismatch loss of 0.51 dB. The mismatch loss for the binomial-weighted four-pulse canceler is 0.97 dB.

**Clutter Visibility Factor ( $V_{oc}$ )** The IEEE definition is

**clutter detectability factor:** The predetection signal-to-clutter ratio that provides stated probability of detection for a given false alarm probability in an automatic detection circuit.

*Note:* In MTI systems, it is the ratio after cancellation or doppler filtering.

The clutter visibility factor is the ratio by which the target signal must exceed the clutter residue so that target detection can occur without having the clutter residue result in false-target detections. The system must provide a threshold that the targets will cross and the clutter residue will not cross.

## 2.6 IMPROVEMENT FACTOR CALCULATIONS

---

Using Barton's approach,<sup>17</sup> the maximum improvement factor  $I$  against zero-mean clutter with a gaussian-shaped spectrum for different implementations of the finite-impulse-response binomial-weight MTI canceler (see Section 2.8) is

$$I_1 \approx 2 \left( \frac{f_r}{2\pi\sigma_f} \right)^2 \quad (2.23)$$

$$I_2 \approx 2 \left( \frac{f_r}{2\pi\sigma_f} \right)^4 \quad (2.24)$$

$$I_3 \approx \frac{4}{3} \left( \frac{f_r}{2\pi\sigma_f} \right)^6 \quad (2.25)$$

where  $I_1$  is the MTI improvement factor for the single-delay coherent canceler;  $I_2$  is the MTI improvement factor for the dual-delay coherent canceler;  $I_3$  is the MTI improvement factor for the triple-delay coherent canceler;  $\sigma_f$  is the rms frequency spread of the gaussian clutter power spectrum, in hertz; and  $f_r$  is the radar repetition frequency, in hertz. When the values of  $\sigma_f$  for scanning modulation in Eq. 2.15 are substituted in the above equations for  $I$ , the limitation on  $I$  due to scanning is

$$I_1 \approx \frac{n^2}{1.39} \quad (2.26)$$

$$I_2 \approx \frac{n^4}{3.84} \quad (2.27)$$

$$I_3 \approx \frac{n^6}{16.0} \quad (2.28)$$

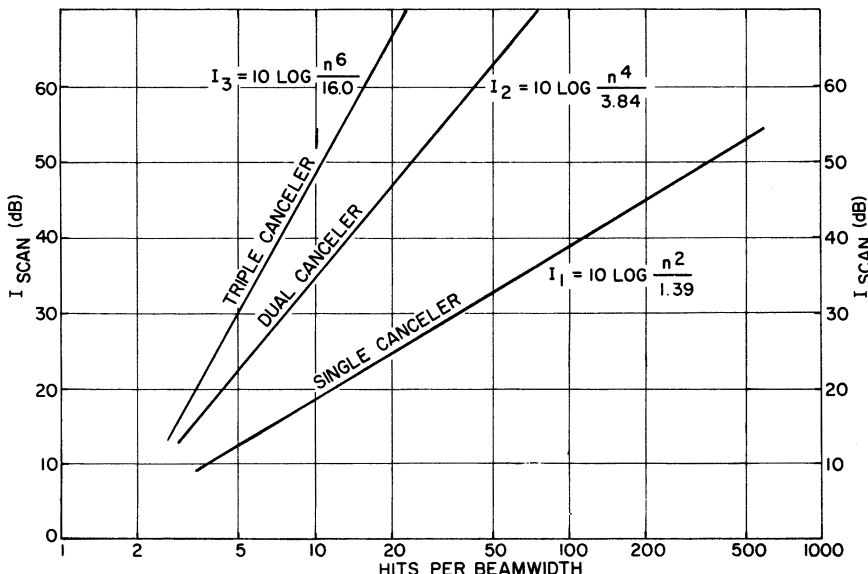


**FIGURE 2.19** Theoretical MTI improvement factor due to scan modulation: gaussian antenna pattern:  $n$  = number of pulses within the one-way half-power beamwidth

These relationships are shown graphically in Figure 2.19. This derivation assumes a linear system. That is, it is assumed that the voltage envelope of the echo signals, as the antenna scans past a point target, is identical to the two-way antenna voltage pattern. This assumption of a linear system may be unrealistic for some practical MTI systems with relatively few hits per beamwidth, however, as discussed in Section 2.11.

The scanning limitation does not apply to a system that can step-scan, such as a phased array. Note, however, that sufficient pulses must be transmitted to initialize the filter before useful outputs may be obtained. For example, with a three-pulse binomial-weight canceler, the first two transmitted pulses initialize the canceler, and a useful output is not available until after the third pulse has been transmitted. Feedback or infinite impulse response (IIR) filters would not be used with a step-scan system because of the long transient settling time of the filters.

The limitation on  $I$  due to internal-clutter fluctuations can be determined by substituting the appropriate value of  $\sigma_f$  into Eqs. 2.23 to 2.25. By letting  $\sigma_f = 2\sigma/\lambda$ , where  $\sigma_v$  is the rms velocity spread of the clutter, the limitation on  $I$  can be plotted for different types of clutter as a function of the wavelength  $\lambda$  and the pulse repetition frequency  $f_r$ . This is done for one-, two-, and three-delay binomial-weight cancelers in Figure 2.20, Figure 2.21, and Figure 2.22. The values of  $V_B$  given are the first blind speed of the radar (or where the first blind speed  $V_B$  would be for a staggered PRF system if staggering were not used). The improvement factor shown in these figures for rain and chaff is based on the assumption that the average velocity of the rain and chaff has been compensated for so that the returns are centered in the canceler rejection notch. Unless such compensation is provided, the MTI offers little or no improvement for rain and chaff.

Two further limitations on  $I$  are the effect of pulse-to-pulse repetition-period staggering combined with clutter spectral spread from scanning and internal-clutter motion.

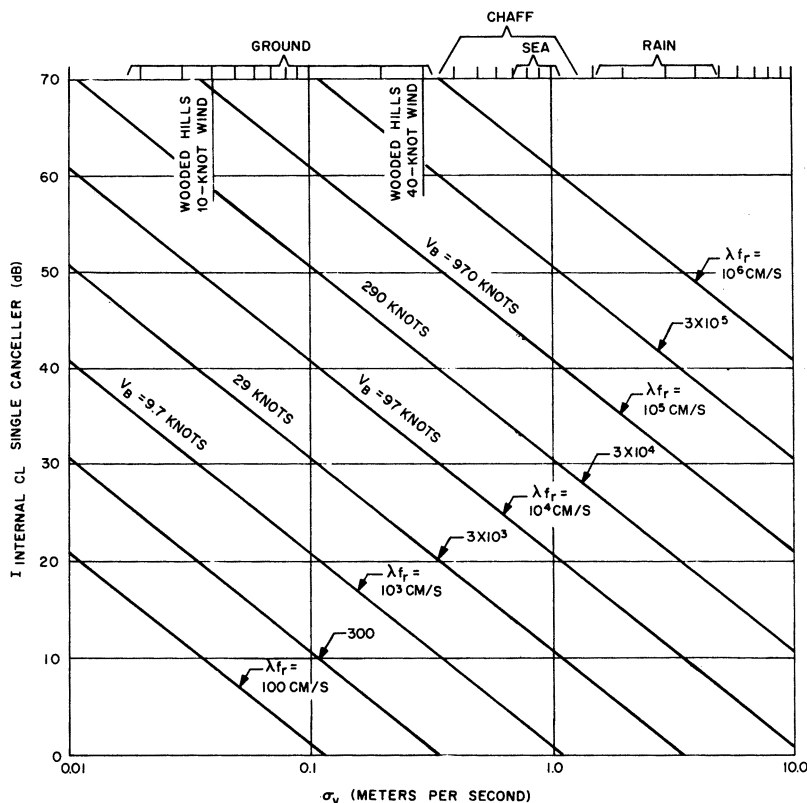


**FIGURE 2.20** MTI improvement factor as a function of the rms velocity spread of clutter for a two-pulse binomial-weight canceler

These limitations, plotted in Figure 2.23 and Figure 2.24, apply to all cancelers, whether single or multiple. (The derivation of these limitations and a means of avoiding them by the use of time-varying weights are given in "Stagger Design Procedures" in Section 2.8.)

## 2.7 OPTIMUM DESIGN OF CLUTTER FILTERS

The statistical theory of detection of signals in gaussian noise provides the required framework for the optimum design of radar clutter filters. Such theoretical results are important to the designer of a practical MTI or MTD system, in that they establish upper bounds on the achievable performance in a precisely specified clutter environment. It should be noted, however, that owing to the extreme variability of the characteristics of real clutter returns (power level, doppler shift, spectrum shape, spectral width, etc.) any attempt to actually approximate the performance of such optimum filters for the detection of targets in clutter requires the use of adaptive methods. The adaptive methods must estimate the unknown clutter statistics and

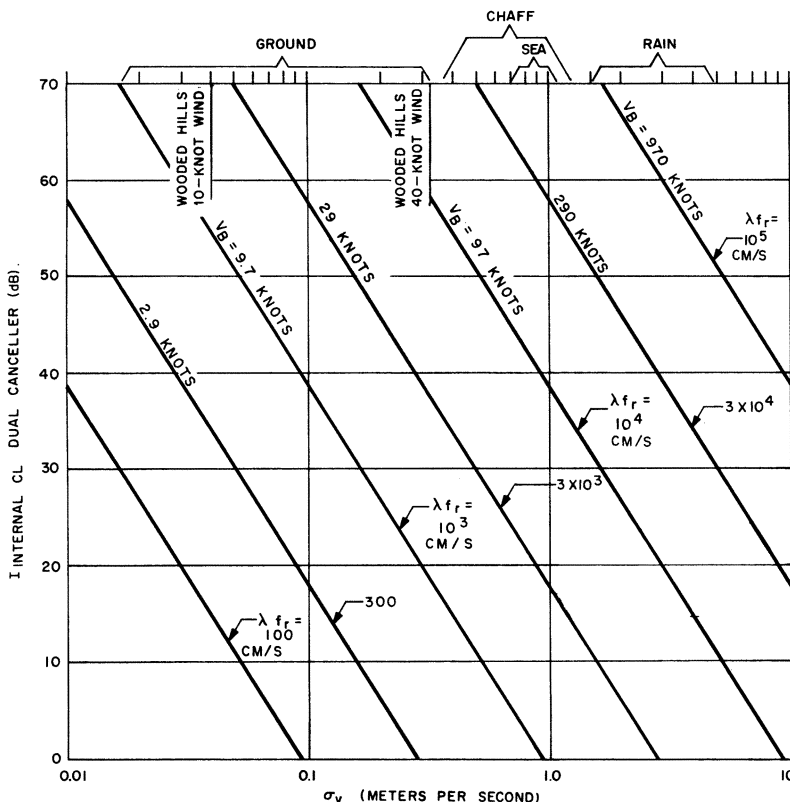


**FIGURE 2.21** MTI improvement factor as a function of the rms velocity spread of clutter for a three-pulse binomial-weight canceler

subsequently implement the corresponding optimum filter. An example of such an adaptive MTI system is discussed in Section 2.14.

For a single radar pulse with a duration of a few microseconds, the doppler shift due to aircraft target motion is a small fraction of the signal bandwidth, and conventional MTI and pulse doppler processing are not applicable. It is well known that the classical single-pulse “matched” filter provides optimum radar detection performance when used in a white-noise background. Against clutter returns that have the same spectrum as the transmitted radar pulse, the matched filter is no longer optimum, but the potential improvement in the output signal-to-clutter ratio by designing a modified optimized filter is usually insignificant.

When the duration of the transmitted radar signal, whether CW or a repetitive train of  $N$  identical pulses, is comparable with or greater than the reciprocal of anticipated target doppler shifts, the difference between a conventional white-noise matched filter (or coherent integrator) and a filter optimized to reject the accompanying clutter becomes significant. The characteristics of the clutter are characterized by the covariance matrix  $\Phi_C$  of the  $N$  clutter returns. If the power spectrum of the clutter is denoted

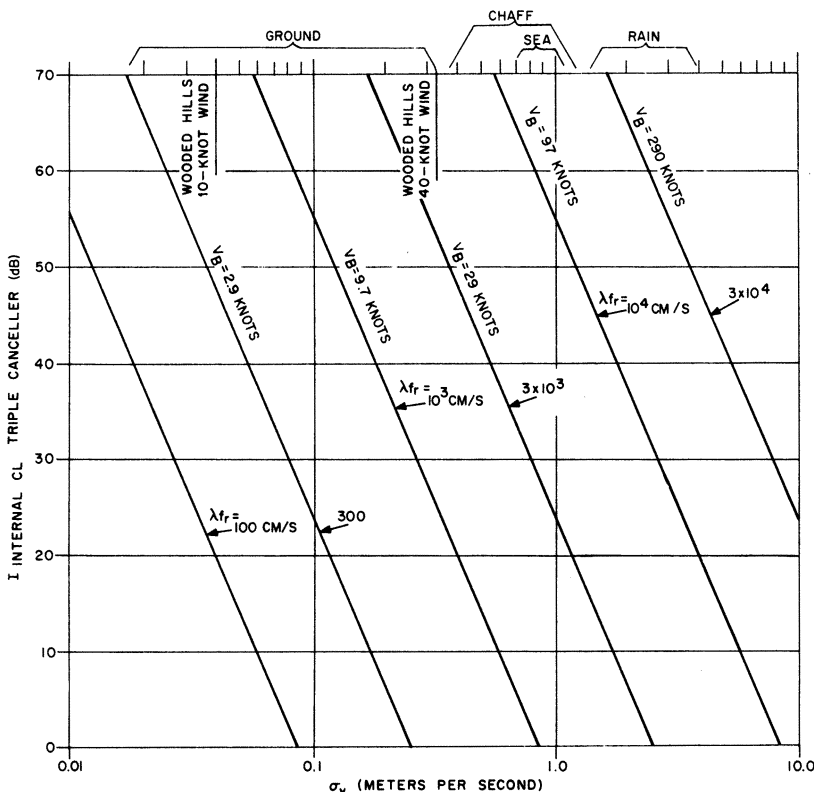


**FIGURE 2.22** MTI improvement factor as a function of the rms velocity spread of clutter for a four-pulse binomial-weight canceler

$S_C(f)$  and the corresponding autocorrelation function is  $R_C(t_i - t_j)$ , then the elements of  $\Phi_C$  are given by

$$\Phi_{ij} = R_C(t_i - t_j) \quad (2.29)$$

where  $t_i$  is the transmission time of the  $i$ th pulse. For example, for a gaussian-shaped clutter spectrum we have

$$S_C(f) = P_C \cdot \frac{1}{\sqrt{2\pi} \cdot \sigma_f} \cdot \exp\left[-\frac{(f - f_d)^2}{2 \cdot \sigma_f^2}\right] \quad (2.30)$$

where  $P_C$  is the total clutter power,  $\sigma_f$  is the standard deviation of the clutter spectral width, and  $f_d$  is the average doppler shift of the clutter. The corresponding autocorrelation function is

$$R_C(\tau) = P_C \exp(-4\pi\sigma_f^2\tau^2) \exp(-j2\pi f_d\tau) \quad (2.31)$$

where  $\tau$  is the separation in time of two consecutive clutter returns.

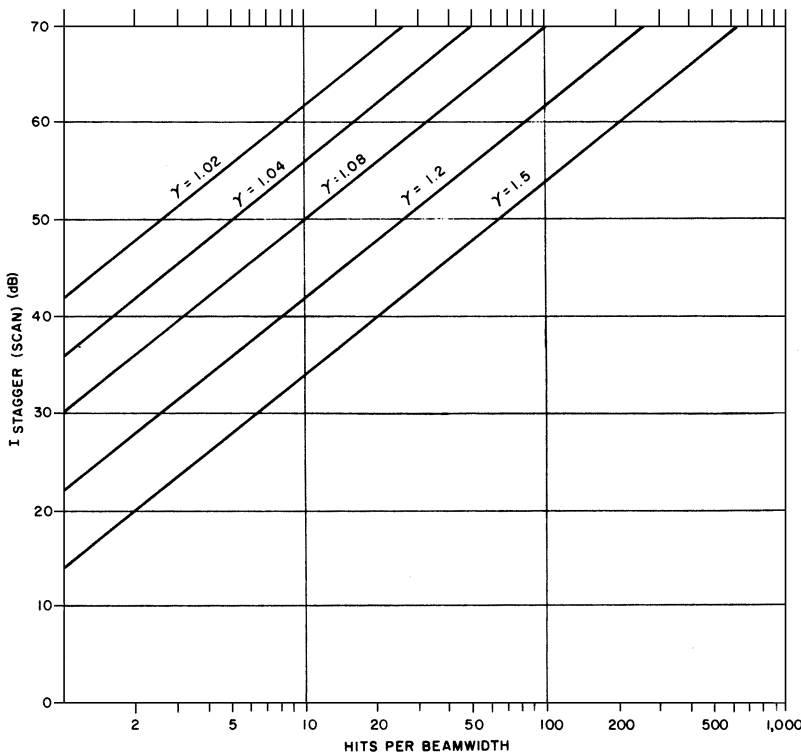


**FIGURE 2.23** Approximate MTI improvement factor limitation due to pulse-to-pulse repetition-period staggering and scanning (all canceler configurations):  $I(\text{dB}) = 20 \log [2.5n/(\gamma - 1)]$ ;  $\gamma$  = maximum period/minimum period

For two pulses separated in time by the interpulse period  $T$ , the complex correlation coefficient between two clutter returns is

$$\rho_T = \exp \left( -4\pi\sigma_f^2 T^2 \right) \cdot \exp (-j2\pi f_d T) \quad (2.32)$$

The second factor in this expression represents the phase shift caused by the doppler shift of the clutter returns.

For a known target doppler shift, the received target return can be represented by an  $N$ -dimensional vector:

$$\mathbf{s} = A_s \cdot \mathbf{f} \quad (2.33)$$

where  $A_s$  is the signal amplitude and the elements of the vector  $\mathbf{f}$  are  $f_i = \exp [j2\pi f_s t_i]$ . On the basis of this description of signal and clutter, it has been shown<sup>18</sup> that the optimum doppler filter will have weights given by

$$\mathbf{w}_{\text{OPT}} = \Phi_C^{-1} \cdot \mathbf{s} \quad (2.34)$$

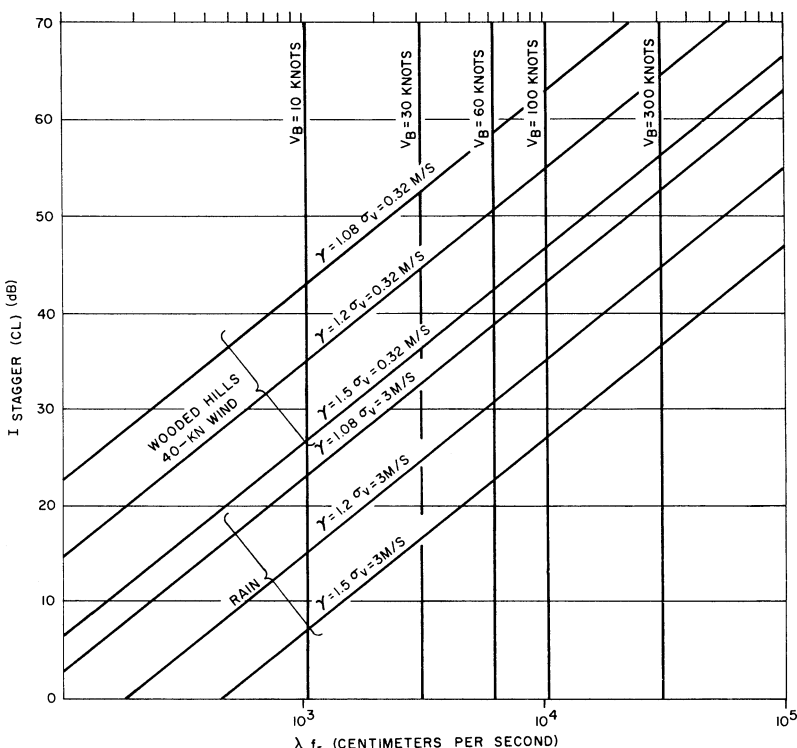


**FIGURE 2.24** Approximate MTI improvement factor limitation due to pulse-to-pulse staggering and internal-clutter motion (all canceler configurations):  $I(dB) = 20 \log [0.33/(\lambda - 1) (\gamma f_r/\sigma_v)]$ ;  $\gamma = \text{maximum period}/\text{minimum period}$

and the corresponding signal-to-clutter improvement is

$$I_{SCR} = \frac{\mathbf{w}_{opt}^T \mathbf{s} \cdot \mathbf{s}^T \mathbf{w}_{opt}^*}{\mathbf{w}_{opt}^T \Phi_C \mathbf{w}_{opt}^*} \quad (2.35)$$

where the asterisk denotes complex conjugation and superscript  $T$  is the transposition operator. An example where the optimum performance is determined for the case of clutter at zero doppler having a gaussian-shaped spectrum with a normalized width of  $\sigma_f T = 0.1$  is shown in Figure 2.25. In this case, a coherent processing interval of CPI = nine pulses was assumed, and the limitation due to thermal noise was ignored by setting the clutter level at 100 dB above noise.

It should be kept in mind that Eq. 2.34 for the optimum weights will yield a different result for each different target doppler shift, so that a large number of parallel filters would be needed to approximate the optimum performance even when the clutter characteristics are known exactly. As an example, the response of the optimum filter designed for one particular target doppler frequency labeled as point A in Figure 2.25 is shown in a broken line. At approximately  $\pm 5\%$  from the design doppler, the performance starts to fall significantly below the optimum.

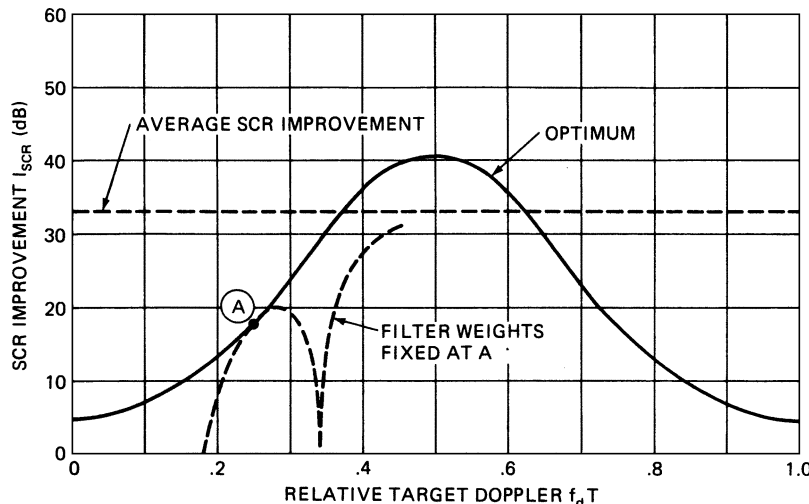


**FIGURE 2.25** Optimum signal-to-clutter ratio improvement  $I_{SCR}$ ) for gaussian-shaped clutter spectrum and a CPI of nine pulses; clutter-to-noise ratio, 100 dB

Also shown in Figure 2.25 is a horizontal line labeled “average SCR improvement.” This indicates the level corresponding to the average of the optimum SCR curve across one doppler interval and may be considered as a figure of merit for a multiple-filter doppler processor, somewhat analogous to the MTI improvement factor defined for a single doppler filter. In Figure 2.26, the optimum average  $I_{SCR}$  has been computed for several different values of the CPI as a function of the normalized spectrum width. These results may be used as a point of reference for practical doppler

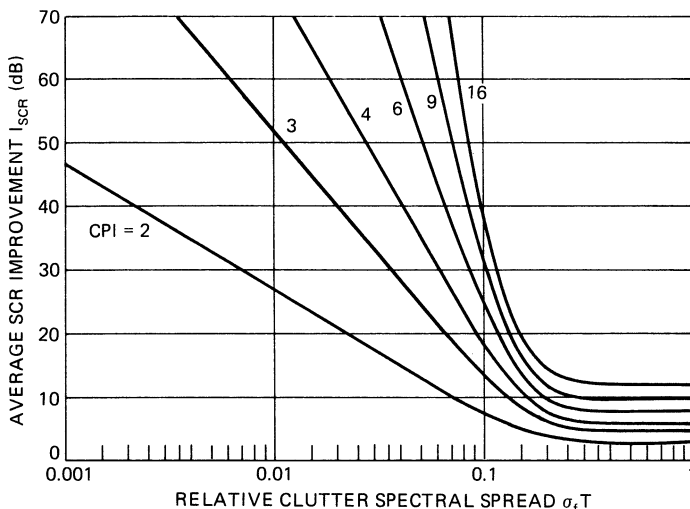


**FIGURE 2.26** Reference curve of optimum average SCR improvement for a gaussian-shaped clutter spectrum

processor designs as discussed in Section 2.9. Note that for  $\sigma_f T \approx 1$  the average SCR improvement is due only to the coherent integration of all the pulses in the CPI.

An MTI filter can also be designed based on the criterion of maximizing the signal-to-clutter improvement at a specific target doppler. However, such a design will usually provide suboptimum performance at all other target dopplers. The single exception is the two-pulse MTI canceler,<sup>19</sup> which provides optimum performance for all target dopplers.

A more attractive approach for designing an optimum MTI filter is to maximize its improvement factor (or clutter attenuation). To design an optimum MTI filter using improvement factor as the criterion, the covariance matrix of the clutter returns, as given by Eq. 2.29, is again the starting point. As shown by Capon,<sup>20</sup> the weights of the optimum MTI filter are found as the eigenvector corresponding to the smallest eigenvalue of the clutter covariance matrix and the MTI improvement factor is equal to the inverse of the smallest eigenvalue. The optimum improvement factor for the three models for the spectrum of land clutter introduced in Section 2.4 have been computed based on this above approach.

For the gaussian clutter spectrum, the optimum improvement factor is shown in Figure 2.27 as a function of the rms relative spectrum width, assuming zero mean for the spectrum. Calculations are shown for MTI cancelers of order  $N = 2$  through 32.

For the polynomial clutter spectrum, the optimum improvement factor is shown in Figure 2.28, again as a function of the RMS relative spectrum width assuming zero mean for the spectrum.

Finally, for the exponential clutter spectrum model, the optimum improvement factor is shown in Figure 2.29, again as a function of the RMS relative spectrum width, assuming zero mean for the spectrum.

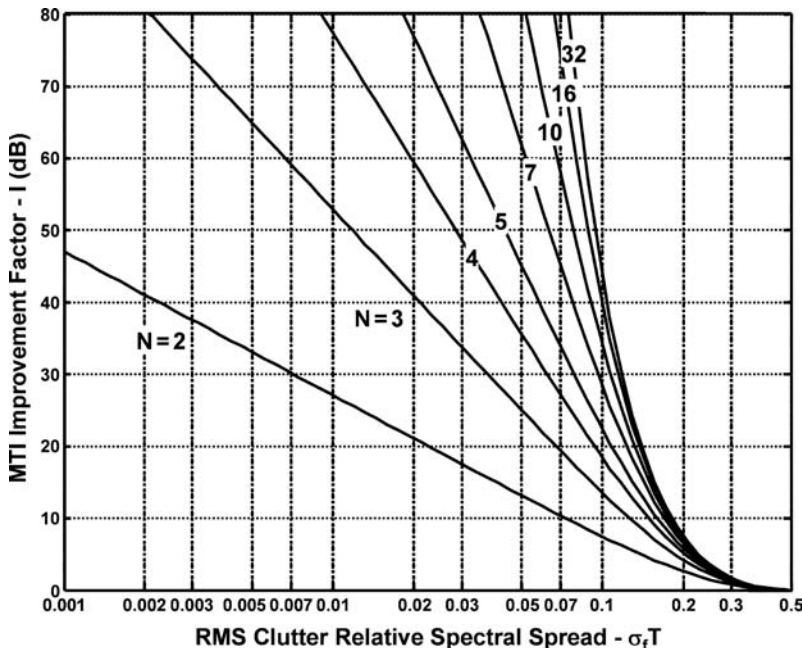
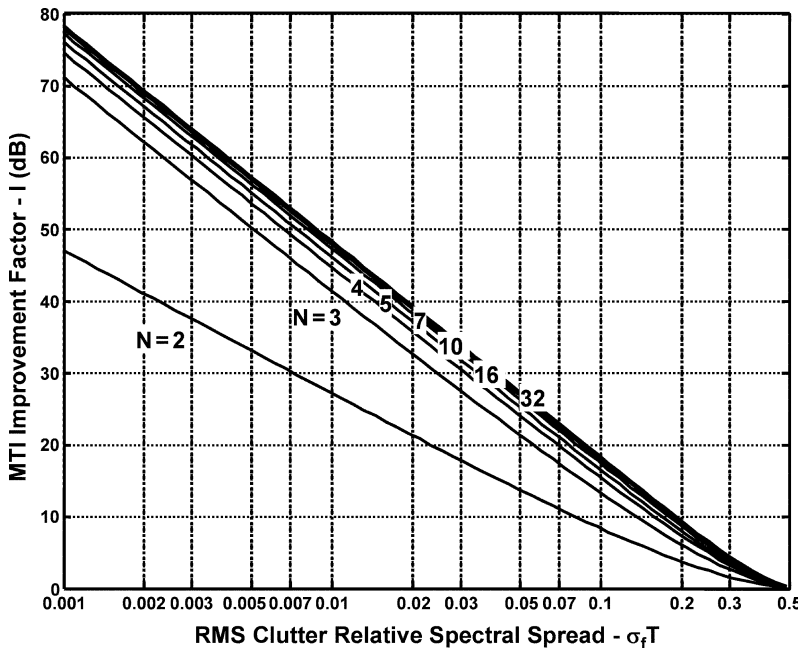
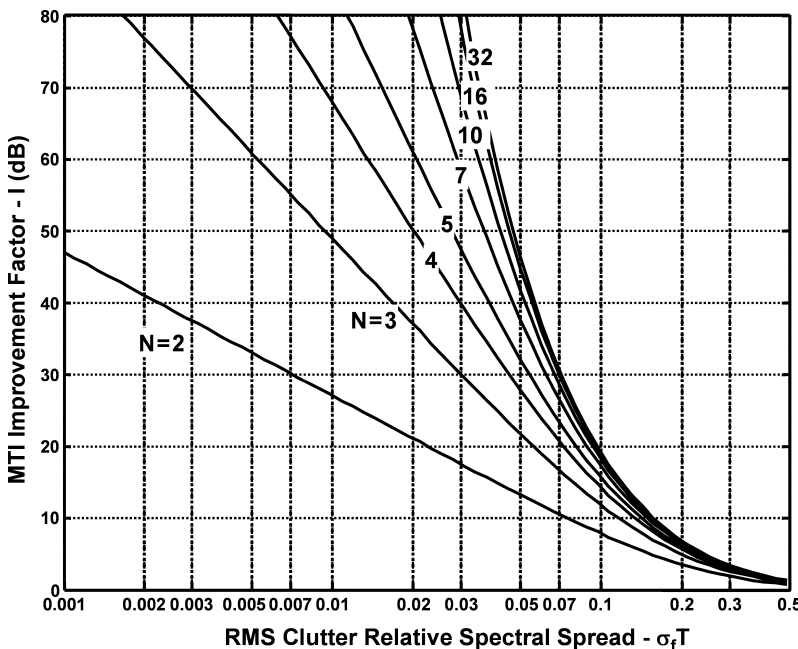


FIGURE 2.27 Optimum improvement factor for gaussian spectrum model



**FIGURE 2.28** Optimum improvement factor for polynomial clutter spectrum model



**FIGURE 2.29** Optimum improvement factor for Billingsley's exponential spectrum model

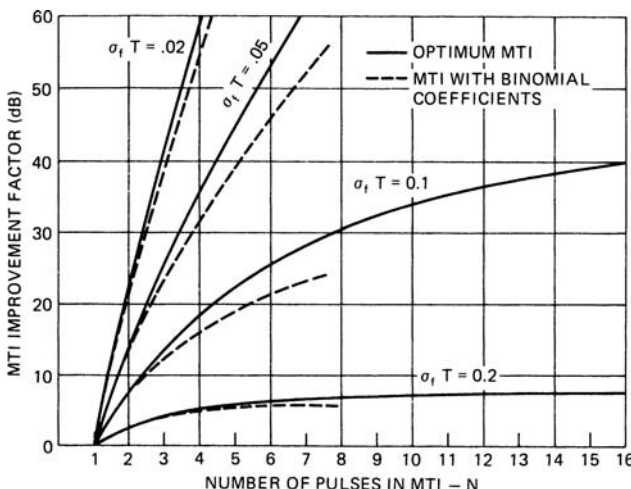


**FIGURE 2.30** Comparison of MTI improvement factor of binomial-weight MTI and optimum MTI against a gaussian-shaped clutter spectrum

In Figure 2.30, the improvement factor of an MTI using the optimum weights is compared with the binomial coefficient MTI for different values of the relative clutter spectral spread and shown as a function of the number of pulses in the CPI. These results again assume a gaussian-shaped clutter spectrum. For typical numbers of pulses in the MTI (three to five), the binomial coefficients are remarkably robust and provide a performance which is within a few decibels of the optimum. Again, it should be noted that any attempt to implement an MTI canceler, which performs close to the optimum, would require the use of adaptive techniques that estimate the clutter characteristics in real time. If the estimate is in error, the actual performance may fall below that of the binomial-weight MTI canceler.

## 2.8 MTI CLUTTER FILTER DESIGN

---

The MTI block diagrams introduced by Figures 2.2 and 2.3 and whose response was discussed in detail in Section 2.3, considered a single-delay\* canceler. It is possible to utilize more than one delay and to introduce feedback and/or feedforward paths around the delays to change the MTI system response to targets of different velocities. Filters with only feedforward paths are called finite impulse response (FIR) filters, and filters that incorporate feedback are called infinite impulse response (IIR) filters, or recursive filters. Multiple-delay cancelers have wider clutter rejection notches than single-delay cancelers. The wider rejection notch encompasses more of the clutter spectrum and thus increases the MTI improvement factor attainable with a given clutter spectral distribution.

\* Delay is used here to represent an interpulse memory for an MTI filter. An FIR filter with one delay is a two-pulse filter. For feedback (IIR) filters, it is inappropriate to call them two-pulse (or three-pulse, etc.) filters because they require a number of pulses to reach steady-state.

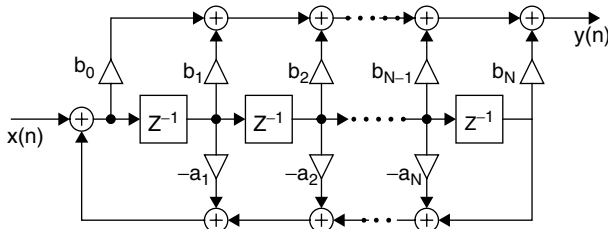
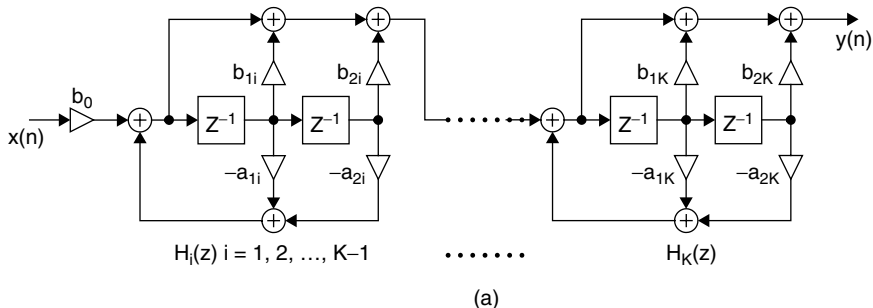


**FIGURE 2.31** Direct Form 2 or canonical form of any MTI filter design

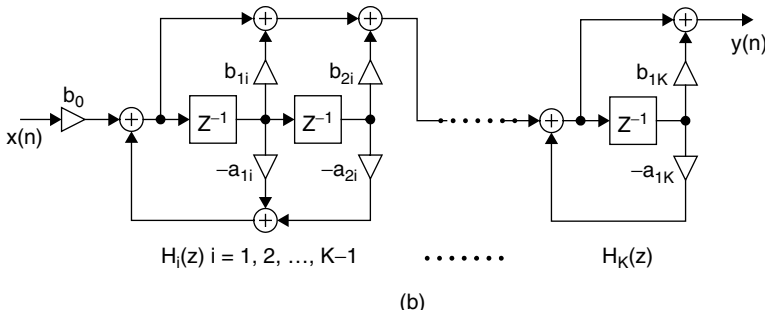
A general block diagram model applicable to any MTI filter is shown in Figure 2.31. This model has been denoted the “Direct Form 2,” or the canonical form, in the terminology survey presented in Rabiner et al.<sup>21</sup>

It can be shown that an MTI filter as shown in Figure 2.31 can be divided into a cascade of second order sections as shown in Figure 2.32.

When a number of single-delay feedforward cancelers are cascaded in series, the overall filter voltage response is  $k2^n \sin^n(\pi f_d T)$ , where  $k$  is the target amplitude,  $n$  is the number of delays,  $f_d$  is the doppler frequency, and  $T$  is the interpulse period.<sup>22</sup> The cascaded single-delay cancelers can be rearranged as a transversal filter, and the weights for each pulse are the binomial coefficients with alternating sign: 1,  $-1$  for two pulses; 1,  $-2$ , 1 for three pulses; 1,  $-3$ , 3,  $-1$  for four pulses, and so on. Changes of the binomial feedforward coefficients and/or the addition of feedback modify the

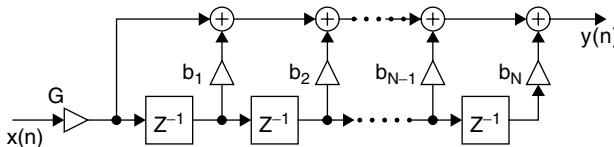


(a)



(b)

**FIGURE 2.32** MTI shown as cascaded form of second order section: (a) is for even order and (b) is for odd order with first order section at end.

FIGURE 2.33 *N*th order FIR MTI canceler block diagram

filter characteristics. Within this chapter, reference to *binomial-weight cancelers* refers to cancelers with the  $2^n \sin^n(\pi f_d T)$  transfer function. The block diagram of this type of MTI canceler is shown in Figure 2.33.

Figure 2.34 to Figure 2.36 represent typical velocity response curves obtainable from one-, two-, and three-delay cancelers. Shown also are the canceler configurations assumed, with corresponding Z-plane pole-zero diagrams. The Z plane is the comb-filter equivalent of the S plane<sup>23</sup> with the left-hand side of the S plane transformed to the inside of the unit circle centered at  $Z = 0$ . Zero frequency is at  $Z = 1 + j0$ . The stability requirement is that the poles of the Z transfer function lie within the unit circle. Zeros may be anywhere.

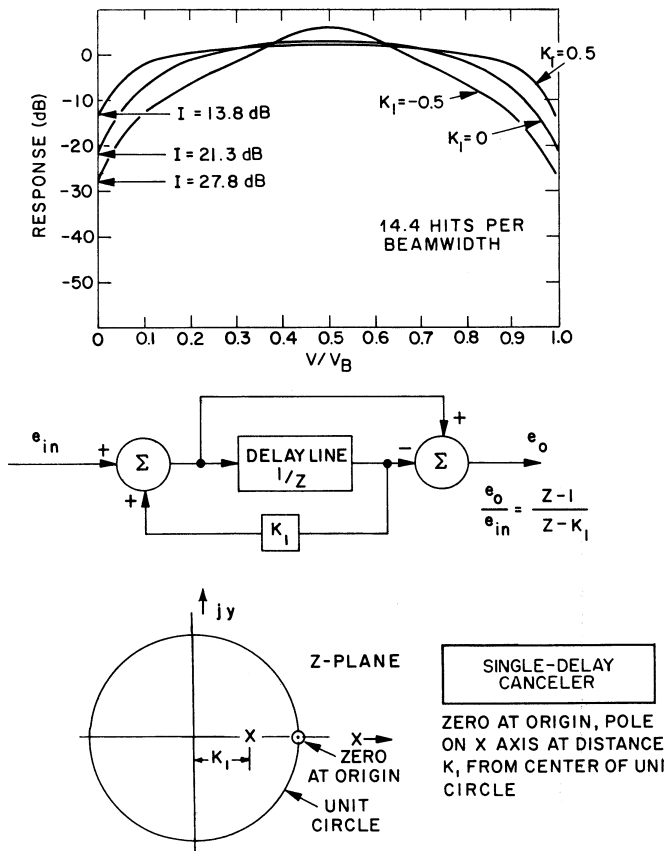
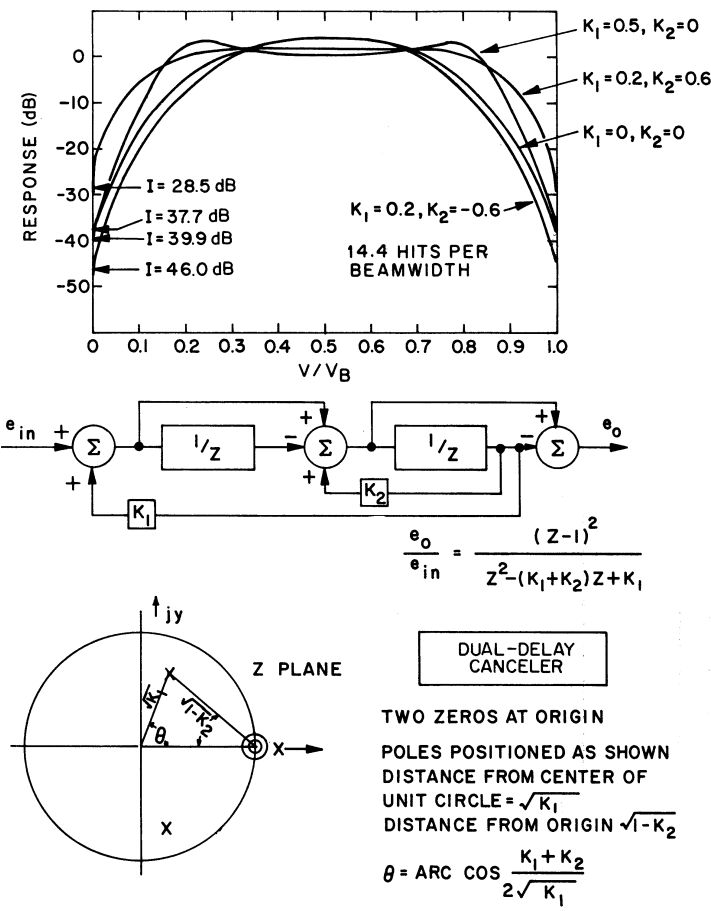


FIGURE 2.34 One-delay canceler



POLES SHOWN FOR  $K_1 = 0.5, K_2 = 0$

FIGURE 2.35 Two-delay canceler

These velocity response curves are calculated for a scanning radar system with 14.4 hits per one-way 3-dB beamwidth. An antenna beam shape of  $(\sin U)/U$ , terminated at the first nulls, was assumed. The shape of these curves, except very near the blind speeds, is essentially independent of the number of hits per beamwidth or the assumed beam shape.

The ordinate labeled “response” represents the single-pulse signal-to-noise output of the MTI receiver relative to the signal-to-noise response of a normal linear receiver for the same target. Thus, all the response curves are normalized with respect to the noise power gain for the given canceler configuration. The intersection at the ordinate represents the negative decibel value of  $I$ , the MTI improvement factor for a point clutter target processed in a linear system.

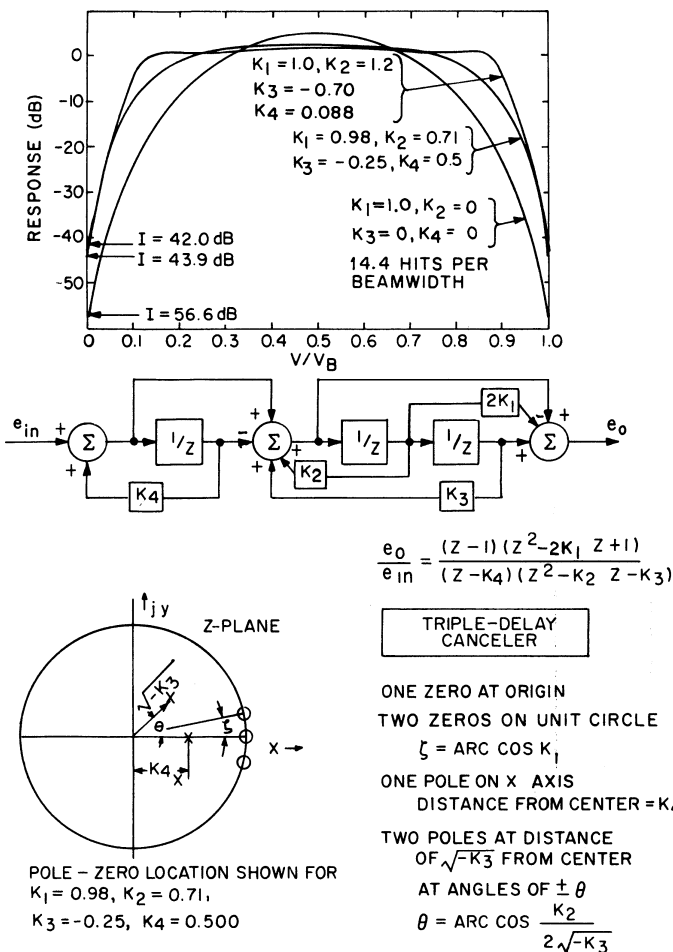


FIGURE 2.36 Three-delay canceler

Because these curves show the signal-to-noise response for each output pulse from the MTI canceler, the inherent loss incurred in a scanning radar with MTI processing due to the reduction of the effective number of independent pulses integrated<sup>24</sup> is not apparent. This loss is 1.4 dB for a 3-pulse canceler and 2.1 dB for a 5-pulse canceler, assuming a large number of pulses. If quadrature MTI channels (see Section 2.13) are not employed, there is an additional loss of 1½ to 3 dB.

The abscissa of these curves,  $V/V_B$ , represents the ratio of target velocity  $V$  to the blind speed  $V_B = \lambda f_r/2$ , where  $\lambda$  is the radar wavelength and  $f_r$  is the average PRF of the radar. The abscissa can also be interpreted as the ratio of the target doppler frequency to the average PRF of the radar.

The canceler configurations shown are not the most general feedforward, feedback networks possible. Pairs of delays are required to locate zeros and poles elsewhere

than on the real axis of the Z-plane. In the configurations shown, the zeros are constrained to the unit circle. To move the zeros off of the unit circle, which may be done to control the flatness of the filter passband response, requires a configuration similar to the elliptic filter configuration shown in Figure 2.46 later in this chapter. The triple-canceler configuration shown is such that two of the zeros can be moved around the unit circle in the Z plane. Moving the zeros can provide a 4 or 5 dB increase in the MTI improvement factor for specific clutter spectral spreads, as compared with keeping all three zeros at the origin.<sup>25</sup>

Note the width of the rejection notches for the different binomial-weight canceler configurations. If the -6 dB response relative to average response is used as the measuring point, the rejection is 24% of all target dopplers for the single canceler, 36% for the dual canceler, and 45% for the triple canceler. Consider the dual canceler: Eliminating 36% of the dopplers means limiting the system to a long-term average of 64% single-scan probability of detection. Feedback can be used to narrow the rejection notch without much degradation of  $I$ . If feedback is used to increase the improvement factor, the single-scan probability of detection becomes worse.

Figure 2.37 shows the improvement factor limitation due to scanning for cancelers with feedback. These curves were calculated assuming a  $(\sin U)/U$  antenna pattern terminated at the first nulls.

The no-feedback curves shown in Figure 2.37 are almost indistinguishable from the theoretical curves derived for a gaussian pattern shown in Figure 2.19. (One of the curves showing the effect of feedback on the triple canceler is not straight because two of the three zeros are not at the origin but have been moved along the unit circle the optimum amount for 14 hits per beamwidth. Thus, at 40 hits per beamwidth, these two zeros are too far removed from the origin to be very effective.)

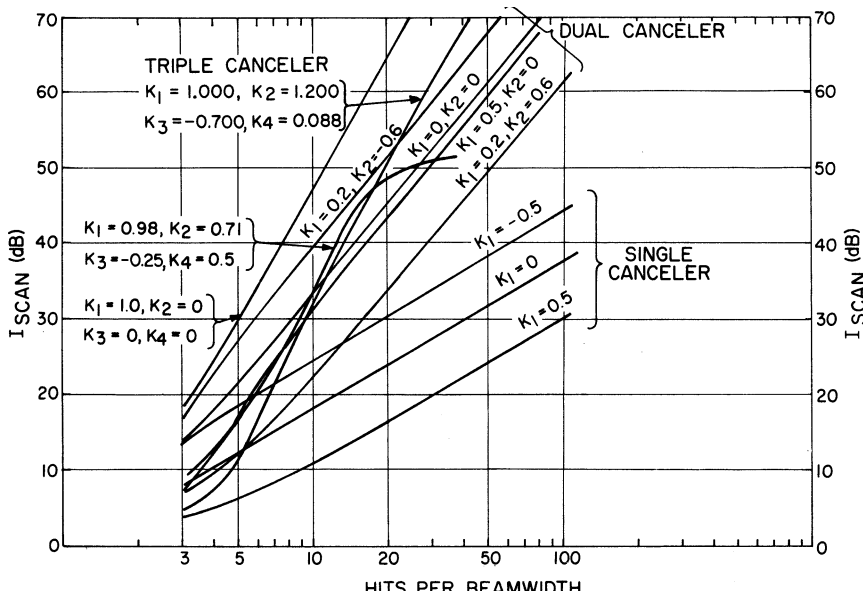


FIGURE 2.37 Improvement factor limitation due to scanning for cancelers with feedback

In theory, it is possible to synthesize almost any velocity response curve with digital filters.<sup>26</sup> As mentioned earlier, for each pair of poles and pair of zeros on the Z plane, two delay sections are required. The zeros are controlled by the feedforward paths and the poles by the feedback paths.

Velocity response shaping can be accomplished by the use of feedforward only without the use of feedback. The principal advantage of not using feedback is the excellent transient response of the canceler, an important consideration in a phased array or when pulse interference noise is present. If a phased array radar should use a feedback canceler, many pulses would have to be gated out after the beam has been repositioned before the canceler transient response has settled to a tolerable level. An initialization technique has been proposed<sup>27</sup> to alleviate this problem, but it provides only partial reduction in the transient settling time. If feedforward only is used, only three or four pulses have to be gated out after moving the beam. The disadvantage of using feedforward for velocity response shaping is that an additional delay, and therefore an additional transmit pulse, must be provided for each zero used to shape the response. Figure 2.38 shows the velocity response and Z-plane diagram of a feedforward-only, shaped-response, four-pulse canceler. Also shown are the velocity responses of a five-pulse feedforward canceler and a three-pulse feedback canceler. For the cancelers shown, the improvement factor capability of the three-pulse canceler is about 4 dB better than the shaped-response four-pulse feedforward canceler, independent of clutter spectral spread.

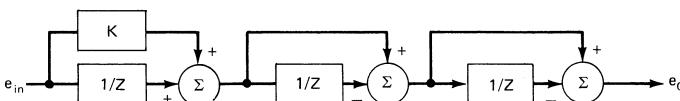
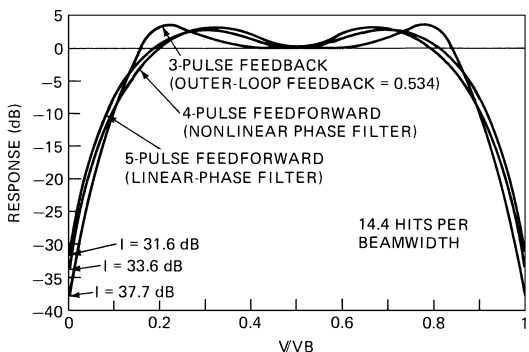
The five-pulse canceler response shown is a linear-phase<sup>28</sup> MTI filter described by Zverev.<sup>29</sup> The four zeros are located on the Z-plane real axis at +1.0, +1.0, -0.3575, and -2.7972. Much of the literature on filter synthesis describes linear-phase filters, but for MTI applications linear phase is of no importance. Almost identical filter responses can be obtained with nonlinear-phase filters that require fewer pulses, as shown in Figure 2.38. Because only a fixed number of pulses is available during the time on target, none should be wasted. Thus, one should choose the nonlinear-phase filter that uses fewer pulses.

**Stagger Design Procedures.** The interval between radar pulses may be changed to modify the target velocities to which the MTI system is blind. The interval may be changed on a pulse-to-pulse, dwell-to-dwell (each dwell being a fraction of the beamwidth), or scan-to-scan basis. Each approach has advantages. The advantages of the scan-to-scan method are that it is easier to build a stable transmitter, and multiple-time-around clutter is canceled in a power amplifier MTI system. The transmitter stabilization necessary for good operation of an unstaggered MTI is a significant challenge. To stabilize the transmitter sufficiently for pulse-to-pulse or dwell-to-dwell stagger operation is considerably more difficult. Typically, pulse-to-pulse staggering is used with MTI processing, whereas dwell-to-dwell staggering is used with MTD (filter bank) processing.

For many MTI applications pulse-to-pulse or dwell-to-dwell staggering is preferable to scan-to-scan staggering.<sup>†</sup> For example, if a binomial-weighted three-pulse canceler that has 36%-wide rejection notches is employed and if scan-to-scan pulse staggering is used, 36% of the desired targets would be missing on each scan owing to doppler consideration alone. This might be intolerable for some applications.

---

<sup>†</sup> The choice between pulse-to-pulse staggering and dwell-to-dwell (MTD) operation is a system concept decision—both approaches have their advantages. For example, pulse-to-pulse staggering will not provide canceling of clutter in the ambiguous range intervals. With dwell-to-dwell staggering, an extra transmitter pulse (also known as a fill pulse) will enable canceling of second range interval clutter.



$$\frac{e_0}{e_{in}} = \frac{(Z-1)^2 (Z + \frac{1}{K})}{Z^3}$$

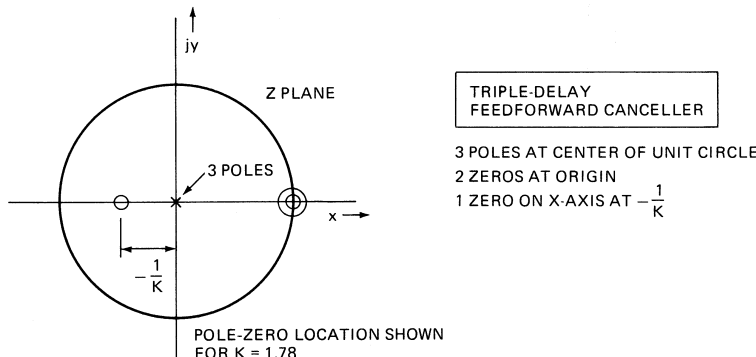


**FIGURE 2.38** Shaped-velocity-response feedforward cancelers compared with three-pulse feedback canceler. See text for five-pulse canceler parameters.

With pulse-to-pulse staggering, good response can be obtained on all dopplers of interest on each scan. In addition, better velocity response can be obtained at some dopplers than either pulse interval will give on a scan-to-scan basis. This is so because pulse-to-pulse staggering produces doppler components in the passband of the MTI filter. Pulse-to-pulse staggering may degrade the improvement factor attainable, as shown in Figure 2.23 and Figure 2.24, but this degradation may not be significant, or it can be eliminated by the use of time-varying weights as described below. One further advantage of pulse-to-pulse staggering is that it may permit eliminating the use of feedback in the cancelers (used to narrow the blind-speed notches), which eliminates the transient settling problem of the feedback filters.

The optimum choice of the stagger ratio depends on the velocity range over which there must be no blind speeds and on the permissible depth of the first null

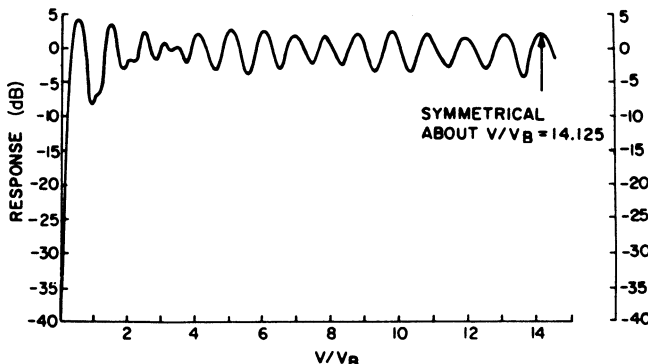


**FIGURE 2.39** Velocity response curve: dual canceler, no feedback, 25:30:27:31 pulse-interval ratio

in the velocity response curve. For many applications, a four-period stagger ratio is best, and a good set of stagger ratios can be obtained by adding the first blind speed (in  $V/V_B$ ) to the numbers  $-3, 2, -1, 3$  (or  $3, -2, 1, -3$ ). Thus, in Figure 2.41<sup>‡</sup>, where the first blind speed occurs at about  $V/V_B = 14$ , the stagger ratio is  $11:16:13:17$ <sup>§</sup> (alternating the long and short periods keeps the transmitter duty cycle as nearly constant as possible, as well as ensuring good response at the first null where  $V = V_B$ ). Figures 2.39 and 2.42 show two other 4-period velocity response curves. If using four interpulse periods makes the first null to be too deep, then five interpulse periods may be used, with the stagger ratio obtained by adding the first blind speed to the number  $-6, +5, -4, +4, +1$ . Figure 2.40 shows a velocity response curve for five pulse intervals. The depth of the first null can be predicted from Figure 2.45, which is discussed later.

For a radar system with relatively few hits per beamwidth, it is not advantageous to use more than four or five different intervals because then the response to an individual target will depend on which part of the pulse sequence occurs as the peak of the beam passes the target. Random variation of the pulse intervals is not desirable (unless used as an electronic counter-countermeasure feature) because it permits the nulls to be deeper than the optimum choice of four- or five-pulse intervals.

When the ratio of pulse intervals is expressed as a set of relatively prime integers (i.e., a set of integers with no common divisor other than 1), the first true blind speed occurs at

$$\frac{V}{V_B} = \frac{R_1 + R_2 + R_3 + \dots + R_N}{N} \quad (2.36)$$

<sup>‡</sup> All velocity response curves plotted herein present the average power response of the output pulses of the canceler for the duration of the time on target for a scanning radar. If staggering were used with batch processing, such as in a phased array, these curves would not apply for a single output. For example, if the stagger ratio was  $11:16:13:17$  and a three-pulse FIR filter is used, it would be necessary to transmit six pulses, with interpulse spacings of  $11:16:13:17:11$  and sum the power output from the filter after the last four pulses were transmitted to get the equivalent response shown in these curves.

<sup>§</sup> Note that the first differences between all combinations of the integers  $11, 16, 13$ , and  $17$  are  $1, 2, 3, 4, 5, 6$ . This “perfect difference set” for the stagger sequence is the key to the relative flatness of the response curves.

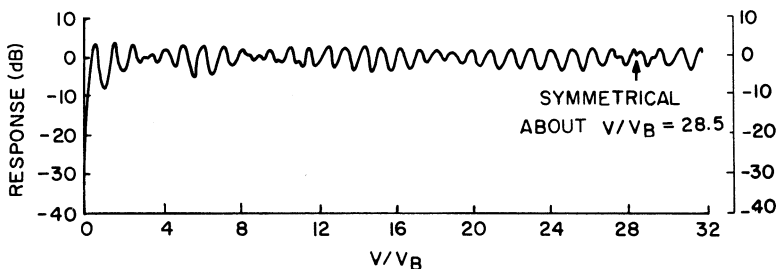


**FIGURE 2.40** Velocity response curve: three-pulse binomial canceler, 51:62:53:61:58 pulse-interval ratio

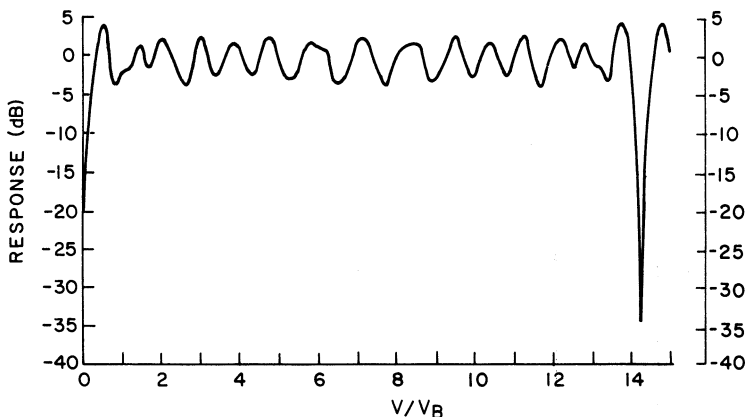


**FIGURE 2.41** Velocity response curve: three-pulse binomial canceler, 11:16:13:17 pulse-interval ratio

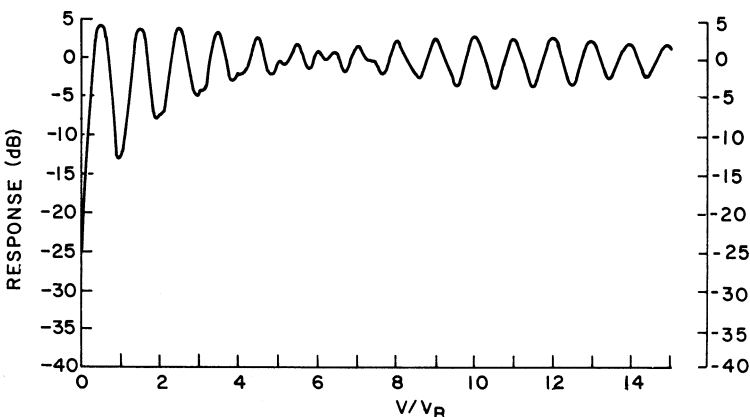


**FIGURE 2.42** Velocity response curve: three-pulse binomial canceler, 53:58:55:59 pulse-interval ratio. This response curve continues to  $V/V_B = 53$  with no dips below 5 dB. The first blind speed is at  $V/V_B = 56.25$ .

where  $(R_1, R_2, R_3, \dots, R_N)$  are the set of integers and  $V_B$  is the blind speed corresponding to the average interpulse period. The velocity response curve is symmetrical about one-half of the value from Eq. 2.36.

**Feedback and Pulse-to-Pulse Staggering.** When pulse-to-pulse staggering is employed, the effect of feedback is reduced. Staggering causes a modulation of the signal doppler at or near the maximum response frequency of the canceler. The amount of this modulation is proportional to the absolute target doppler so that, for an aircraft flying at  $V_B$ , the canceler response is essentially independent of the feedback employed. Figure 2.43 shows a plot of the effects of feedback on a dual-canceler system with 14.4 hits per beamwidth and a ratio of stagger intervals of 6:7:8. The feedback values employed are several of those used for the unstaggered velocity response plot in Figure 2.35. If scan-to-scan pulse-interval staggering had been used instead of pulse-to-pulse, the no-feedback rms response for three scans at a target velocity of  $V_B$  would be  $-12.5$  dB. The composite response for pulse-to-pulse staggering, however, is only  $-6$  dB at  $V_B$ , thus illustrating the advantage of pulse-to-pulse staggering.

**Improvement Factor Limitations Caused by Staggering.** When pulse-to-pulse staggering is used, it limits the attainable improvement factor owing to the unequal time spacing of the received clutter samples. The curves in Figure 2.23 and Figure 2.24, which have been referred to several times, give the approximate limitation on  $I$  caused by pulse-to-pulse staggering and either antenna scanning or internal clutter motion. They have been derived as explained below.

A two-delay canceler will perfectly cancel a linear waveform,  $V(t) = c + at$ , if it is sampled at equal time intervals independent of the constant  $c$  or the slope  $a$ . (Additional delay cancelers perfectly cancel additional waveform derivatives; e.g., a three-delay canceler will perfectly cancel  $V(t) = c + at + bt^2$ .) A stagger system with two pulse intervals samples the linear waveform at unequal intervals, and therefore

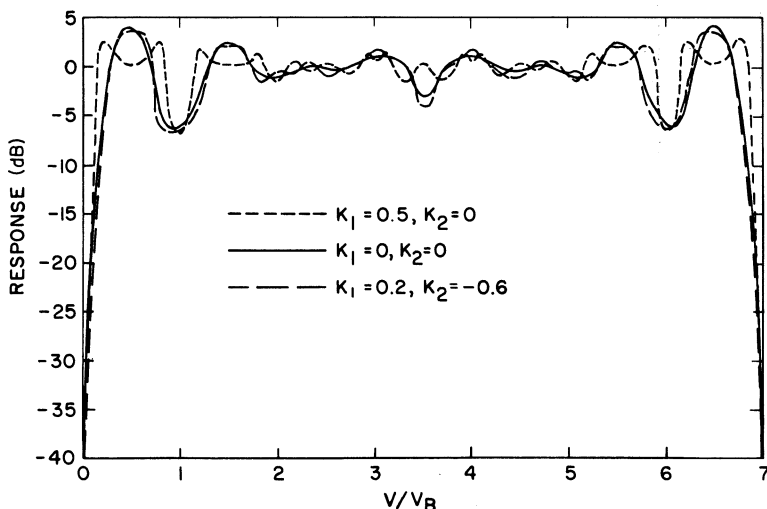


**FIGURE 2.43** Effect of feedback on the velocity response curve: dual canceler, 6:7:8 pulse-interval ratio

there will be a voltage residue from the cancelers that is proportional to the slope  $a$  and inversely proportional to  $\gamma - 1$ , where  $\gamma$  is the ratio of the intervals. The apparent doppler frequency of the residue will be at one-half the average repetition rate of the system and thus will be at the frequency of maximum response of a binomial-weight canceler.

The rate of change of phase or amplitude of clutter signals in a scanning radar is inversely proportional to the hits per beamwidth,  $n$ . Thus, with the use of a computer simulation to determine the proportionality constant, the limitation on  $I$  due to staggering is approximately

$$I \approx 20 \log \left( \frac{2.5n}{\gamma-1} \right) \text{dB} \quad (2.37)$$

which is plotted in Figure 2.23.

These curves, which apply to all multiple-delay cancelers, give answers that are fairly close to the actual limitation that will be experienced for most practical stagger ratios. An example of the accuracy is as follows: A system with 14.4 hits per beamwidth, a four-pulse binomial weight canceler, and a 6:9:7:8 pulse-interval ratio has an improvement factor limitation of 36.5 dB due to staggering. The curve gives a limitation of 37.2 dB for this case. But if the sequence of pulse intervals were to be changed from 6:9:7:8 to 6:8:9:7, the actual limitation would be 41.1 dB, which is 3.9 dB less than that indicated by the curve. This occurs because the primary modulation with a 6:9:7:8 pulse-interval ratio looks like a target at maximum-response speed, whereas the primary modulation with a 6:8:9:7 pulse-interval ratio looks like a target at one-half the speed of maximum response. Because it is desirable to average the transmitter duty cycle over as short a period as possible, the 6:9:7:8 pulse-interval ratio would probably be chosen for a practical system.

Once Eq. 2.37 for the limitation on  $I$  due to scanning and staggering is obtained, it is possible to determine the limitation on  $I$  due to internal-clutter motion and staggering. If

$$n = \frac{\sqrt{\ln(2)}}{2\pi} \times \frac{\lambda f_r}{\sigma_v} = 0.1325 \frac{\lambda f_r}{\sigma_v} \quad (2.38)$$

(from Eqs. 2.14 and 2.15) is substituted into Eq. 2.37,

$$I = 20 \log \left( \frac{2.5}{\gamma-1} \times \frac{0.1325 \lambda f_r}{\sigma_v} \right) = 20 \log \left( \frac{0.33 \lambda f_r}{(\gamma-1) \sigma_v} \right) \quad (2.39)$$

where  $\lambda$  is the wavelength,  $f_r$  is the average pulse repetition frequency, and  $\sigma_v$  is the rms velocity spread of scattering elements. This is plotted in Figure 2.24 for rain and for wooded hills with a 40 knot wind. This limitation on the MTI improvement factor is independent of the type of canceler employed.

**Time-Varying Weights.** The improvement factor limitation caused by pulse-to-pulse staggering can be avoided by the use of time-varying weights in the canceler forward paths instead of binomial weights. The use of time-varying weights has no appreciable effect on the MTI velocity response curve. Whether the added complexity of utilizing time-varying weights is desirable depends on whether the stagger

limitation is predominant. For two-delay cancelers, the stagger limitation is often comparable with the basic canceler capability without staggering. For three-delay cancelers, the stagger limitation usually predominates.

Consider the transmitter pulse train and the canceler configurations shown in Figure 2.44. During the interval  $T_N$  when the returns from transmitted pulse  $P_N$  are being received, the two-delay canceler weights should be

$$A = 1$$

$$C = \frac{T_{N-2}}{T_{N-1}} \quad (2.40)$$

$$B = -1 - C$$

and the three-delay canceler weights should be

$$A = 1$$

$$C = 1 + \frac{T_{N-3} + T_{N-1}}{T_{N-2}} \quad (2.41)$$

$$B = -C$$

$$D = -1$$

These weights have been derived by assuming that the cancelers should perfectly cancel a linear waveform  $V(t) = c + at$ , sampled at the stagger rate, independent of the values of the constant  $c$  or the slope  $a$ . (As mentioned at the beginning of this section, a multiple-delay canceler with binomial weights in an unstaggered system will perfectly cancel  $V(t) = c + at$ .)

The choice of  $A = 1$  in both cases is arbitrary. In the three-delay canceler, setting  $D = -1$  eliminates the opportunity for a second-order correction to cancel the quadratic term  $bt^2$ , which could be obtained if  $D$  were also time-varying. Computer calculations have shown that it is unnecessary to vary  $D$  in most practical systems.

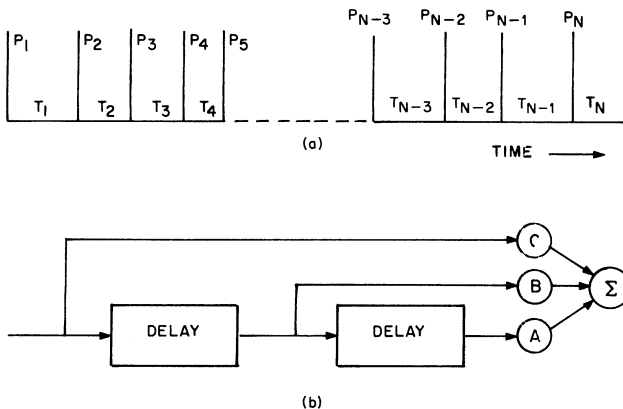


**FIGURE 2.44** Use of time-varying weights: (a) pulse train, (b) two-delay canceler, and (c) three-delay canceler

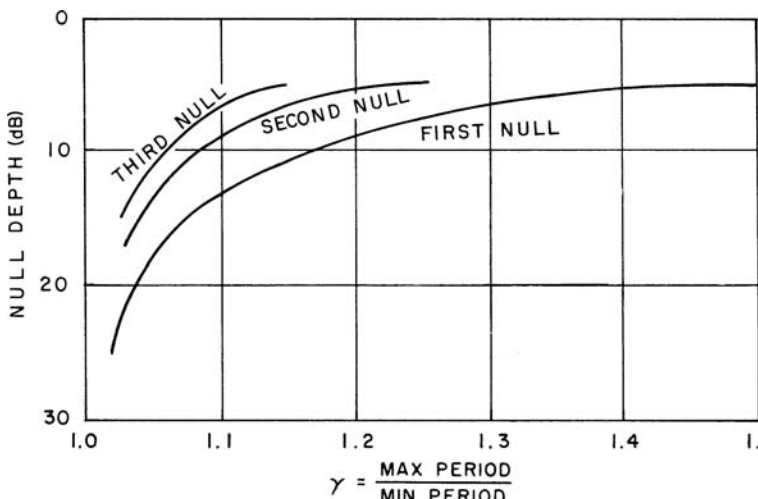


**FIGURE 2.45** Approximate depth of nulls in the velocity response curve for pulse-to-pulse staggered MTI

**Depth of First Null in Velocity Response.** When selecting system parameters, it is useful to know the depth of the first few nulls to be expected in the velocity response curve. As discussed earlier, the null depths are essentially unaffected by feedback. They are also essentially independent of the type of canceler employed, whether single, dual, or triple, or of the number of hits per beamwidth. Figure 2.45 shows approximately what null depths can be expected versus the ratio of maximum to minimum interpulse period.

## 2.9 MTI FILTER DESIGN FOR WEATHER RADARS

---

MTI filters are used at the lower elevation angles in weather radars to prevent weather estimates from being contaminated with ground clutter returns. It is, however, also very important to preserve an accurate measurement of weather intensity and precipitation rate. To meet this dual objective, MTI filters with narrow fixed clutter rejection notches and flat passbands are needed. Use of a very narrow clutter notch even permits measuring weather precipitation rates with a mean radial velocity of zero, albeit with some bias.\* Such measurement is possible because weather usually has a wide spectral spread—typically 1 to 4 m/s—whereas fixed clutter has a much narrower spectral spread—typically less than 0.5 m/s.

\* Bias as used herein refers to the error in measuring radar reflectivity due to the clutter notch and lack of flatness of the MTI filters. When weather has a wide spectral spread and the clutter notch of the filters is narrow, there is minimal measurement error induced by the MTI filters. Conversely, when the weather spectral width is narrow and the radial velocity of the weather is near zero, significant error in the weather reflectivity measurement will exist. There are other causes of error between radar estimates of precipitation rates and rain gauge measurements that are not addressed herein, such as the spatial and temporal distribution of rain.

Examples of weather radar applications for which MTI filters are used:

- Weather Doppler Radars (NEXRAD/WSR-88)* Radars with rotating antennas that measure precipitation rate, doppler velocity, and turbulence. Measures total rainfall and provides tornado warnings.
- Terminal Doppler Weather Radars (TDWR)* Radars with rotating antennas designed to detect severe wind shear in aircraft approach and departure paths close to airports.
- Airport Surveillance Radars* Radars with rotating antennas designed for air traffic control functions in the terminal area but with a secondary function of detecting and monitoring severe weather and wind shear in aircraft approach and departure paths.
- Phased Array Radars* Radars with fixed electronically scanned antennas designed for many functions such as missile detection and air traffic control, and used concurrently for measuring precipitation rates.

As an example, the design of elliptic MTI filters as used in the TDWR will be described. TDWR is a C-band radar used at airports for detection of downbursts, microbursts, and prediction of wind direction. Elliptic filters are infinite impulse response (IIR) filters that have the sharpest possible transition from rejection notch to passband for a specified level of the clutter rejection notch (width and depth), ripple in the passband, and number of delay sections (see Oppenheim and Schafer<sup>28</sup>). The elliptic filters can be followed with pulse-pair processing<sup>13</sup> for estimation of weather mean velocity and spectral width (turbulence). There are two drawbacks of elliptic filters: First, the long transient settling time. For a scanning weather radar, it takes about four beamwidths of scanning after the transmitter starts pulsing before clutter attenuation reaches 50 to 60 dB. Second, if the input clutter signal reaches the limit level in the IF receiver, there will be a significant transient increase of clutter residue. One of the elliptic filters employed in the original TDWR radar is used as an example.

TDWR operates at C band (5.60-5.65 GHz). The antenna rotates at 4.33 rpm and has a 0.55° one-way beamwidth. The PRF is 1066 Hz. The elliptic filter designed for these parameters has an improvement factor of 57.2 dB. HBW (hits per one-way 3-dB beamwidth) are 22.6. The specifications for the elliptic filter for the above parameters are normalized stopband edge  $\sigma_f T = 0.03492$ ; passband edge  $\sigma_f T = 0.07350$ ; stopband attenuation 58 dB below peak filter response; and passband ripple = 2.0 dB. To meet these requirements, the filter requires 4-delay sections, which can be implemented as two cascaded 2-delay sections, as shown in Figure 2.46.

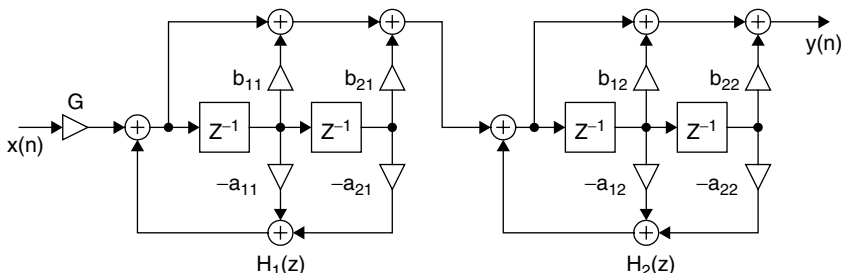


FIGURE 2.46 Four-delay elliptic filter used in TDWR

The filter coefficients are

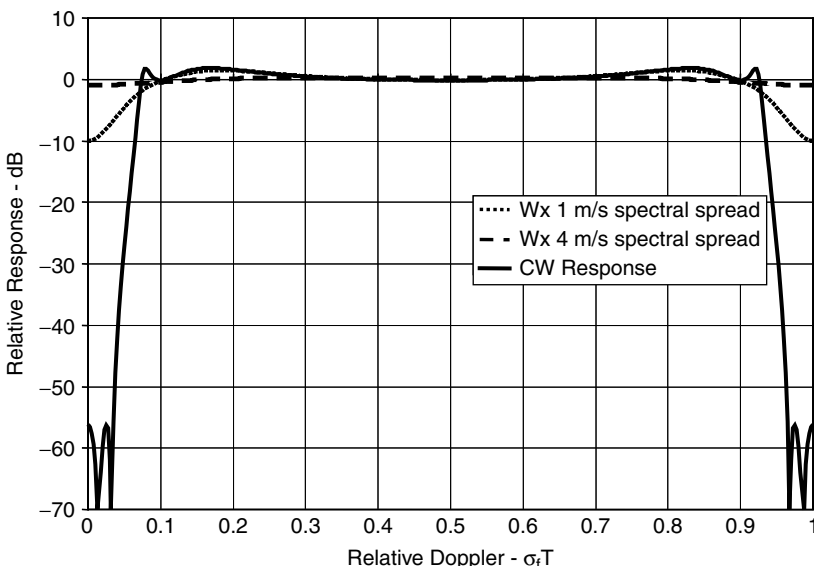
$$\begin{array}{ll} a_{11} = -0.901933 & a_{12} = -1.701983 \\ a_{21} = 0.420985 & a_{22} = 0.914913 \\ b_{11} = 1.000000 & b_{21} = 1.000000 \\ b_{21} = -1.992132 & b_{22} = -1.958290 \end{array}$$

The calculated improvement factor for this filter against land clutter with 22.6 HBW is 58 dB, and the bias for weather returns with spectral spreads of 1 and 4 m/sec is  $-10$  dB and  $-2$  dB, respectively, when the radial velocity of the weather returns is  $v = 0$  m/s.

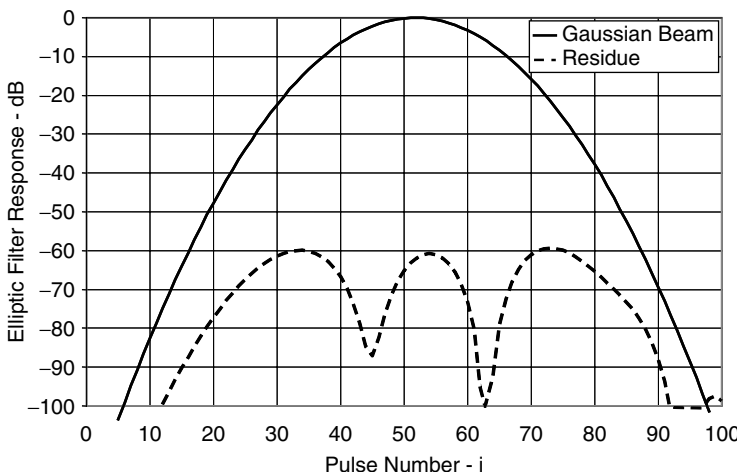
Figure 2.47 shows the elliptic filter CW response and its response for weather with 1 m/s and 4 m/s rms spectral spread. The unambiguous doppler interval corresponding to  $f_d T = 1$  is 28.4 m/s for the parameters used to calculate this response.

Figure 2.48 shows the time-domain responses for this filter as the antenna scans past a point of clutter, such as a water tower. This figure shows the input to the elliptic filter and the residue output. A gaussian antenna pattern is assumed in this figure. The calculated improvement factor for the sequence shown (total clutter power into the filter divided by total residue power out of the filter, normalized by the noise gain of the filter) is 58 dB.

A  $\sin(x)/x$  antenna pattern is assumed for the following three figures, but the lessons to be gained from these figures is essentially independent of the assumed beam shape. Figure 2.49 shows the filter response if the transmitter starts radiating just as a null of the antenna pattern passes the point of clutter. The individual samples of residue are 60 or more dB below the peak clutter return. The improvement factor for this sequence is 57 dB.



**FIGURE 2.47** Elliptic filter CW response and response to weather with  $\sigma = 1$  and 4 m/s rms spectral spread



**FIGURE 2.48** Time-domain clutter input and output residue as antenna scans past a point target

Figure 2.50 shows the residue if the transmitter starts radiating as the peak of the beam passes the point clutter. Forty-nine pulses after the transmitter starts radiating, the residue has decayed only 27 dB. It would take at least another 50 pulses for the residue to decay to -60 dB. For this reason, when the transmitter starts pulsing, a settling time of at least 90 pulses must be allowed before useful data is collected.

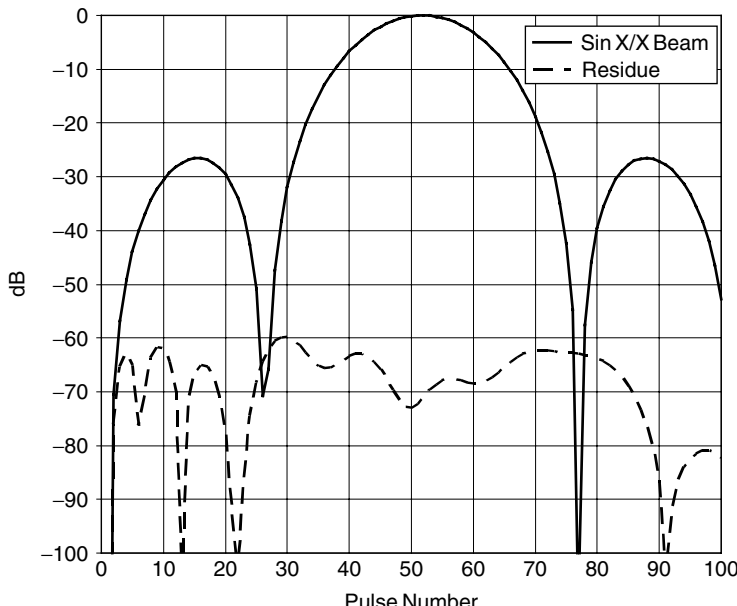


**FIGURE 2.49** Clutter input and residue from elliptic filter. Radar starts radiating at pulse number 1.

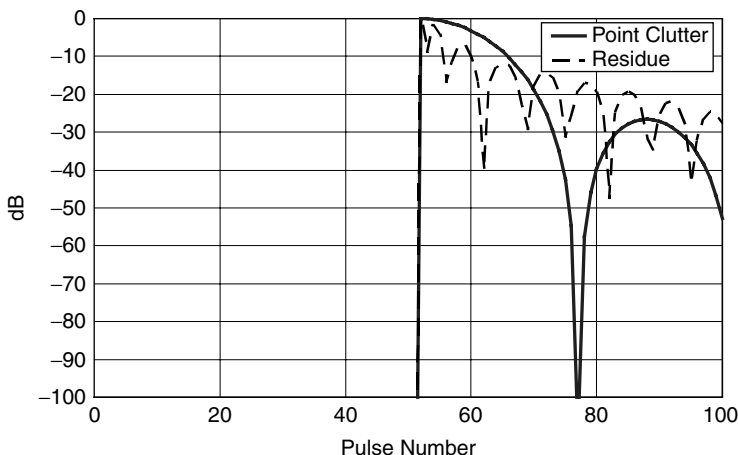


**FIGURE 2.50** Clutter input and residue from elliptic filter. Radar starts radiating at pulse number 51.

Figure 2.51 shows the effect of the returned signal if the point clutter exceeds the IF limit level by 6 dB. When the signal reaches the limit level, there is a step increase of residue of about 30 dB. TDWR uses clutter maps to normalize the residue from the strong points of clutter that exceed the limit level.

The weather mode of Airport Surveillance Radars is demonstrated by five-pulse finite impulse response (FIR) filters used in the ASR-11, an S-band radar used for air traffic control at airports. The design of the filters is primarily for Moving Target Detector (MTD) detection of aircraft, but special attention is given to providing flat passband response for accurate weather reflectivity estimation. The filter bank (for  $HBW = 17$ ) is pictured in Figure 2.52 and the coefficients are shown in Table 2.3.

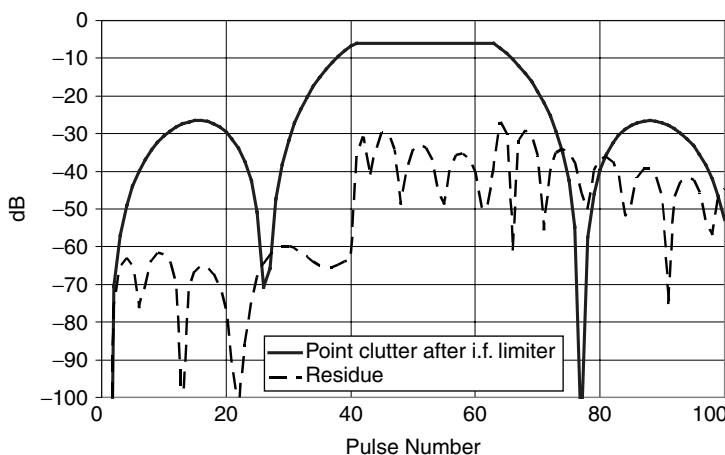


**FIGURE 2.51** Effect of limiting on elliptic filter response

**TABLE 2.3** ASR: Coefficients of ASR-11 5-Pulse Low-PRF Fir Filters

FILTER	Coefficient 1	Coefficient 2	Coefficient 3	Coefficient 4	Coefficient 5
20 dB	0.79812	-0.50687	-0.29297	-0.08340	0.11528
30 dB	0.67844	-0.62907	-0.28700	0.00815	0.24810
40 dB	0.50178	-0.80291	0.06899	0.30685	-0.06807
50 dB	0.39235	-0.78485	0.21613	0.37851	-0.20021
60 dB	0.28502	-0.75401	0.58529	-0.03661	-0.07956
70 dB	0.17766	-0.58440	0.70278	-0.35920	0.06322

Selection of filters is based on clutter amplitude information stored in a clutter map. The filters are selected on a range-cell by CPI basis.

These FIR clutter filters have the narrowest rejection notches that can be obtained with five pulses and the indicated level of fixed clutter rejection. However, the notches are significantly wider than those of the elliptic filters; thus, they will have greater bias for measurement of weather intensity when the weather radial velocity is zero.

For phased array radars, FIR filters similar to those described for the ASR-11 are applicable. The filters can be designed, if the time budget of the phased array radar allows, to utilize more than the five pulses per coherent processing interval (CPI) used by the ASR-11 radar. Using more pulses makes possible narrower rejection notches and thus less bias for estimates of precipitation with zero radial velocity.

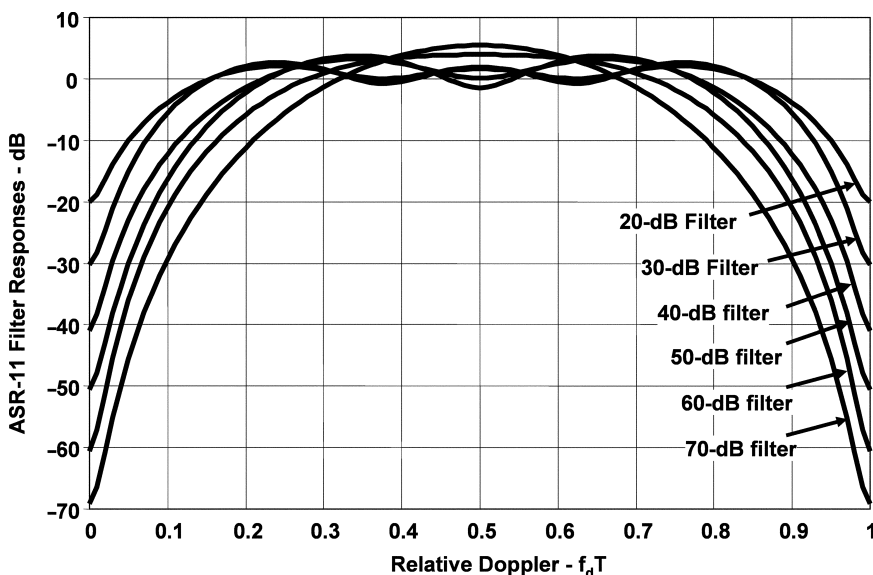


**FIGURE 2.52** Response of ASR-11 FIR filters low-PRF ( $f_r = 855$  pps) filters operating against fixed clutter with HBW = 17. The unambiguous doppler interval ( $fT = 1$ ) is 45.8 m/s for the parameters used to calculate this response.

## 2.10 CLUTTER FILTER BANK DESIGN

---

As discussed in Section 2.2, the MTD uses a waveform consisting of coherent processing intervals (CPIs) of  $N$  pulses, all at the same PRF and RF frequency. The PRF and possibly the RF are changed from one CPI to the next. With this constraint, only finite-impulse-response (FIR) filter designs are realistic candidates for the filter bank design. (Feedback filters require a number of pulses to settle after either the PRF or the RF is changed and thus would not be practical.)

The number of pulses available during the time when a surveillance radar beam illuminates a potential target position is determined by system parameters and requirements such as beamwidth, PRF, volume to be scanned, and the required data update rate. Given the constraint on the number of pulses on target, one must decide how many CPIs should occur during the time on target and how many pulses per CPI. The compromise is usually difficult. One wishes to use more pulses per CPI to enable the use of better filters, but one also wishes to have as many CPIs as possible. Multiple CPIs (at different PRFs and perhaps at different RF frequencies) improve detection and can provide information for true radial velocity determination.<sup>30</sup>

The design of the individual filters in the doppler filter bank is a compromise between the frequency sidelobe requirement and the degradation in the coherent integration gain of the filter. The number of doppler filters required for a given length of the CPI must be balanced between hardware complexity and the straddling loss at the crossover between filters. Finally, the requirement of providing a high degree of clutter suppression at zero doppler (land clutter) sometimes introduces special design constraints.

When the number of pulses in a CPI is large ( $\geq 16$ ), the systematic design procedure and efficient implementation of the fast Fourier transform (FFT) algorithm is particularly attractive. Through the use of appropriate weighting functions of the time-domain returns in a single CPI, the resulting frequency sidelobes can be readily controlled. Further, the number of filters (equal to the order of the transform) needed to cover the total doppler space (equal to the radar PRF) can be chosen independently of the CPI, as discussed below.

As the CPI becomes smaller ( $\leq 10$ ), it becomes important to consider special designs of the individual filters to match the specific clutter suppression requirements at different doppler frequencies in order to achieve better overall performance. While some systematic procedures are available for designing FIR filters subject to specific passband and stopband constraints, the straightforward approach for small CPIs is to use an empirical approach in which the zeros of each filter are adjusted until the desired response is obtained. An example of such filter designs is presented next.

**Empirical Filter Design.** An example of an empirical filter design for a six-pulse CPI follows. (The six pulses per CPI may be driven by system considerations, such as time-on-target.) Because the filter will use six pulses, only five zeros are available for the filter design; the number of zeros available is the number of pulses minus one. The filter design process consists of placing the zeros to obtain a filter bank response that conforms to the specified constraints. The example that follows was produced with an interactive computer program with which the zeros could be moved until the desired response was obtained. The assumed filter requirements are as follows:

- Provide a response of  $-66$  dB in the clutter rejection notch (relative to the peak target response) of the moving-target filters.

- Provide a response of  $-46$  dB for chaff rejection at velocities between  $\pm 20\%$  of the ambiguous doppler frequency range.
- In this design, only five filters will be implemented.
- Three of the five filters will reject fixed clutter and respond to moving targets. Two filters will respond to targets at zero doppler and its ambiguities. (With good fixed clutter rejection filters, it takes two or more coherent filters to cover the gap in response at zero velocity.)

With the above considerations, a filter bank can be constructed.

Figure 2.53a shows the filter designed to respond to targets in the middle of the doppler passband. The sidelobes near zero velocity are  $66$  dB down from the peak, thus providing good clutter rejection for clutter within  $5\%$  of zero doppler. The  $-46$  dB sidelobe provides chaff rejection to  $\pm 16\%$ . Because of the constraint of having only five zeros available, this filter could not provide  $-46$  dB rejection to  $\pm 20\%$ .

Figure 2.53b shows the filter that responds to targets as near as possible to zero doppler, while having a zero-doppler response of  $-66$  dB. Two zeros are placed near 0, providing  $-66$  dB response to clutter at 0. The filter sidelobes between 0.8 and 1.0 doppler provide the specified chaff rejection of  $46$  dB. A mirror image of this filter is used for the third moving doppler filter. (The mirror-image filter has coefficients that are complex conjugates of the original filter coefficients.)

Figure 2.53c shows the first filter designed for response at zero doppler. Considerations here are that the doppler straddling loss of the filter bank be minimized

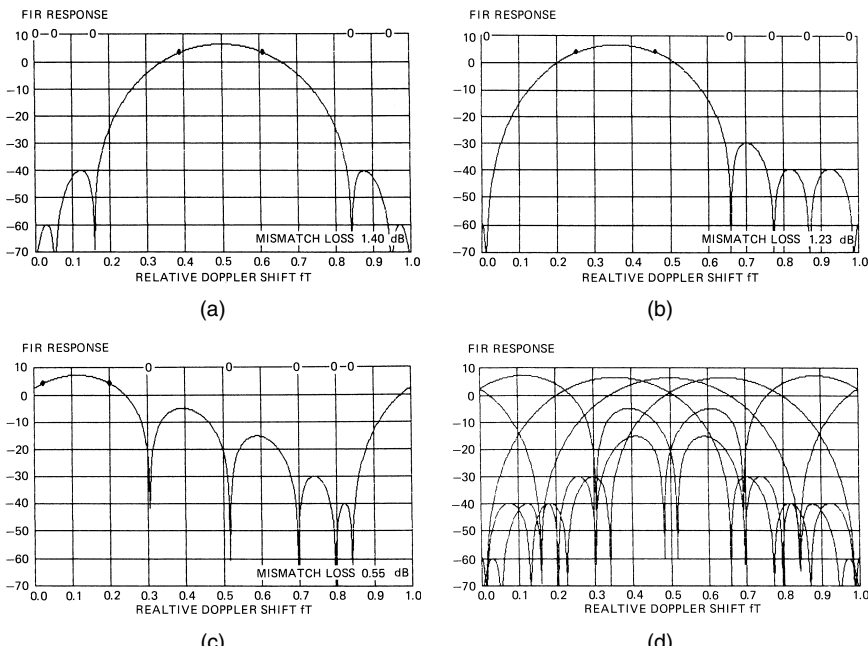


**FIGURE 2.53** Six-pulse filters for targets at (a)  $fT = 0.5$ , (b)  $fT = 0.3, fT = 0.8$ , and (c) combined response of complete bank of five six-pulse filters

(this dictates the location of the peak), that the response to chaff at 0.8 doppler be down 46 dB, and that the mismatch loss be minimized. Minimizing the mismatch loss is accomplished by permitting the filter sidelobes between 0.3 and 0.8 to rise as high as needed (lower sidelobes in this range increase the mismatch loss). The second zero-doppler filter is the mirror image of this one.

Figure 2.53d shows the composite response of the filter bank. Note that the filter peaks are fairly evenly distributed. The dip between the first zero-doppler filter and the first moving doppler filter is larger than the others, primarily because, under the constraints, it is impossible to move the first doppler filter nearer to zero velocity.

**Chebyshev Filter Bank.** For a larger number of pulses in the CPI, a more systematic approach to filter design is desirable. If a doppler filter design criterion is chosen that requires the filter sidelobes outside the main response to be below a specified level (i.e., providing a constant level of clutter suppression), while simultaneously minimizing the width of the filter response, a filter design based on the Dolph-Chebyshev distribution provides the optimum solution. Properties and design procedures based on the Dolph-Chebyshev distribution can be found in the antenna literature. An example of a filter design for a CPI of 9 pulses and a sidelobe requirement of 68 dB is shown in Figure 2.54. The peak filter response can be located arbitrarily in frequency by adding a linear-phase term to the filter coefficients.

The total number of filters implemented to cover all doppler frequencies is a design option trading straddling loss at the filter crossover frequencies against implementation complexity. An example of a complete doppler filter bank implemented with nine uniformly spaced filters is shown in Figure 2.55. The performance of this doppler filter bank against the clutter model considered in Figure 2.25 is shown in Figure 2.56. This graph shows the signal-to-clutter ratio improvement against clutter at zero doppler as a function of target doppler frequency. Only the response of the filter providing the greatest improvement is plotted at each target doppler.

For comparison the optimum curve from Figure 2.25 is shown by a broken line and thus provides a direct assessment of how well the Chebyshev filter design performs against a given clutter model. Also shown is the average SCR improvement for both the optimum and the Chebyshev filter bank.

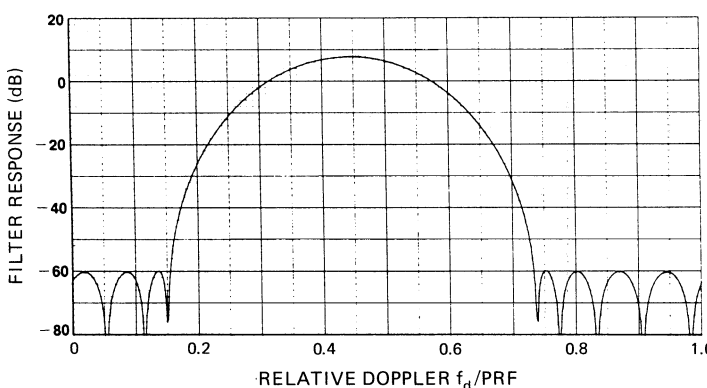
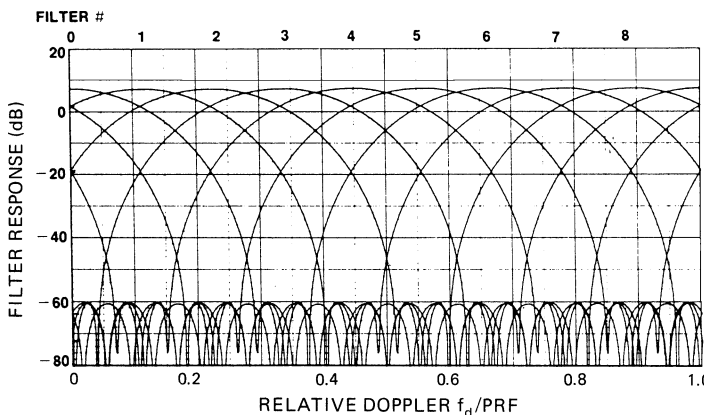


FIGURE 2.54 Chebyshev FIR filter design with 68 dB doppler sidelobes



**FIGURE 2.55** Doppler filter bank of 68 dB Chebyshev filters, CPI = 9 pulses

Finally, Figure 2.57 shows the average SCR improvement of the 68 dB Chebyshev doppler filter bank as well as the optimum curve (from Figure 2.26) as a function of the relative spectrum spread of the clutter. Owing to the finite number of filters implemented in the filter bank, the average SCR improvement will change by a small amount if a doppler shift is introduced into the clutter returns. This effect is illustrated by the cross-hatched region, which shows upper and lower limits on the average SCR improvement for all possible clutter doppler shifts. For a smaller number of filters in the doppler filter bank, this variation would be greater.

**Fast Fourier Transform Filter Bank.** For a large number of parallel doppler filters, hardware implementation can be simplified significantly through the use of the FFT algorithm. The use of this algorithm constrains all filters in the filter bank to

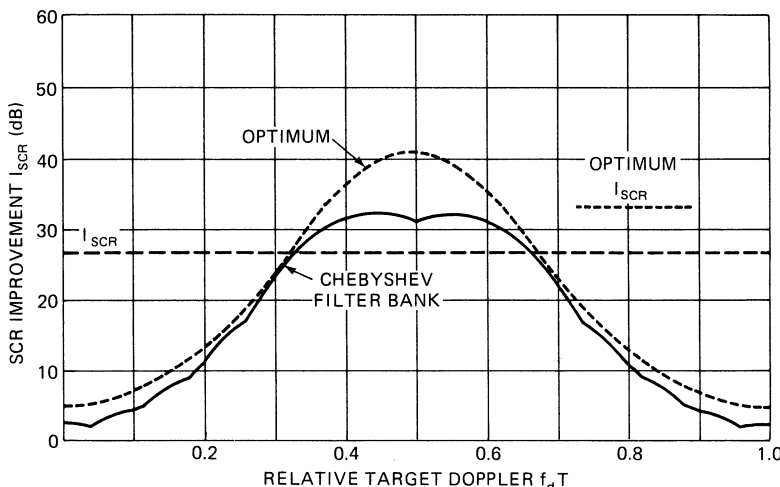


**FIGURE 2.56** SCR improvement of 68 dB Chebyshev doppler filter bank compared with the optimum

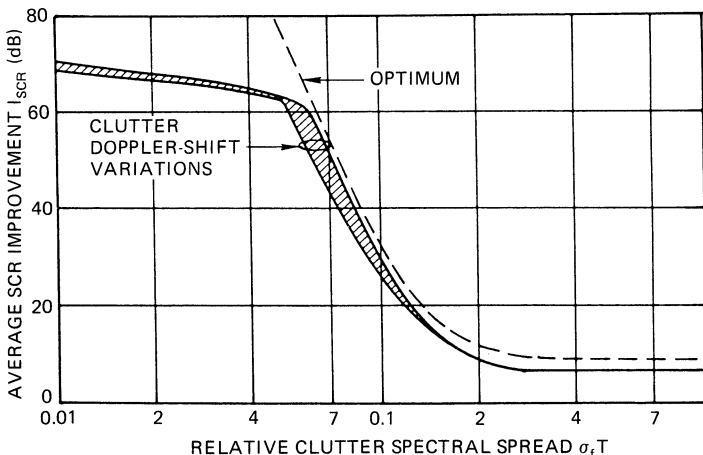


**FIGURE 2.57** Average SCR improvement for the 68 dB Chebyshev filter bank shown in Figure 2.55. CPI = 9 pulses. Optimum is from Figure 2.26.

have identical responses, and the filters will be uniformly spaced along the doppler axis. The number of filters implemented for a given size of the CPI can, however, be varied. For example, a greater number of filters can be realized by extending the received data with extra zero values (also known as zero padding) after the received returns have been appropriately weighted in accordance with the desired filter response (e.g., Chebyshev).

**Filter Bank Designs Using Constrained Optimization Techniques.** For a greater numbers of pulses in the CPI, and when the economy of the FFT implementation of a doppler filter bank can be replaced by a FIR implementation, more desirable FIR filter responses can be realized through the use of appropriate numerical digital filter design techniques. The goal is similar to that pursued with the empirical filter designs discussed earlier but filters with a large number of taps can be designed to exacting specifications.

As an example, consider the design of a doppler filter bank for an S band (3.0 GHz) radar using a CPI of  $N = 25$  pulses using a PRF of 6 kHz. Assume that the radar requirements call for a suppression of stationary land clutter by 80 dB and a suppression of moving clutter (rain) by 50 dB. For the filter design, a clutter attenuation 10 dB below these requirements will be needed to keep the sensitivity loss due to the clutter residue below 1 dB and also because each doppler filter will have a coherent gain of around  $10 \cdot \log_{10}(25) = 14$  dB, this must be added to the filter design specification as well. The total S-band doppler space for the above radar parameters is 300 m/s, and assuming that the land clutter suppression region has to be  $\pm 4$  m/s and that the moving clutter suppression region has to be  $\pm 30$  m/s, the constraint for all doppler filter designs normalized to their peak is as shown in Figure 2.58.

Using a signal processing toolbox developed by Dr. Dan P. Scholnik of the Naval Research Laboratory, a doppler filter bank meeting the above constraints was designed. The first filter, which has its peak located as close as possible to the left edge of the constraint box is shown in Figure 2.59, with the abscissa normalized to the total available doppler space.

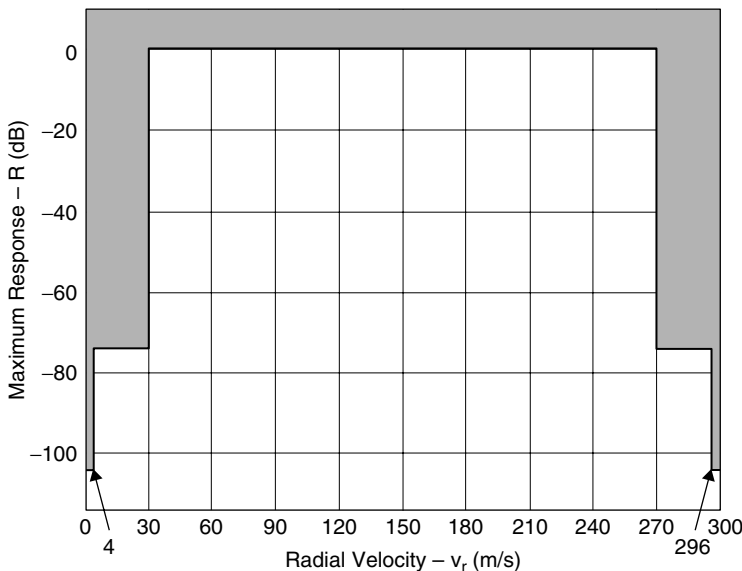


**FIGURE 2.58** Doppler filter design constraints

The mismatch loss of this filter is  $L_m = 1.29$  dB, which is well below that of a 105 dB Dolph-Chebyshev filter bank ( $L_m = 3.0$  dB). For the remaining filters, a relative spacing of  $D = 1/25 = 0.04$  was used, but this could be reduced in order to minimize doppler straddling losses. The third filter in the filter bank is shown in Figure 2.60.

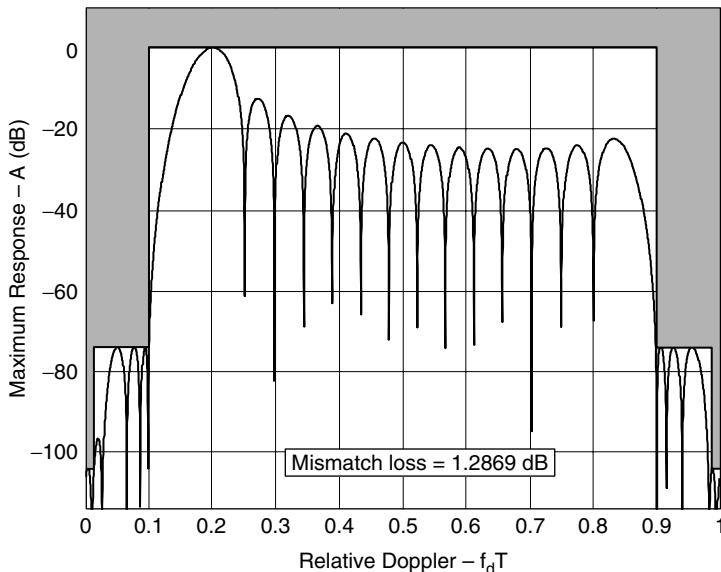


**FIGURE 2.59** Leftmost FIR filter in doppler filter bank design

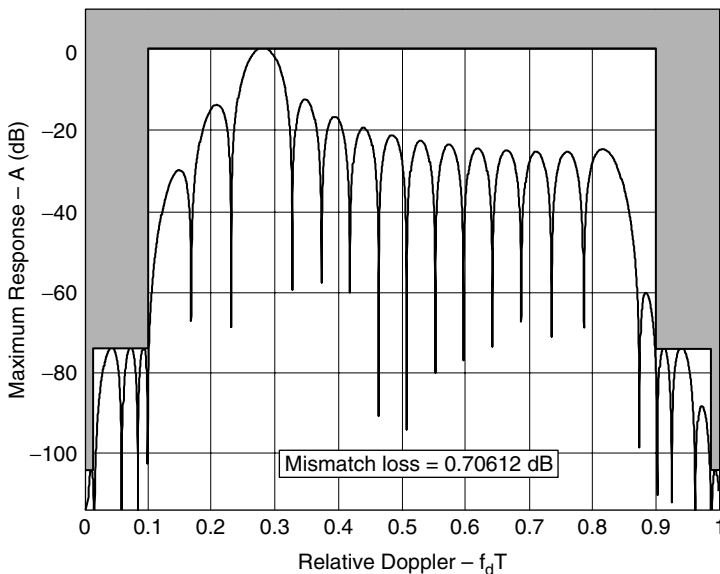


**FIGURE 2.60** Third FIR filter in doppler filter bank design

The mismatch loss has now been reduced to 0.71 dB. Finally, the complete doppler filter bank is shown in Figure 2.61. This filter bank could be augmented with additional filters around zero doppler, but these would not meet the design constraints discussed above. The main benefit of a customized doppler filter bank design, as

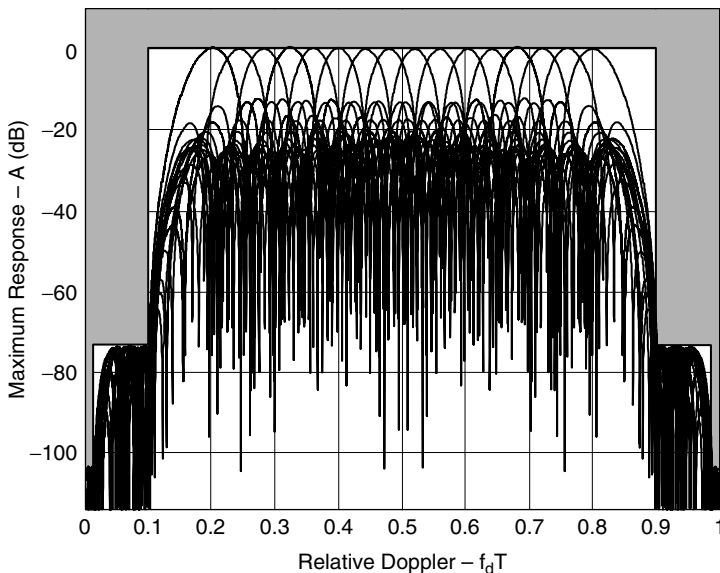


**FIGURE 2.61** Complete doppler filter bank design

described here, is its reduced mismatch loss. For the 16 filters in the above design, the average mismatch loss is  $\bar{L}_m = 0.66$  dB, a savings of 2.3 dB as compared to the alternative of a 105 dB weighted Dolph-Chebyshev filter bank.

## **2.11 PERFORMANCE DEGRADATION CAUSED BY RECEIVER LIMITING**

Elsewhere in this chapter (Sections 2.2 and 2.12, particularly) IF bandpass limiters have been discussed as (1) a means of preventing received clutter signals from exceeding the range of the A/D converters, (2) normalizing MTI clutter residue caused by system instabilities, and (3) normalizing residue due to the spectral spread of “fixed clutter” caused by either scanning or wind-blown motion. There are occasional clutter residue spikes when clutter exceeds the limit level, and in the past, the energy from these spikes of residue has been suppressed by further reduction of the limit level. When limiters have been used to normalize the energy of clutter residue spikes, the average improvement factor of the MTI systems drastically deteriorates. The equations for  $I$  (improvement factor) of a scanning radar in Section 2.6 are based on linear theory. Field measurements, however, have shown that many scanning multiple-delay MTI radar systems fall considerably short of the predicted performance. This occurs because the IF bandpass limiters have been used to suppress the energy of the residue spikes that are caused by the limiting action. Later in this section, it is shown that the use of a binary detection scheme, instead of a drastic reduction of the limit level, can be used to maintain a clutter rejection performance close to linear theory prediction in the resolution cells where clutter limiting occur.

An example of how limiting the dynamic range adjusts the residue is shown in the MTI PPI photographs shown in Figure 2.62. The range rings are at 5-mi intervals.

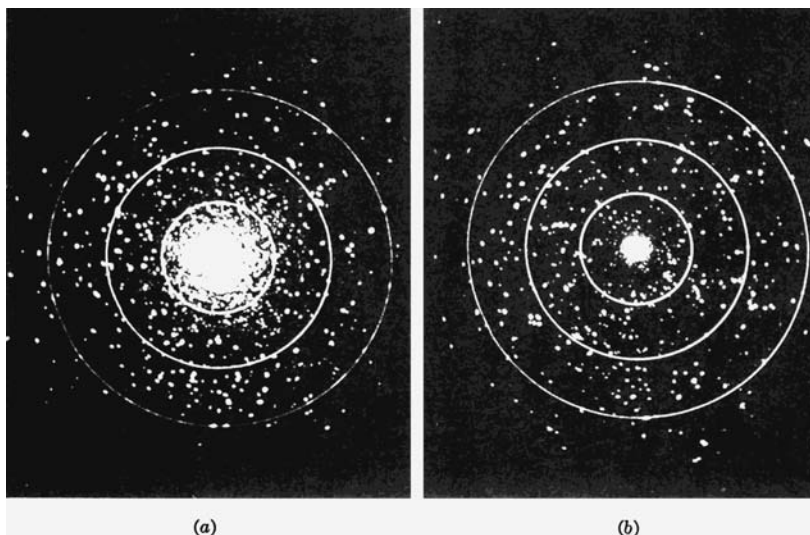


**FIGURE 2.62** Effect of limiters: (a) 18 dB improvement factor, 20 dB input dynamic range, and (b) 18 dB improvement factor, 14 dB input dynamic range

A number of birds are shown on the display. The residue from clutter in the left photograph is solid out to 3 nmi and then decreases until it is almost entirely gone at 10 nmi. The MTI improvement factor in both pictures is 18 dB, but the input dynamic range (peak signal-to-rms noise) to the canceler was changed from 20 to 14 dB between the two pictures. An aircraft flying over the clutter in the first 5 mi in the left-hand picture could not be detected, no matter how large its radar cross section. In the right-hand picture, the aircraft could be detected if the target-to-clutter cross-section ratio were sufficient. Although this example is from many years ago,<sup>31</sup> the principle is still the same, even though current MTI improvement factors are better by tens of dBs. Restriction of the IF dynamic range is still a very efficient way of normalizing clutter residue due to system instabilities or clutter spectral spread to system noise. This is true whether or not the radar uses pulse compression.

Prior to the development of modern clutter maps for controlling false alarms caused by clutter residue, or the more recent suggestion that binary integration can mitigate impulse-like residue,<sup>32</sup> the use of IF limiting was essential for false-alarm control in an MTI radar. Such limiting, however, seriously affects the mean improvement factor obtainable with a scanning-limited, multiple-delay canceler because of the increased spectral spread of the clutter that exceeds the limit level. Part of the additional clutter spectral components comes from the sharp discontinuity in the envelope of returns as the clutter reaches the limit level.<sup>33</sup> A time-domain example of this phenomenon is shown in Figure 2.63 for a radar with  $N = 16.4$  hits per beamwidth. On the left is a point target that does not exceed the limit level; on the right is a point target that exceeds the limit level by 20 dB. Note that, for this example,  $I$  degrades by 12.8 dB for the dual canceler and by 26.5 dB for the triple canceler. The exact result of this calculation depends on the assumed shape of the antenna pattern; for this example, a  $\frac{\sin(u)}{u}$  pattern terminated at the first nulls was assumed. There is a comparable improvement factor degradation due to spectral spreading of limited distributed clutter.<sup>34,35</sup> Figures 2.64, 2.65, and 2.66 show the expected mean improvement factor for two-, three-, and four-pulse cancelers as a function of  $\sigma/L$ , the ratio of the rms clutter amplitude to the limit level. Hits per one-way half-power beamwidth are indicated by  $N$ .

An example of clutter residue from simulated hard-limited distributed clutter is taken from Hall and Shrader.<sup>32</sup> Figure 2.67 shows a polar plot of part of a linear clutter sequence for a scanning radar with  $N = 20$  hits per beamwidth. This linear clutter sequence is 65 consecutive complex voltage returns from one range cell of distributed clutter. Figure 2.68 shows the phase and amplitude of this sequence.

If this clutter sequence were 40 dB stronger and passed through a 10 V IF limiter, only the phase information would remain. Each pulse would have a 10 V amplitude. When the resulting limited clutter sequence is passed through a three-pulse canceler (coefficients 1, -2, 1), the output residue appears as in Figure 2.69a. The corresponding pulse-to-pulse improvement factor is shown Figure 2.69b.

The expected three-pulse canceler improvement factor (from equation 2.27) for a linear system with  $N = 20$  is  $I_3 = n^4/3.84 = 46.2$  dB. In Figure 2.69b, it is seen that this level of  $I_3$  is achieved for most of the pulses, with only two pulses having very low values of  $I_3$ . The statistics for the distribution of  $I_3$  for the three-pulse canceler for hard-limited distributed clutter are shown in Figure 2.70.<sup>32</sup>

Note that for  $N = 20$ , less than 5% of the hard-limited samples have an improvement factor less than 24 dB, whereas almost 60% of the samples exceed the  $I_3$  expected for a linear system.

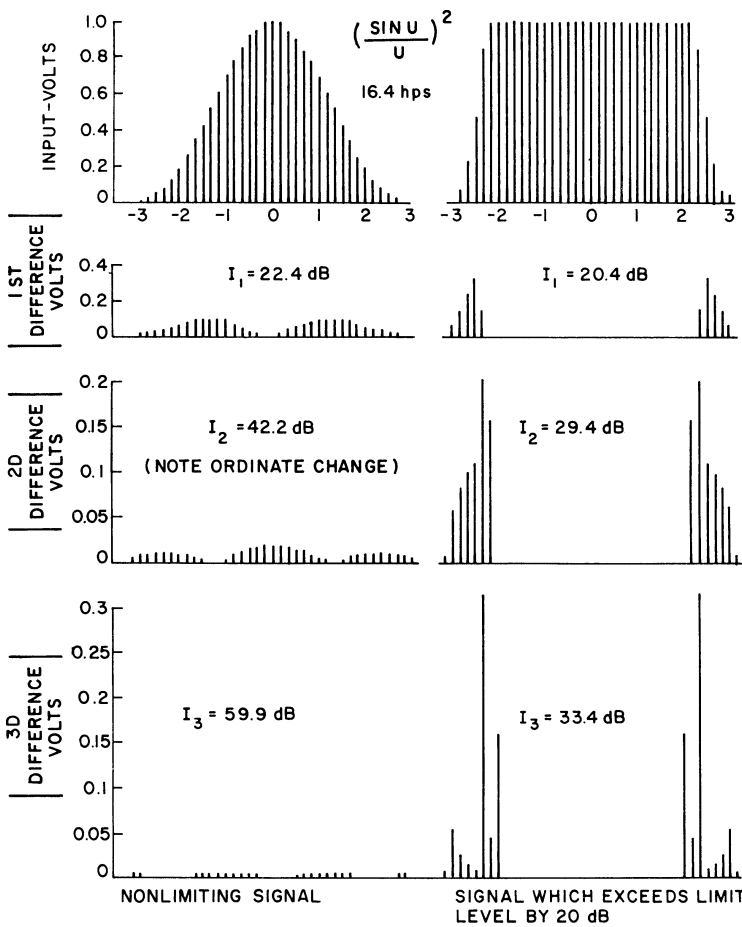
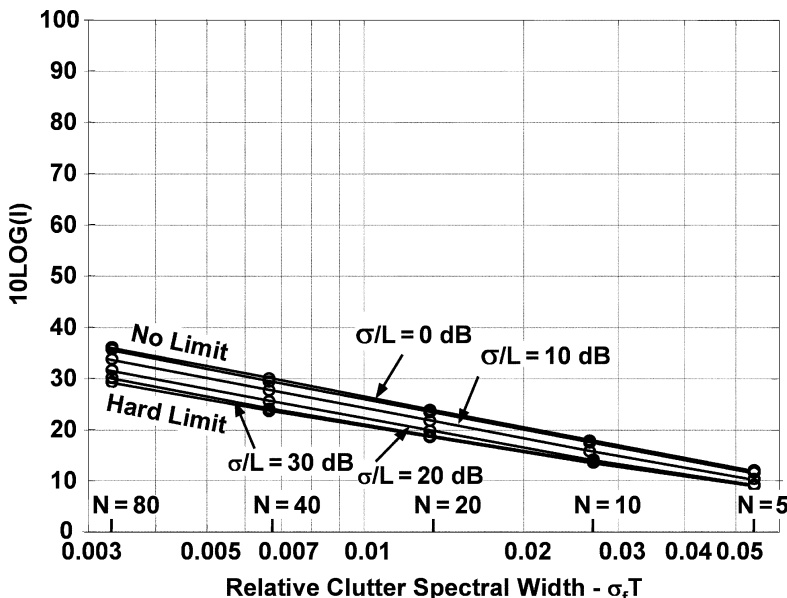


**FIGURE 2.63** Improvement factor restriction caused by a limiter

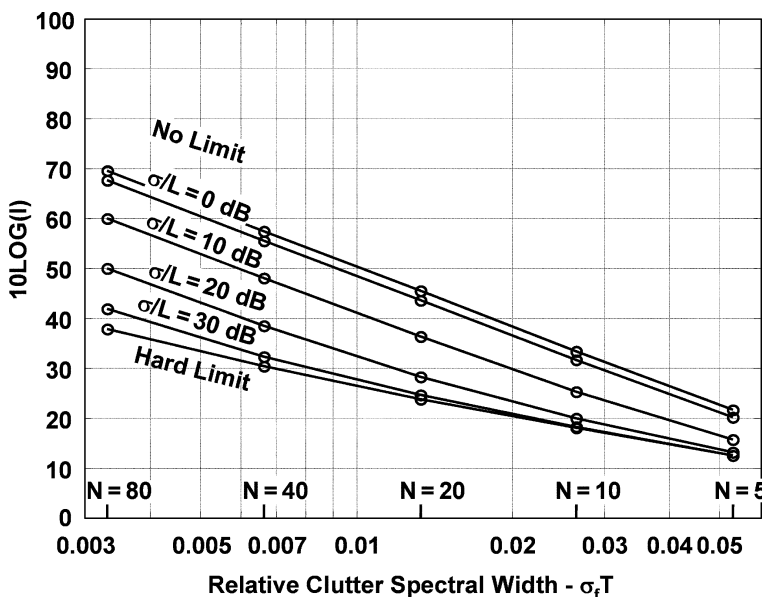
The time-domain illustration shown previously in Figure 2.69 leads to the conclusion of Hall and Shrader<sup>32</sup> that using an  $M$  out of  $N$  binary detector at the output of an MTI filter will preclude false alarms from the clutter residues caused by limiting.

Figure 2.71 shows, in addition to clutter residue, the returns from a target that was superimposed on the distributed clutter prior to the clutter-plus-target sequence passing through the IF limiting process. One can see that many of the individual pulse returns from the target exceed the detection threshold, whereas only four of the clutter residue pulses exceed the threshold.

To summarize: (1) The MTI improvement factor in a majority of limiting clutter cells exceeds the average improvement factor obtained with linear processing; (2) cells with poor MTI improvement factor can be rejected with binary detection processing; and, therefore, (3) excellent MTI performance can be obtained even in regions of clutter that exceed the IF dynamic range.



**FIGURE 2.64** Mean improvement factor restriction versus amount of limiting and clutter spectral spread for a two-pulse canceler (after T. M. Hall and W. W. Shrader<sup>32</sup> © IEEE 2007 and H. R. Ward and W. W. Shrader<sup>34</sup> © IEEE 1968)



**FIGURE 2.65** Mean improvement factor restriction versus amount of limiting and clutter spectral spread for a three-pulse canceler (after T. M. Hall and W. W. Shrader<sup>32</sup> © IEEE 2007 and H. R. Ward and W. W. Shrader<sup>34</sup> © IEEE 1968)

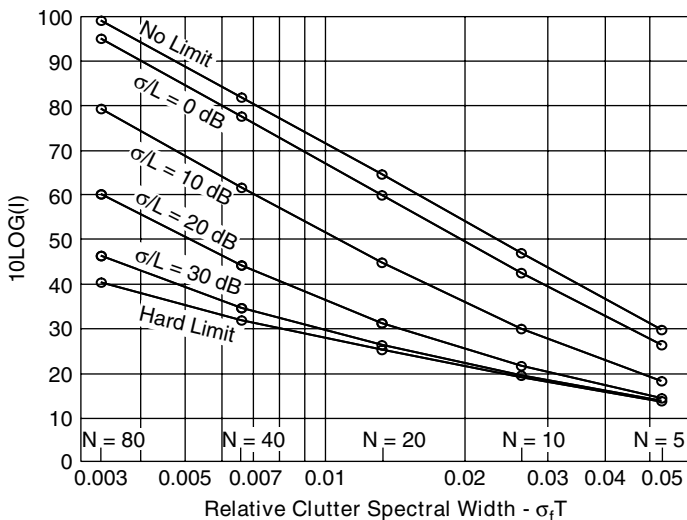


**FIGURE 2.66** Mean improvement factor restriction versus amount of limiting and clutter spectral spread for a four-pulse canceler (after T. M. Hall and W. W. Shrader<sup>32</sup> © IEEE 2007 and H. R. Ward and W. W. Shrader<sup>34</sup> © IEEE 1968)

Note that this discussion of binary detection is addressed to the spectral distribution of real clutter, that, when viewed in the time domain before limiting, has a smoothly varying change of the amplitude and phase of the clutter vector. This is distinct from clutter variations due to system instabilities that are noise-like, wherein the system dynamic range should be limited to prevent the instability residue from exceeding the system noise level.

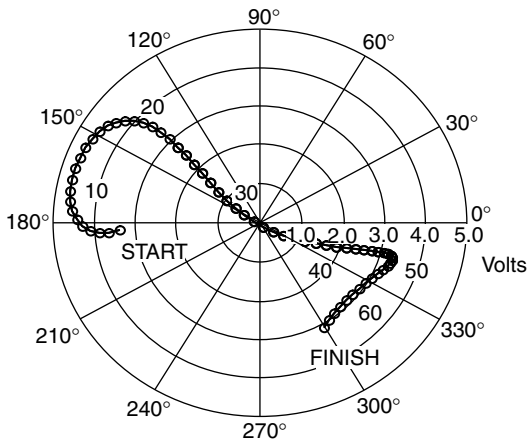


**FIGURE 2.67** Polar representation of a linear clutter sequence for 20 hits per beamwidth (after T. M. Hall and W. W. Shrader<sup>32</sup> © IEEE 2007)

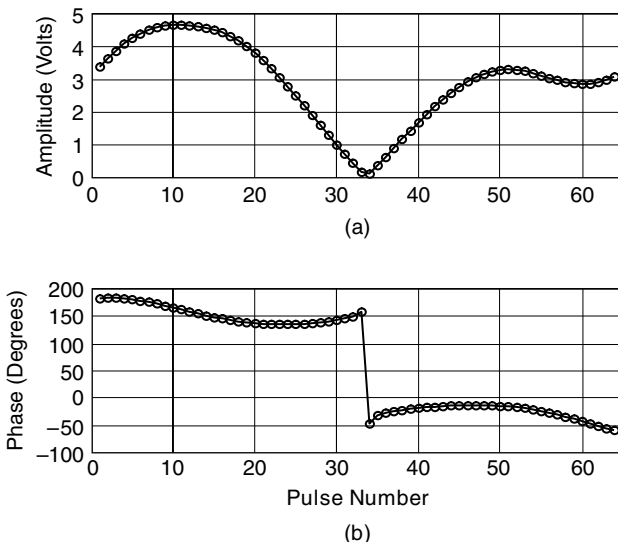


**FIGURE 2.68** Linear clutter sequence amplitude and phase for 20 hits per beamwidth (after T. M. Hall and W. W. Shrader<sup>32</sup> © IEEE 2007)

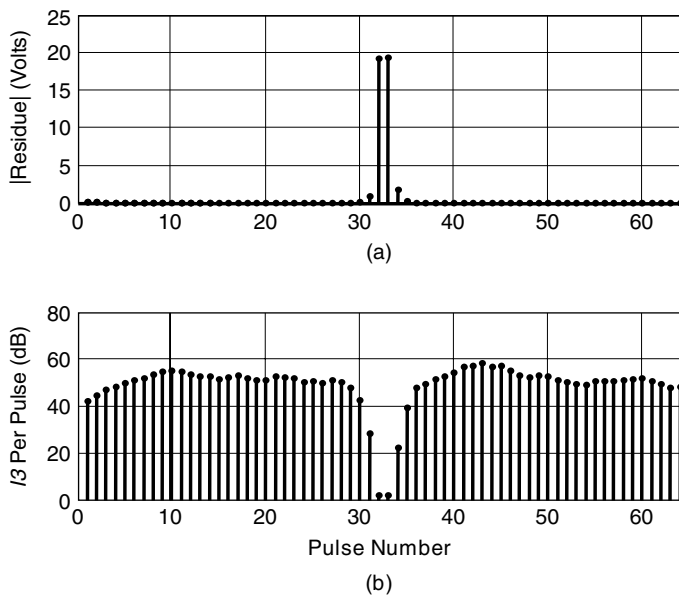


**FIGURE 2.69** (a) Three-pulse canceler residue and (b) improvement factor for hard-limited clutter sequence for  $N=20$  hits per beamwidth (after T. M. Hall and W. W. Shrader<sup>32</sup> © IEEE 2007)

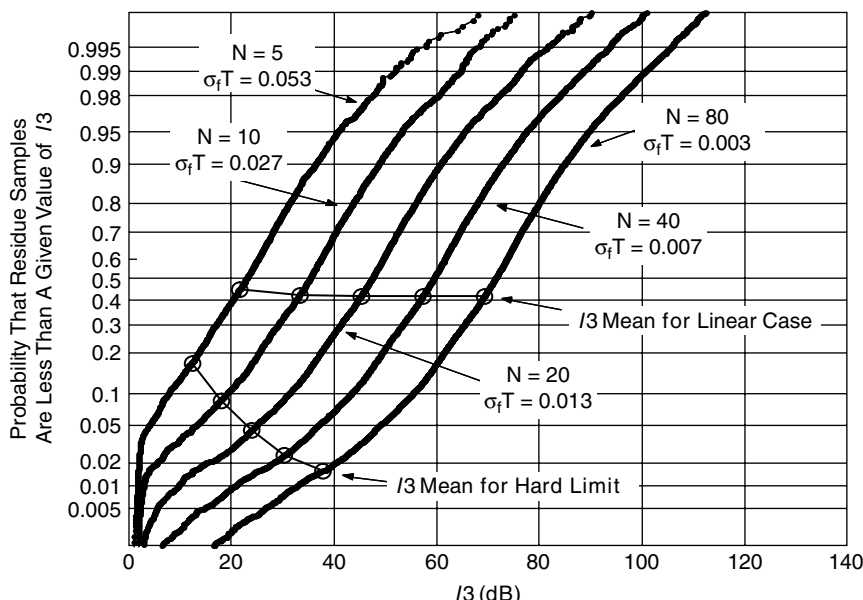


**FIGURE 2.70** Distribution of  $I_3$  and mean of  $I_3$  for hard-limited clutter for different numbers of scanning hits per beamwidth. For reference, the mean of  $I_3$  is also shown for linear processing. ( $I_3$  refers to the improvement factor of a three-pulse MTI canceler.) (after T. M. Hall and W. W. Shrader<sup>32</sup> © IEEE 2007)

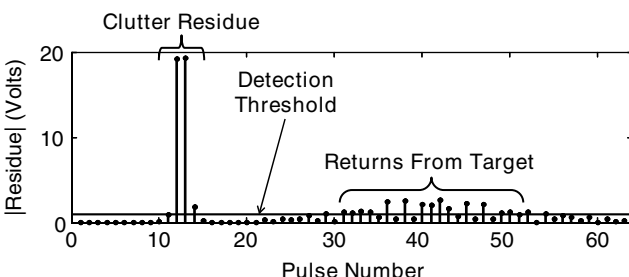


**FIGURE 2.71** After MTI processing of the hard-limited distributed clutter sequence ( $N=20$ ) and a target superimposed on the clutter sequence, the residue spikes are distinctly different from the target returns. A binary  $M$ -of- $N$  detector will reject the residue and keep the target. (after T. M. Hall and W. W. Shrader<sup>32</sup> © IEEE 2007)

## 2.12 RADAR SYSTEM STABILITY REQUIREMENTS

**System Instabilities.** Not only do the antenna motion and clutter spectrum affect the improvement factor that is attainable, but system instabilities also place a limit on MTI performance. These instabilities come from the stalo and coho, from the transmitter pulse-to-pulse frequency change if a pulsed oscillator and from pulse-to-pulse

phase change if a power amplifier, from the inability to lock the coho perfectly to the phase of the reference pulse, from time jitter and amplitude jitter on the pulses, and from quantization noise of the A/D converter.<sup>36,37</sup>

Phase instabilities will be considered first. If the phases of consecutive received pulses relative to the phase of the coho differ by, say, 0.01 rad, a limitation of 40 dB is imposed on  $I$ . The 0.01-rad clutter vector change would be equivalent to a target vector, 40 dB weaker than the clutter, being superimposed on the clutter, as shown in Figure 2.72.

In the power amplifier MTI system shown in Figure 2.73, pulse-to-pulse phase changes in the transmitted pulse can be introduced by the pulsed amplifier. The most common cause of a power amplifier introducing phase changes is ripple on the high-voltage power supply. Other causes of phase instability include ac voltage on a transmitter tube filament and uneven power supply loading, such as that caused by pulse-to-pulse stagger.

In the pulsed oscillator system, shown in Figure 2.74, pulse-to-pulse frequency changes result in phase run-out during the transmitted pulse. Phase run-out is the change of the transmitted pulse phase during the pulse duration with respect to the phase of the reference oscillator. If the coho locked perfectly to the end of the transmitted pulse, a total phase run-out of 0.02 rad during the transmitted pulse would then place an average limitation of 40 dB on the improvement factor attainable. Pulse-to-pulse frequency change in microwave oscillators is primarily caused by high-voltage power supply ripple. In the pulsed oscillator system, a pulse-to-pulse phase difference of 0.01 rad in locking the coho results in  $I$  limitation of 40 dB. (As noted elsewhere, frequency change during a pulse from a pulsed oscillator does not limit  $I$  if it repeats precisely pulse to pulse.)

The limitations on the improvement factor that are due to equipment instabilities in the form of frequency changes of the stalo and coho between consecutive transmitted pulses are a function of the range of the clutter. These changes are characterized in two ways. All oscillators have a noise spectrum. In addition, cavity oscillators, used because they are readily tunable, are microphonic, and thus their frequency may vary at an audio rate. The limitation on the improvement factor due to frequency changes is the difference in the number of radians that the oscillator runs through between the time of transmission and the time of reception of consecutive pulses. Thus, the improvement factor will be limited to 40 dB if  $2\pi\Delta f T = 0.01$  rad, where  $\Delta f$  is the oscillator frequency change between transmitted pulses and  $T$  is the transit time of the pulse to and from the target.

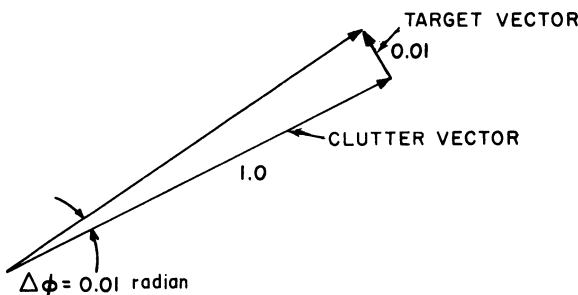


FIGURE 2.72 Phase instability

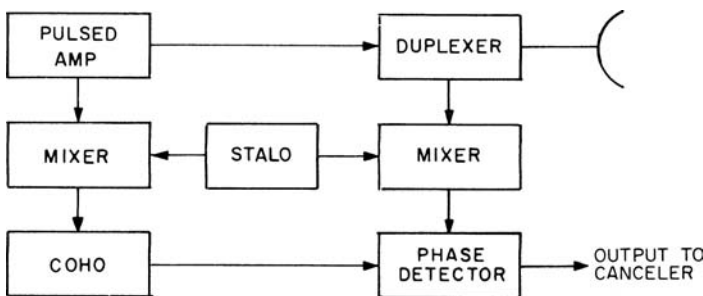


FIGURE 2.73 Power amplifier simplified block diagram

To evaluate the effects of oscillator phase noise on MTI performance, there are four steps. First, determine the single-sideband power spectral density of the phase noise as a function of frequency from the carrier.<sup>38,39</sup> Second, increase this spectral density by 6 dB. This accounts for a 3-dB increase because both sidebands of noise affect clutter residue, and a 3-dB increase because the oscillator contributes noise during both transmitting and receiving. Third, adjust the oscillator phase noise spectral density determined above due to the following three effects: (a) the self-cancellation of phase noise based on correlation resulting from the two-way range delay of the clutter of interest, (b) noise rejection due to the frequency response of the clutter filters, and (c) noise rejection due to the frequency response of the receiver passband. Finally, as the fourth step, integrate the adjusted spectral density of the phase noise across the entire passband. The result is the limitation on  $I$  due to the oscillator noise.

Rather than performing this integration of the residual noise numerically, a much simpler analysis can be carried out if both the oscillator phase noise characteristic and all of the adjustments to phase noise are approximated by straight lines on a decibel-versus-log frequency plot. This procedure becomes particularly simple when a MTI FIR filter using binomial coefficients is assumed. The locations along the frequency axis where the straight lines intersect are called *break frequencies*. This simplified procedure, which is similar to that presented in Vigneri et al.,<sup>40</sup> is described in the following paragraphs.

The first of the three adjustments—oscillator noise self-cancellation due to the range of the clutter of interest—reduces noise at the low frequencies by 20 dB per decade below the break frequency of  $f = 1/(\sqrt{2} \cdot T_R \cdot \pi)$ . Here  $T_R = 2 \cdot R/c$  is the time

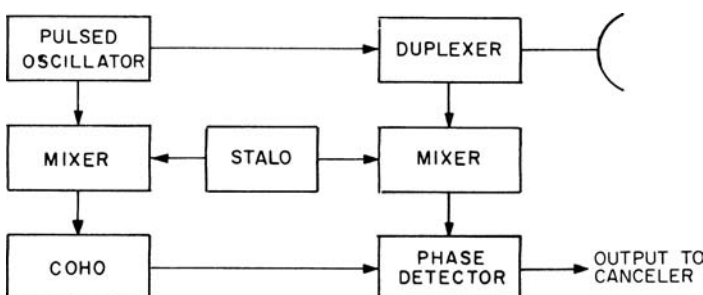
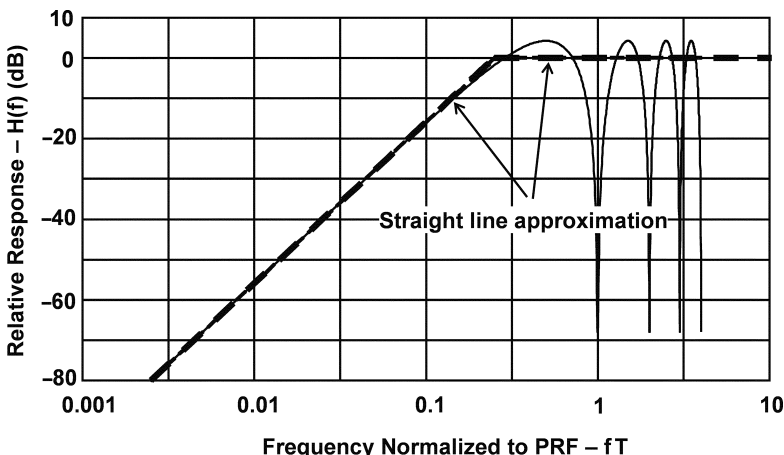


FIGURE 2.74 Pulsed oscillator simplified block diagram



**FIGURE 2.75** Straight-line approximation to two-delay binomial MTI

delay of the clutter return,  $R$  is the clutter range, and  $c$  is the speed of light. For the second adjustment due to the frequency response of the clutter filters, which as stated previously are assumed to be FIR cancelers with binomial weights, it is noted that the response at very low frequencies fall off at 20 dB per decade for one delay, 40 dB per decade for two delays, 60 dB per decade for three delays, etc. As an example, the approximation used for a two-delay MTI filter is shown in Figure 2.75. The MTI response has a peak value of  $4/\sqrt{6} \approx 4.26$  dB, resulting in an average noise gain of unity, and the straight line approximation follows the low frequency asymptote up to the 0 dB level, which occurs at  $fT = 0.249$ , and stays constant at the 0 dB level at all higher frequencies. The justification for the 0 dB approximation at the higher frequencies is that the oscillator spectral density is more nearly constant and the average over one period of the MTI response is unity. For other binomial coefficient MTI cancelers, the break frequencies for the start of the response falloff are  $fT = 0.225$  for one delay, 0.249 for two delays, 0.262 for three delays, and 0.271 for four delays.

For example, consider an oscillator with single-sideband phase-noise spectral density as shown in Figure 2.76. All oscillator noise contributions are assumed to be combined into this one curve. The single-sideband noise is increased by 3 dB because both sidebands affect system stability, and the power integration is only carried out for positive frequencies and by an additional 3 dB because the oscillator introduces noise in both the upconversion to the transmitted signal and in the receiver downconversion process.

Figure 2.77 shows the spectral modifications due to the system responses: (a) The first modification accounts for correlation due to the range to the clutter of interest [assumed clutter range is  $\approx 50$  nmi (92.6 km); thus, the break frequency is 365 Hz]. (b) Second, a three-pulse binomial-weighted canceler is assumed with the radar operating at a PRF of 360 Hz. Thus, the break frequency is  $0.249 \times 360 = 90$  Hz. (c) Third, the receiver passband is assumed to extend from  $-500$  kHz to  $+500$  kHz with respect to the IF center frequency (1 MHz total passband) at the  $-3$  dB points and determined by a two-pole filter. Thus, the receiver passband response falls off at 40 dB per decade from the break frequency at 500 kHz as shown.

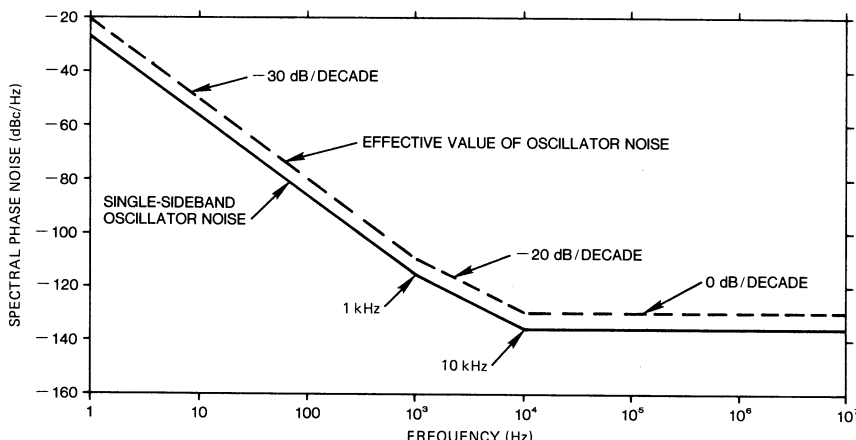


**FIGURE 2.76** Single-sideband phase-noise spectral density of a microwave oscillator and the effective noise density

The adjusted phase-noise spectral density is shown in Figure 2.78. The total noise power with respect to the carrier is determined by integration of the noise power under the curve. The equation for the power spectral density of any one segment as a function of frequency is

$$S(f) = S_1 \cdot \left( \frac{f}{f_1} \right)^\alpha \quad f_1 \leq f \leq f_2 \quad (2.42)$$

Here  $f_1$  and  $f_2$  are the start and end frequencies of the segment, respectively;  $S_1$  ( $\text{Hz}^{-1}$ ) is the phase noise spectral density relative to the carrier at the beginning of the segment and  $\alpha$  is the slope of the segment in  $\log_{10}$ -units per decade. Note that the

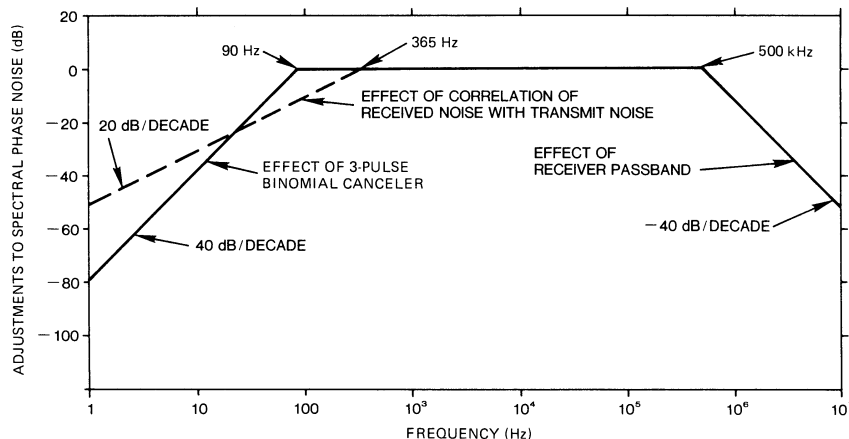


**FIGURE 2.77** Adjustments, based on system parameters (see text), to the phase noise of a microwave oscillator

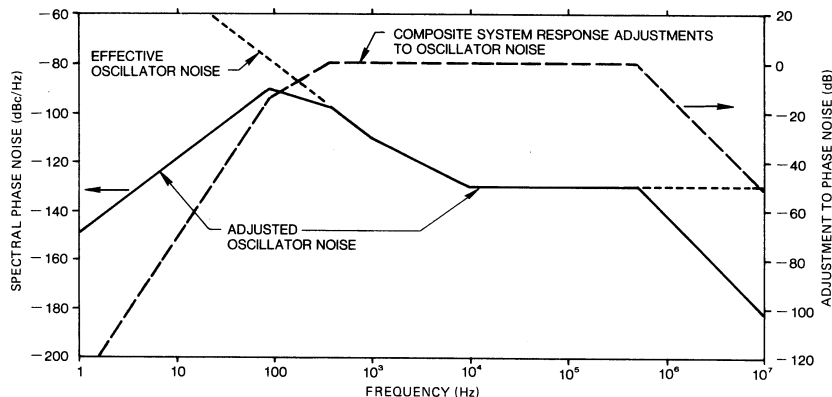


**FIGURE 2.78** Composite adjustments and adjusted phase-noise spectral density

dBc/Hz values in Figure 2.78 correspond to  $10 \cdot \log(S)$ . Further denoting the phase noise spectral density relative to the carrier at the end of the segment as  $S_2$  ( $\text{Hz}^{-1}$ ), the slope is defined by

$$\alpha = \frac{\log_{10}(S_2/S_1)}{\log_{10}(f_2/f_1)} \quad (2.43)$$

The slope in dB/decade is equal to  $10 \cdot \alpha$ . The noise power contribution corresponding to this segment is found as

$$P = \begin{cases} \frac{S_1}{f_1^\alpha} \cdot \frac{1}{1+\alpha} \cdot [f_2^{\alpha+1} - f_1^{\alpha+1}] & \text{all } \alpha \neq -1 \\ \frac{S_1}{f_1^\alpha} \cdot [\ln(f_2) - \ln(f_1)] & \alpha = -1 \end{cases} \quad (2.44)$$

Table 2.4 gives the integration for the example. When the integrated powers for all segments have been calculated, they are summed and then converted back to dBc. The final answer, -66.37 dBc, is the limit on  $I$  that results from oscillator noise. The limit on  $I_{\text{SCR}}$  (dB) is  $I$  (dB) plus target integration gain (dB).

**TABLE 2.4** Integration of the Phase-Noise Spectral Density of Figure 2.76 with Adjustments of Figure 2.77 as Shown in Figure 2.78

Segment	$f_1$ , Hz	$f_2$ , Hz	Slope, dB/dek	Slope $\alpha$	$S_1$ dBc/Hz	$S_2$ dBc/Hz	Integrated power	Integrated power, dBc
1	1	90	30.0	3	-149.4	-90.8	0.188e-7	-77.25
2	90	365	-10.0	-1	-90.8	-96.9	0.105e-6	-69.80
3	365	1,000	-30.0	-3	-96.9	-110.0	0.323e-7	-74.91
4	1.0e3	1.0e4	-20.0	-2	-110.0	-130.0	0.900e-8	-80.46
5	1.0e4	5.0e5	0.0	0	-130.0	-130.0	0.490e-7	-73.10
6	5.0e5	1.0e7	-40.0	-4	-130.0	-182.0	0.167e-7	-77.78
Total integrated noise power							0.231e-6	-66.37

Time jitter of the transmitted pulses results in degradation of MTI systems. Time jitter results in failure of the leading and trailing edges of the pulses to cancel, the amplitude of each uncancelled part being  $\Delta t/\tau$ , where  $\Delta t$  is the time jitter and  $\tau$  is the transmitted pulse length. The total residue power is  $2(\Delta t/\tau)^2$ , and therefore the limitation on the improvement factor due to time jitter is  $I = 20 \cdot \log[\tau/(\sqrt{2}\Delta t)]$  (dB). This limit on the improvement factor is based on a CW transmitter pulse and on the assumption that the receiver bandwidth is matched to the duration of the transmitted pulse. In a pulse compression system, the receiver bandwidth is wider by the time-bandwidth ( $B\tau$ ) product; thus the clutter residue power at each end of the pulse increases in proportion to the  $B\tau$  product. The limit on  $I$  for a chirp pulse compression system is then  $I = 20 \cdot \log[\tau/(\sqrt{2} \cdot \Delta t \cdot \sqrt{B \cdot \tau})]$ . For pulse compression systems employing phase-coded waveforms, the factor 2 in the preceding equation should be multiplied by the number of subpulses in the waveform. Thus, for example, the limit on  $I$  for a 13-pulse Barker code is

$$I = 20 \log [\tau/(\sqrt{2 \times 13} \cdot \Delta t \sqrt{13})] \text{ dB} \quad (2.45)$$

Pulse-width jitter results in one-half the residue of time jitter, and

$$I = 20 \log \frac{\tau}{\Delta PW \sqrt{B\tau}} \text{ dB} \quad (2.46)$$

where  $\Delta PW$  is pulse-width jitter.

Amplitude jitter in the transmitted pulse also causes a limitation of

$$I = 20 \log \frac{A}{\Delta A} \text{ dB} \quad (2.47)$$

where  $A$  is the pulse amplitude and  $\Delta A$  is the pulse-to-pulse change in amplitude. This limitation applies even though the system uses limiting before the canceler because there is always much clutter present that does not reach the limit level. With most transmitters, however, the amplitude jitter is insignificant after the frequency-stability or phase-stability requirements have been met.

Jitter in the sampling time in the A/D converter also limits MTI performance. If pulse compression is done prior to the A/D or if there is no pulse compression, this limit is

$$I = 20 \log \frac{\tau}{J \sqrt{B\tau}} \text{ dB} \quad (2.48)$$

where  $J$  is the timing jitter,  $\tau$  is transmitted pulse length, and  $B\tau$  is the time-bandwidth product. If pulse compression is done subsequent to the A/D converter, then the limitation is

$$I = 20 \log \frac{\tau}{JB\tau} \text{ dB} \quad (2.49)$$

The limitations on the attainable MTI improvement factor are summarized in Table 2.5. This discussion has assumed that the peak-to-peak values of these instabilities occur on a pulse-to-pulse basis, which is often the case in pulse-to-pulse staggered MTI operation. If it is known that the instabilities are random, the peak

**TABLE 2.5** Instability Limitations

Pulse-to-Pulse Instability	Limit on Improvement Factor
Oscillator phase noise	<i>See discussion in text.</i>
Transmitter frequency	$I = 20 \log [1/(\pi \Delta f \tau)]$
Stalo or coho frequency	$I = 20 \log [1/(2\pi \Delta f T)]$
Transmitter phase shift	$I = 20 \log (1/\Delta \phi)$
Coho locking	$I = 20 \log (1/\Delta \phi)$
Pulse timing	$I = 20 \log [\tau / (\sqrt{2} \Delta t \sqrt{B\tau})]$
Pulse width	$I = 20 \log [\tau / (\Delta PW \sqrt{B\tau})]$
Pulse amplitude	$I = 20 \log (A/\Delta A)$
A/D jitter	$I = 20 \log [\tau (J \sqrt{B\tau})]$
A/D jitter with pulse compression following A/D	$I = 20 \log [\tau / (JB\tau)]$
where	
$\Delta f$	interpulse frequency change
$\tau$	transmitted pulse length
$T$	transmission time to and from target
$\Delta \phi$	interpulse phase change
$\Delta t$	time jitter
$J$	A/D sampling time jitter
$B\tau$	time-bandwidth product of pulse compression system ( $B\tau$ = unity for CW pulses)
$\Delta PW$	pulse-width jitter
$A$	pulse amplitude, $V$
$\Delta A$	interpulse amplitude change

values shown in these equations can be replaced by the rms pulse-to-pulse values, which gives results essentially identical to Steinberg's results.<sup>41</sup>

If the instabilities occur at some known frequency, e.g., high-voltage power supply ripple, the relative effect of the instability can be determined by locating the response on the velocity response curve for the MTI system for a target at an equivalent doppler frequency. If, for instance, the response is 6 dB down from the maximum response, the limitation on  $I$  is about 6 dB less severe than indicated in the equations in Table 2.5. If all sources of instability are independent, as would usually be the case, their individual power residues can be added to determine the total limitation on MTI performance.

Intrapulse frequency or phase variations do not interfere with good MTI operation provided they repeat precisely from pulse to pulse. The only concern is a loss of sensitivity if phase run-out during the transmitted pulse or mistuning of the coho or stalo permits the received pulses to be significantly detuned from the intended IF frequency. If a 1-rad phase run-out during the pulse is permitted, the system detuning may be as large as  $1/(2\pi\tau)$  Hz with no degradation of MTI performance.

To give an example of interpulse stability requirements, consider a 3000-MHz radar transmitting a CW pulse of duration  $\tau = 2 \mu s$  and the requirement that no single system instability will limit the MTI improvement factor attainable at a range of 100 nmi to less than 50 dB, a voltage ratio of 316:1. The rms pulse-to-pulse transmitter frequency change (if a pulsed oscillator) must be less than

$$\Delta f = \frac{1}{316\pi\tau} = 504 \text{ Hz} \quad (2.50)$$

which is a stability of about 2 parts in  $10^7$ .

The rms pulse-to-pulse transmitter phase-shift change (if a power amplifier) must be less than

$$\Delta\phi = \frac{1}{316} = 0.00316 \text{ rad} = 0.18^0 \quad (2.51)$$

The stalo or coho frequency change in the interpulse period must be less than

$$\Delta f = \frac{1}{316(2\pi)(100 \times 12.36 \times 10^{-6})} = 0.4 \text{ Hz} \quad (2.52)$$

which is a stability of 1 part in  $10^{10}$  for the stalo (at about 3 GHz) and 1 part in  $10^8$  for the coho (assuming a 30-MHz IF frequency).

The coho locking (if a pulsed oscillator system) must be within

$$\Delta\phi = \frac{1}{316} = 0.00316 \text{ rad} = 0.18^0 \quad (2.53)$$

The pulse timing jitter must be less than

$$\Delta t = \frac{\tau}{316\sqrt{2}\sqrt{1}} = \frac{2 \times 10^{-6}}{316\sqrt{2}} = 4.5 \times 10^{-9} \text{ s} \quad (2.54)$$

The pulse-width jitter must be less than

$$\Delta PW = \frac{\tau}{316\sqrt{1}} = \frac{2 \times 10^{-6}}{316} = 6 \times 10^{-9} \text{ s} \quad (2.55)$$

The pulse amplitude change must be less than

$$\frac{\Delta A}{A} = \frac{1}{316} = 0.00316 = 0.3 \text{ percent} \quad (2.56)$$

The A/D sampling time jitter must be less than

$$J = \frac{\tau}{316\sqrt{1}} = \frac{2 \times 10^{-6}}{316} = 6 \times 10^{-9} \text{ s} \quad (2.57)$$

Of the above requirements, oscillator phase noise may dominate. However, in systems with large bandwidths (short compressed pulses), the timing jitter requirements become significant and may require special clock regeneration circuitry at key system locations.

**Effect of Quantization Noise on Improvement Factor.** Quantization noise, introduced in the A/D converter, limits the attainable MTI improvement factor. Consider a conventional video MTI system, as shown in Figure 2.79. Because the peak signal level is controlled by the linear-limiting amplifier, the peak excursion of the phase-detector output is known, and the A/D converter is designed to cover this excursion. If the A/D converter uses  $N$  bits and the phase-detector output is from  $-1$  to  $+1$ , the quantization interval is  $2/(2^N - 1)$ . The rms value of the signal-level deviation

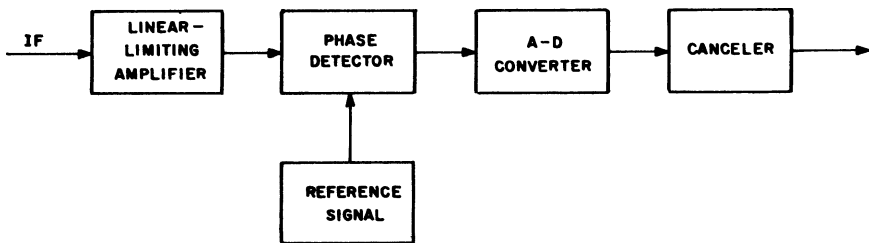


FIGURE 2.79 Digital MTI consideration

introduced by the A/D converter is  $2/[(2^N - 1)\sqrt{12}]$ . The limit on the MTI improvement factor that this imposes on a signal reaching the full excursion of the phase detector is found by substituting in the following equation from Table 2.5:

$$I = 20 \log \frac{A}{\Delta A} = 20 \log \left\{ \frac{1}{[(2^N - 1)\sqrt{3.0}]} \right\} = 20 \log [(2^N - 1)\sqrt{3.0}] \quad (2.58)$$

Because two quadrature channels contribute independent A/D noise, the average limit on the improvement factor of a full-range signal is

$$I = 20 \log \left[ (2^N - 1) \sqrt{\frac{3.0}{2}} \right] = 20 \log [(2^N - 1)\sqrt{1.5}] \quad (2.59)$$

If the signal does not reach the full excursion of the A/D converter, which is normally the case, then the quantization limit on  $I$  is proportionately more severe. For example, if the system is designed so that the mean level of the strongest clutter of interest is 3 dB below the A/D converter peak, the limit on  $I$  would be  $20 \cdot \log_{10}[(2^N - 1) \cdot \sqrt{0.75}]$ . (This is tabulated in Table 2.6.)

This discussion of A/D quantization noise has assumed perfect A/D converters. Many A/D converters, particularly under high-slew-rate conditions, are less than perfect. This, in turn, leads to system limitations more severe than predicted here (see Section 2.13).

TABLE 2.6 Typical Limitation on  $I$  Due to A/D Quantization

Number of Bits, $N$	Limit on MTI Improvement Factor $I$ , dB
10	59.0
11	65.0
12	71.0
13	77.0
14	83.0
15	89.1
16	95.1

**Pulse Compression Considerations.**<sup>†</sup> When an MTI system is used with pulse compression, the system target detection capability in clutter may be as good as a system transmitting the equivalent short pulse, or the performance may be no better than a system transmitting the same length CW pulse. The kind of clutter environment, the system instabilities, and the signal processing utilized determine where the system performance will fall between the above two extremes. Unless provision is incorporated for coping with system instabilities and clutter spectral spread, the MTI pulse compression system may fail to work at all in a clutter environment.

Ideally, a pulse compression receiver coupled with an MTI would appear as in Figure 2.80a.<sup>‡</sup> If the pulse compression system was perfect, the compressed pulse would look as if the radar had transmitted and received a short pulse, and MTI processing could proceed as if the pulse compression had not existed. In practice, the compressed pulse will have time sidelobes from three basic causes. The first is waveform and system design, which includes components that may be nonlinear with frequency, etc. These sidelobes will be stable. That is, they should repeat precisely on a pulse-to-pulse basis and thus will cancel in the MTI canceler. It is assumed that the radar system is fully coherent as required by rule 3 in Section 2.17. The second cause of pulse compression sidelobes is system instabilities, such as noise on local oscillators, transmitter time jitter, transmitter tube noise, and A/D converter jitter. These sidelobes are noise-like and are proportional to the clutter amplitude. They will not cancel in the MTI canceler. The third source of sidelobes is high-frequency ripple in the transmitter power supply.

If the transmitter power supply incorporates high-frequency ac-dc and/or dc-dc converters, and if the converter frequency components are not sufficiently filtered, there will be discrete time sidelobes, offset from the clutter in range, as predicted by paired-echo theory.<sup>42</sup> The paired-echo sidelobes will also have a doppler frequency equal to the converter frequency. This frequency ( $f_{\text{conv}}$ ) will alias into the PRF ( $f_r$ ) doppler interval at the frequency ( $f_{\text{dop}}$ ) [ $f_{\text{dop}} = \text{modulo}(f_{\text{conv}}, f_r)$ ]. These sidelobes will not cancel unless the high-frequency converters are synchronized to a multiple of the PRF, in which case  $f_{\text{dop}} = 0$ .

Assume that the noise-like component of the sidelobes is down 50 dB from the peak transmitted signals. This noise-like component will not cancel in the MTI system, and therefore, for each clutter area that exceeds the system threshold by 50 dB or more, the residue will exceed the detection threshold. If the clutter exceeds the threshold by 70 dB, the residue from the MTI system will exceed the detection threshold by 20 dB, eliminating the effectiveness of the MTI. Figure 2.80b shows a sketch of this effect.

To ensure that the noise-like pulse-compression sidelobes will not exceed the system noise after the MTI canceler, the system stability budget must ensure that the instability sidelobe level is lower than the dynamic range of the receiving system. The receiving system dynamic range is ultimately determined (in a well-designed system) by the IF

<sup>†</sup> All signal processing following the A/D detector is done digitally. It is more meaningful, however, to describe and depict the processing in an analog manner.

<sup>‡</sup> The IF bandpass limiter [Radar Handbook, 2nd Ed., pp. 3.30–3.32] shown in this and subsequent diagrams has an amplitude output characteristic that is linear for input signal voltages from noise level to within 6 dB of the limiter output maximum voltage and then transitions smoothly to the maximum output voltage.<sup>32</sup> The phase of the input signal is precisely preserved. These limiter characteristics exist whether the filter is implemented in analog circuitry or a digital algorithm.

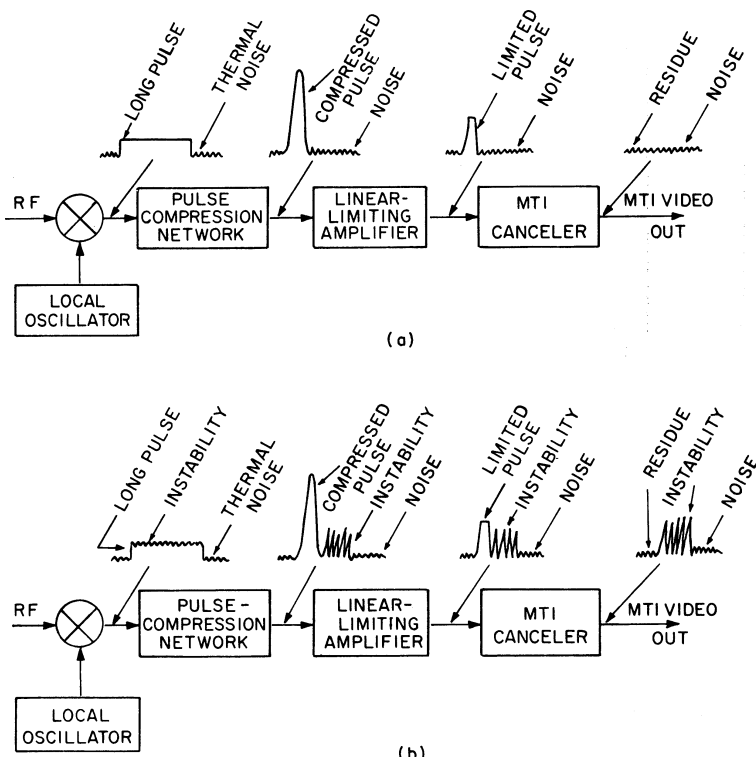


**FIGURE 2.80** Pulse compression with MTI: (a) ideal but difficult-to-achieve combination and (b) effect of oscillator on transmitter instabilities

bandpass limiter that precedes the A/D converter. If system instabilities cannot be controlled to be less than the system dynamic range, then the system dynamic range should be decreased. (An alternative to decreasing the dynamic range is to depend on a cell-averaging constant false alarm rate (CA-CFAR) processor after the signal processing to provide a threshold that rides over the residue noise, but the efficacy of this method depends on the residue noise being completely noise-like, which is unlikely.)

After addressing the unstable pulse-compression sidelobes, it is still necessary to control detections from residue caused by the spectral spread of the clutter or by low frequency transmitter power supply ripple. This can be accomplished by limiting the maximum signal amplitude at the input to the canceler. The process described above is depicted in Figure 2.81.

One approach that has been successful in achieving the maximum MTI system performance attainable within the limits imposed by system and clutter instabilities

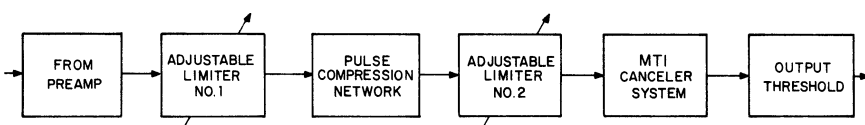


**FIGURE 2.81** Practical MTI pulse-compression combination

is shown in Figure 2.81. (Transmitter noise will be used in the following discussion to represent all possible system instabilities that create noise-like pulse-compression time sidelobes.)

Limiter 1 is set to limit the system dynamic range to the range between peak clutter and clutter instability noise. Limiter 2 is set so that the dynamic range at its output is equal to the expected MTI improvement factor as limited by clutter spectral spread or low-frequency transmitter power supply ripple. These limiter settings cause the residue due to transmitter noise and the residue due to other instabilities, such as quantization noise and internal-clutter motion, each to be equal to front-end thermal noise at the canceler output. This allows maximum sensitivity without an excessive false-alarm rate. Limiter 1 is a very efficient constant-false-alarm-rate device against system instabilities because it suppresses the instability noise in direct proportion to the clutter signal strength but does not suppress at any time when the clutter signal is not strong. Although the limiters cause partial or complete suppression of some desired targets in the clutter areas, no targets are suppressed that could otherwise have been detected in the presence of clutter residue at the system output if the limiters had not been used.

As a specific example, consider a system with a pulse-compression ratio of about 30 dB and system instability noise approximately 28 dB below the carrier power. Assume that the MTI canceler improvement factor is 30 dB, limited by clutter spectral spread. With the above system parameters, a receiver system that will provide the maximum obtainable performance is shown in Figure 2.82. At the output of the pulse-compression network, the system instability noise will be equal to or less than thermal noise for either distributed clutter or point clutter, and the peak clutter signals will vary from about 28 dB above thermal noise for evenly distributed clutter to 58 dB above thermal noise for strong point clutter.

Because the MTI canceler is expected to attenuate clutter by 30 dB, the second limiter is provided to prevent the residue from strong clutter from exceeding the threshold. Without the second limiter, a strong-point reflector that was 58 dB above noise at the canceler input would have a residue 28 dB above noise at the canceler output. This would be indistinguishable from an aircraft target.

If the transmitter noise were 15 dB less than assumed above, the first limiter would be set 43 dB above thermal noise and much less target suppression would occur. Thus target detectability would improve in and near the strong clutter areas even though the MTI improvement factor was still limited to 30 dB by internal-clutter motion.

In summary, the noise-like pulse compression sidelobes and the duration of the uncompressed pulse dictate how effective a pulse-compression MTI system can be. Systems have been built in which transmitter noise and long uncompressed pulses combined to make the systems incapable of detecting aircraft targets in or near land clutter. Some existing pulse-compression systems have not deliberately provided the

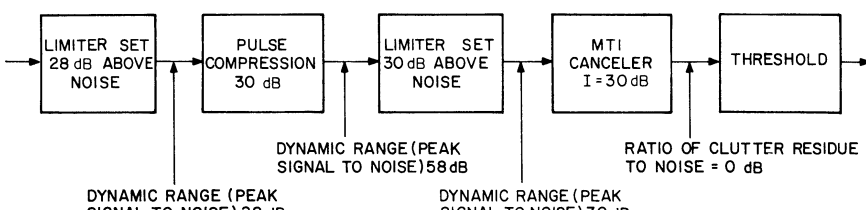


FIGURE 2.82 MTI with pulse compression

two separate limiters described above, but the systems work because dynamic range is sufficiently restricted by circuit components. Other systems, such as those that deliberately hard-limit before pulse compression for CFAR reasons, do not have clutter residue problems but suffer from significant target suppression in the clutter areas.

An alternative to the use of limiters is the use of clutter maps in conjunction with the CA-CFAR. Clutter maps work well for stationary radars operating at fixed frequencies, but are less effective for other radars. The CA-CFAR is useful, even for a system with IF limiters, because there will be small variations (on the order of a few dB) in the combination of clutter residue and system noise. To reemphasize, however, without the limiters, there may be tens of dB's difference between clutter residue and system noise.

## **2.13 DYNAMIC RANGE AND A/D CONVERSION CONSIDERATIONS**

---

The accurate conversion of the radar IF signal into a digital representation of the complex envelope is an important step in the implementation of a modern digital signal processor. This analog-to-digital (A/D) conversion must preserve the linearity of amplitude and phase over the required dynamic range, have a small effect on overall radar system noise temperature, and be free from undesired spurious responses.

Advances in A/D converter technology is now making it possible to directly convert an analog IF signal into a corresponding digital complex representation, rather than going through the intermediate step of first downconverting the IF signal into baseband in-phase (I) and quadrature (Q) components and subsequently using a separate A/D converter in each of these two channels.

A flow chart of a direct IF A/D converter is illustrated in Figure 2.83 along with spectral representations of the signal throughout the conversion process. The IF input centered at the frequency  $f_{IF}$  is first passed through a bandpass filter to ensure that negligible aliasing will occur during the subsequent A/D conversion process. On the right in Figure 2.83, the top graph shows the positive and negative parts of the signal spectrum at the IF filter output. The positive part of this spectrum corresponds to the complex envelope, which needs to be translated into the digital I and Q representation. This filter output becomes the input to the A/D converter operating at a sampling rate of  $f_{AD}$ . The spectrum of the A/D converter output is again shown, and it is obtained simply by replicating the original IF spectrum from minus infinity to plus infinity with a period of  $f_{AD}$ . In this example, an A/D conversion rate of  $f_{AD} = \frac{4}{3} \cdot f_{IF}$  is assumed. The optimum choice of the A/D converter sampling rate ensures that the negative part of the spectrum has the smallest possible overlap with the positive part of the spectrum.

The smallest possible overlap occurs when the A/D sampling rate is related to the radar IF frequency as follows<sup>43</sup>:

$$f_{AD} = \frac{4 \cdot f_{IF}}{2 \cdot M - 1} \quad (2.60)$$

where  $M$  is an integer greater than 1. Thus, optimum sampling rates are  $4f_{IF}$ ,  $1.3333f_{IF}$ ,  $0.8f_{IF}$ ,  $0.57f_{IF}$ , ... etc. The corresponding maximum unaliased (or Nyquist) bandwidth is  $B_{NQ} = f_{AD}/2$ . This value is, therefore, the maximum allowable cutoff bandwidth of the IF bandpass filter at the input to the A/D converter. It is not strictly necessary to use

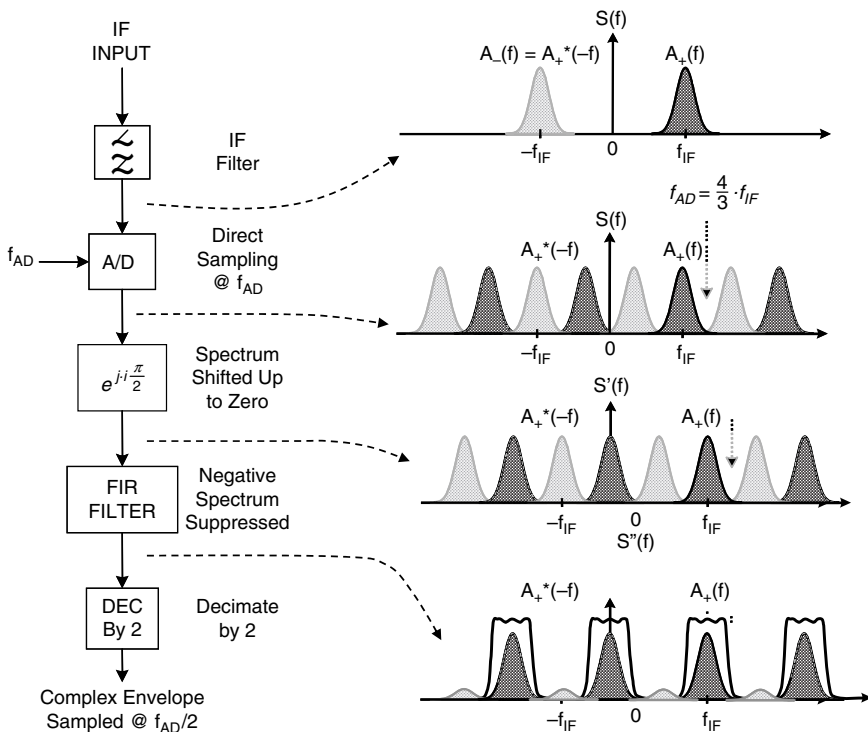


**FIGURE 2.83** Implementation of A/D conversion using direct sampling of the IF signal

an A/D converter sampling rate as given by Eq. 2.60, but other values will result in an available Nyquist bandwidth less than  $f_{AD}/2$ . This is shown in Figure 2.84 where the normalized Nyquist bandwidth is shown as a function of the relative A/D converter sampling rate. From this figure, it is seen that the direct conversion approach will fail whenever a value of  $M$ , which is located halfway between the optimum values, is used.

At the A/D converter output, the signal samples are still real valued. To be able to extract the complex envelope corresponding to the positive part of the spectrum,  $2 \cdot A_{+}(f - f_{IF})$ , it is necessary to shift the spectrum at the A/D converter output down in frequency by the amount  $f_{IF}$ . This corresponds to a multiplication by the time series  $u(i) = e^{-j\cdot i \frac{2\pi}{f_{IF}}}$ . Equivalently, the complex envelope spectrum below zero frequency can be shifted up to zero frequency by multiplication with the time series  $u(i) = e^{j\cdot i \frac{\pi}{2}}$ . This results in the spectrum shown where the desired spectrum corresponding to the complex envelope is centered at zero frequency, but the signal still contains the unwanted negative spectral components (light shading). As a result of this frequency translation, the signal has now become complex. A digital FIR band-pass filter with a nearly rectangular response is then applied to reject the negative-frequency components as shown in the final graph on the right. The desired sampled complex envelope representation has now been realized, but at the original sampling rate of  $f_{AD}$ . If desired, the oversampling can finally be removed through decimation by a factor of 2 as shown in the last step in the figure.

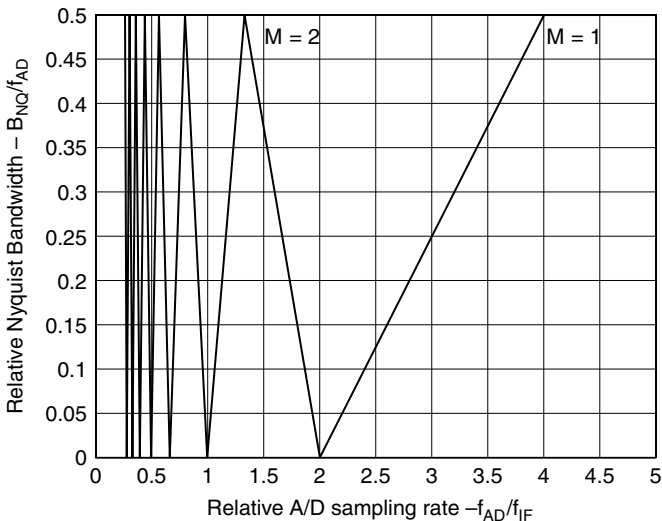


**FIGURE 2.84** Available Nyquist bandwidth vs. A/D converter sampling rate

A/D converters are typically characterized by their signal-to-noise ratio (SNR) performance referred to a bandwidth equal to the A/D sampling rate. Often this SNR is not as high as one would expect based on the number of bits used by the A/D converter. Sometimes the actual performance of an A/D converter is characterized by an effective number of bits, smaller than the actual number of bits and corresponding to the achievable SNR. The SNR of an A/D converter sets an upper limit on the achievable improvement factor.

## 2.14 ADAPTIVE MTI

---

When the doppler frequency of the returns from clutter is unknown at the radar input, special techniques are required to guarantee satisfactory clutter suppression. As discussed in Section 2.10, the doppler filter bank will usually be effective against moving clutter. This requires that the individual filters be designed with a low sidelobe level in the regions where clutter may appear and that each filter be followed by appropriate CFAR processing circuits to reject unwanted clutter residue. When clutter suppression is to be implemented with a single MTI filter, it is necessary to use adaptive techniques to ensure that the clutter falls in the MTI rejection notch. An example of such an adaptive MTI is TACCAR,<sup>31</sup> originally developed for airborne radars. In many applications, the adaptive MTI will further have to take into account the situation where multiple clutter sources with different radial velocities are present at the same range and bearing.

Usually the doppler shift of clutter returns is caused by the wind field, and early attempts of compensating in the MTI have varied the coho frequency sinusoidally as a function of azimuth based on the average wind speed and direction. This approach is

unsatisfactory because the wind field rarely is homogeneous over a large geographical area and because the wind velocity usually is a function of altitude due to wind shear (important for rain clutter and chaff). Against a single clutter source, an implementation is required that permits the MTI clutter notch to be shifted as a function of range. An example of such an adaptive MTI implementation is shown in Figure 2.85. The phase-error circuit compares the clutter return from one sweep to the next. Through a closed loop, which includes a smoothing time constant, the error signal controls a phase shifter at the cohō output such that the doppler shift from pulse to pulse is removed. It should be noted that since the first sweep entering the MTI is taken as a reference, any phase shift run-out as a function of range will increase proportionally to the number of sweeps. Ultimately this run-out will exceed the speed of response of the closed loop, and the MTI must be reset. This type of closed-loop adaptive MTI must, therefore, be operated for a finite set (batch) of pulses to ensure that this will not happen. Such batch-mode operation is also required if a combination of MTI operation and frequency agility is desired.

If a bimodal clutter situation is caused by the simultaneous presence of returns from land clutter and weather or chaff, an adaptive MTI can be implemented following a fixed-clutter-notch MTI section, as illustrated in Figure 2.86. The number of zeros used in the fixed- (zero doppler) clutter-notch section of the MTI is determined by the required improvement factor and the spectral spread of the land clutter. Typically, the fixed-notch MTI would use two or three zeros. For the adaptive portion of the MTI, a fully digital implementation is shown in which the pulse-to-pulse phase shift of the clutter output from the first canceler is measured and averaged over a given number of range cells. This estimated phase shift is added to the phase shift, which is applied to the data on the previous sweep, and this new phase shift is applied to the current data.

The range averaging must be performed separately on the I and Q components of the measured phase in each range cell due to the  $2\pi$  ambiguity of the phase representation itself. The accumulation of the applied phase shift from sweep to sweep, however, must be performed directly on the phase and is computed modulo  $2\pi$ . The number of zeros of the adaptive MTI section is again determined by the required improvement factor and the expected spectral spread of the clutter. The phase shift is applied to the input data in the form of a complex multiply, which again requires the transformation of the phase angle into rectangular coordinates. This transformation can easily be performed by a table lookup operation in a read-only memory.

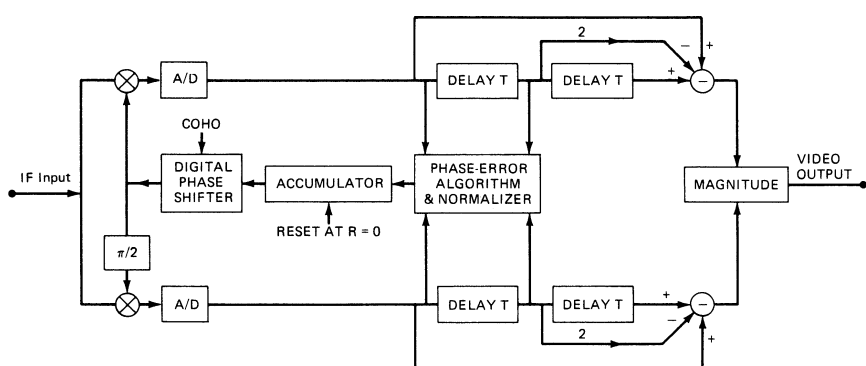


**FIGURE 2.85** Block diagram of closed-loop adaptive digital MTI

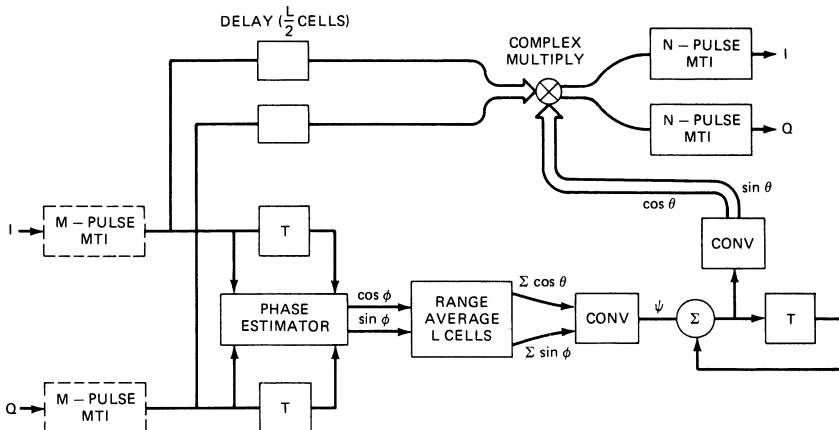


**FIGURE 2.86** Open-loop adaptive MTI for cancellation of simultaneous fixed and moving clutter

When doppler shifts are introduced by digital means as described above, the accuracy of the I and Q representation of the original input data becomes an important consideration. Any dc offset, amplitude imbalance, quadrature phase error, or nonlinearity will result in the generation of undesired sidebands that will appear as residue at the canceler output. A discussion of A/D conversion considerations was presented in Section 2.13.

In the adaptive MTI implementation described above, the number of zeros allocated to each of the two cancelers was fixed, based on an a priori assessment of the clutter suppression requirement. The only variation possible would be to completely bypass one (or both) of the MTI cancelers if no land clutter or weather or chaff returns are received on a given radial. A more capable system can be implemented if the number of zeros can be allocated dynamically to either clutter source as a function of range. This leads to a fully adaptive MTI implementation using a more complex adaptation algorithm, as discussed below. Such an adaptive MTI may provide a performance close to the optimum discussed in Section 2.7.

In order to illustrate the difference in performance between such candidate MTI implementations, a specific example is considered next. For this example, land clutter returns are present at zero doppler with a normalized spectral spread of  $\sigma_f T = 0.01$ , and chaff returns are present at a normalized doppler offset of  $f_d T = 0.25$  with a normalized spectral spread of  $\sigma_f T = 0.05$ . The power ratio of the land clutter to that of the chaff is denoted  $Q$  (dB). Thermal noise is not considered in this example. In both cases, the total number of filter zeros is assumed to be equal to 3. For the adaptive MTI with a fixed allocation of zeros, two zeros are located at zero doppler and the remaining zero is centered on the chaff returns. In the optimum MTI, the zero locations are chosen so that that overall improvement factor is maximized. The results of this comparison are presented in Figure 2.87, which shows the improvement factor for the optimum and the adaptive MTI as a function of the power ratio  $Q$  (dB). When  $Q$  is small so that chaff returns dominate, a significant performance improvement can be realized by using all MTI filter zeros to cancel the chaff returns. The performance difference for large values of  $Q$  is a result of an assumption made that the location of the third zero remains fixed at the chaff doppler frequency. In reality, the adaptive MTI would move

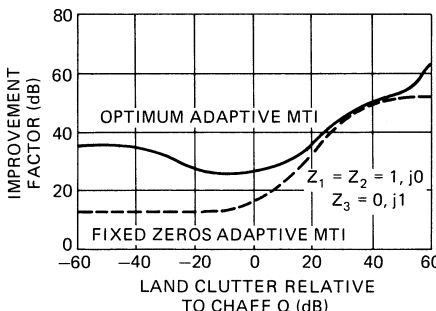


**FIGURE 2.87** Improvement factor comparison of optimum and adaptive MTI against fixed and moving clutter of ratio  $Q$

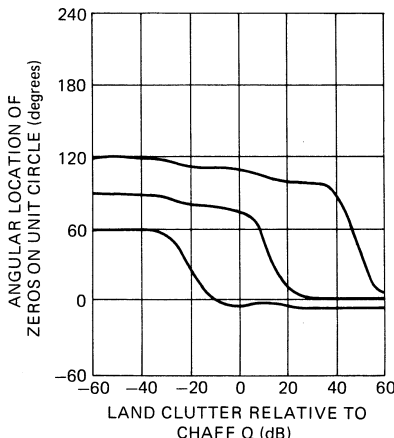


**FIGURE 2.88** Location of the three filter zeros for an optimum MTI used against fixed and moving clutter

its third zero to the land clutter as the land clutter residue starts to dominate the output of the first canceler. The zero locations of the optimum MTI are shown in Figure 2.88 and can be seen to move between the land clutter at zero doppler toward the doppler of the chaff returns as the relative level of the land clutter becomes small.

## 2.15 RADAR CLUTTER MAPS

In many MTI radar applications, the clutter-to-noise ratio in the receiver will exceed the improvement factor limit of the system even when techniques such as sensitivity time control (STC), improved radar resolution, and reduced antenna gain close to the horizon are used to reduce the level of clutter returns. The resulting clutter residues after the MTI canceler must, therefore, be further suppressed to prevent saturation of the PPI display and/or an excessive false-alarm rate in an automatic target detection (ATD) system.

Against spatially homogeneous sources of clutter such as rain, sea clutter, or corridor chaff, a cell-averaging constant-false-alarm-rate (CA-CFAR) processor following the MTI filter will usually provide good suppression of the clutter residues. Special features are sometimes added to the CA-CFAR, such as greatest-of-selection or two-parameter (scale and shape) normalization logic, in order to improve its effectiveness at clutter boundaries if the probability distribution of the clutter amplitude is non-gaussian. However, when the clutter returns are significantly nonhomogeneous, as is the case for typical land clutter returns, the performance of the cell-averaging CFAR will not be satisfactory and other means must be implemented to suppress the output residues to the noise level.

The traditional solution to this problem has been to deliberately reduce the receiver dynamic range prior to the MTI filter to the same value as the maximum system improvement factor. Theoretically, then, the output residue should be at or below the normal receiver noise level, and no false alarms would be generated. In practice, the introduction of IF limiting against the ground clutter returns will result in an additional

improvement factor restriction, as discussed in Section 2.11. Consequently, for the limited IF dynamic range to have the desired effect on the output residues, the limit level must be set 5 to 15 dB below the improvement factor limit of the linear system. The net result is that some of the clutter suppression capability of the MTI radar must be sacrificed in exchange for control of the output false-alarm rate.

Since returns from land clutter scatterers usually are spatially fixed and, therefore, appear at the same range and bearing from scan to scan, it has long been recognized that a suitable memory circuit could be used to store the clutter residues and remove them from the output residue on subsequent scans by either subtraction or gain normalization. This was the basic principle of the so-called area MTI, and many attempts have been made to implement an effective version of this circuit over an extended span of time. The main hindrance to its success has been the lack of appropriate memory technology, since the storage tube (long the only viable candidate) lacks in resolution, registration accuracy, simultaneous read-and-write capability, and stability. The development of high-capacity semiconductor memories is the technological breakthrough that has made the design of a working area MTI a reality. The *area MTI* is better known today as a *clutter map*, but both terms are used.

The clutter map may be considered as a type of CFAR where the reference samples, which are needed to estimate the level of the clutter (or clutter residue), are collected in the cell under test on a number of previous scans. Since aircraft targets usually move several resolution cells from one scan to the next, it is unlikely that the reference samples will be contaminated by a target return. Alternatively, by making the averaging time (in terms of past scans) long, the effect of an occasional target return can be minimized. Although the primary purpose of the clutter map is to prevent false alarms due to discrete clutter or clutter residues that are at a fixed location, it may also be necessary to consider slowly moving point clutter in the clutter map design, either to suppress bird returns or because the radar is on a moving platform (e.g., a ship).

The memory of a clutter map is usually organized in a uniform grid of range and azimuth cells, as illustrated in Figure 2.89. Each map cell will typically have 8 to 16 bits of memory so that it will handle the full dynamic range of signals at its input, which makes it possible to detect a strong target flying over a point of clutter (sometimes referred to as *superclutter visibility*). The dimensions of each cell are a compromise between the required memory and several performance characteristics. These are the minimum target velocity that will not be suppressed by the map (so-called cutoff velocity), its transient response, and the loss in sensitivity caused by the clutter map (similar to a CFAR loss). The minimum cell size will be constrained by the size of the radar resolution cell.

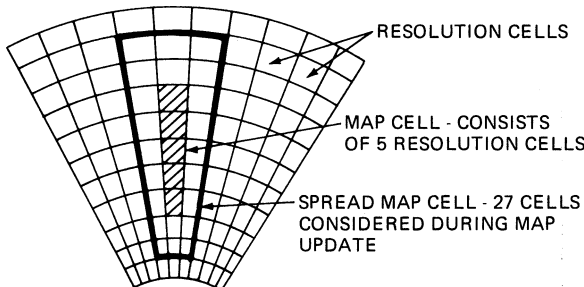


**FIGURE 2.89** Clutter map cell definition

Each map cell is updated by the radar returns (or residues) falling within its borders (or in its vicinity) on several previous scans. To save memory, the cells are usually updated by using a simple recursive (single-pole) filter of the form

$$y(i) = (1 - \alpha) \cdot y(i-1) + \alpha \cdot x(i) \quad (2.61)$$

where  $y(i-1)$  is the clutter map amplitude from the previous scan,  $y(i)$  is the updated clutter map amplitude,  $x(i)$  is the radar output on the present scan, and the constant  $\alpha$  determines the memory of the recursive filter. The test for detecting a target based on the output  $x(i)$  is

$$x(i) \geq k_T \cdot y(i-1) \quad (2.62)$$

where the threshold constant  $k_T$  is selected to give the required false-alarm rate. Alternatively, the radar output can be normalized on the basis of the clutter map content to obtain an output  $z(i) = \frac{x(i)}{y(i-1)}$ , which can be processed further if required. Analogously to the implementation of the cell-averaging CFAR processor, the amplitude  $x(i)$  can be obtained using a linear, square-law, or logarithmic detector.

The loss in detectability due to the clutter map is analogous to the CFAR loss analyzed in the literature for many different conditions. An analysis of the clutter map loss for single-hit detection using a square-law detector has been presented by Nitzberg.<sup>44</sup> These and other results can be summarized into a single universal curve of clutter map loss,  $L_{CM}$ , as a function of the clutter map ratio  $x/L_{eff}$ , as shown in Figure 2.90, where  $x$  defines the required false-alarm probability according to  $P_f = 10^{-x}$  and  $L_{eff}$  is the effective number of past observations averaged in the clutter map defined as

$$L_{eff} = \frac{2 - \alpha}{\alpha} \quad (2.63)$$

For example, for  $P_f = 10^{-5}$  and  $\alpha = 0.125$ , the clutter map loss is  $L_{CM} = 1.8$  dB since  $x = 5$  and  $L_{eff} = 15$  for this case. Also shown in Figure 2.90 is the curve for the conventional CA-CFAR,<sup>45</sup> where all reference samples are equally weighted. If more than one noise and/or clutter amplitude is used to update the clutter map content on each scan, the value of  $L_{eff}$  should be increased proportionally. It should also be noted that most radars base their target detection on multiple hits using some form of video integration, and that a clutter map loss based on the single-hit results of Figure 2.90 could be much too large.

An analysis of the performance of typical implementations of clutter maps has been discussed in Khoury and Hoyle.<sup>46</sup> From this reference, a typical transient-response curve is shown in Figure 2.91 for a single point clutter source 20 dB above thermal noise that fluctuates from scan-to-scan according to a Rayleigh probability density function, a filtering constant of  $\alpha = 0.125$  and assuming four returns noncoherently integrated in each clutter map cell. The abscissa is in radar scans, and the ordinate is probability of detection of the point clutter source. Since the clutter point has the same amplitude statistics as thermal noise, the output false-alarm rate approaches  $P_f = 10^{-6}$  asymptotically.

Against a slowly moving source of clutter (e.g., birds), the probability of detection may increase as the clutter source crosses the boundary between two clutter map cells. To prevent this, a spreading technique can be used, through which each clutter map cell will be updated—not only with radar returns falling within its boundaries, but also

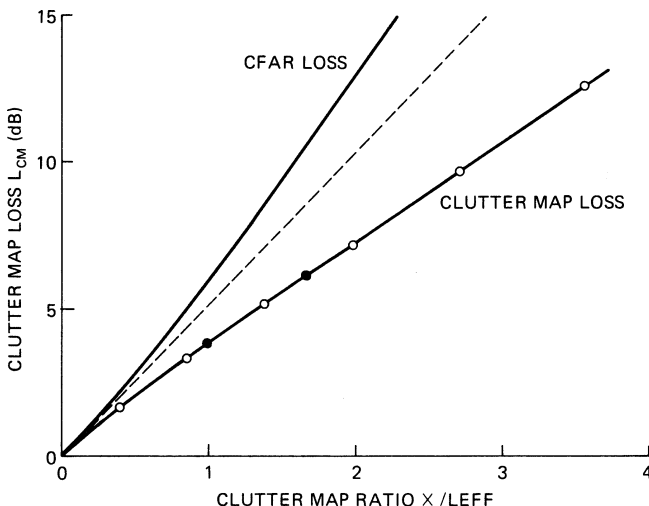


**FIGURE 2.90** Universal curve for determining detectability loss caused by the clutter map

by using radar returns in adjacent cells in range and azimuth. Through the use of such spreading, an additional degree of control over the clutter map velocity response can be achieved.

An example of the velocity response of a clutter map including such spreading is shown in Figure 2.92. The range extent of the clutter map cell is  $5 \mu\text{s}$ , the radar resolution cell is  $1 \mu\text{s}$ ,  $n = 4$  pulses are noncoherently integrated, the filtering constant is  $\alpha = 0.125$ , the update interval is  $5 \text{ s}$ , and the  $SNR = 20 \text{ dB}$ . On each scan, the clutter map cell is updated with the radar amplitudes in the five range cells falling within the clutter map cell and with the amplitude from one additional radar resolution cell before and after the clutter map cell.

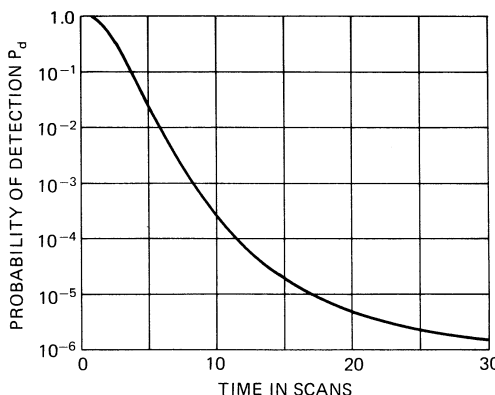


**FIGURE 2.91** Transient response of clutter map due to Swerling Case 2 point clutter model

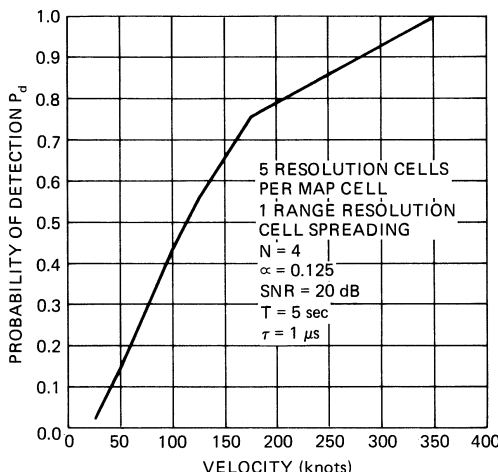


FIGURE 2.92 Velocity response of clutter map

It is seen from Figure 2.92 that the velocity response characteristic of the clutter map from stopband to passband is somewhat gradual in this particular implementation. This is partly due to the large size of the clutter map cell relative to the radar resolution. A finer-grain map with additional spreading would have a much better velocity response characteristic.

A potential problem with the type of amplitude clutter map described in this section is the fact that a large target flying in front of a smaller target may cause enough buildup in the map to suppress the small target. One way to overcome this problem in a system that includes automatic tracking would be to use the track prediction gate to inhibit updating of the clutter map with new (target) amplitudes.

## 2.16 SENSITIVITY-VELOCITY CONTROL (SVC)

---

In the mid-1980s, several radar researchers had realized that signal processing algorithms to estimate the unambiguous radial velocity of a target using multiple PRF dwells during the time of target were becoming practical. These radial velocity estimates could be used for improved false-alarm control against slow-moving targets such as birds.<sup>30,47</sup> When such radial velocity measurements are paired with corresponding cross section estimates a powerful discriminant for distinguishing between slow-moving birds and low cross-section missiles becomes possible using the so-called sensitivity velocity control (SVC) algorithm.<sup>48</sup>

**The SVC Concept.** Sensitivity velocity control (SVC) is used when a radar must detect aircraft and missile targets in the presence of returns from unwanted targets such as large birds or bird flocks. The criteria to accept or reject targets is based on a combination of the radial velocity and apparent RCS (radar cross section) of the target returns. The desired targets may have an RCS smaller than a single bird, or possibly

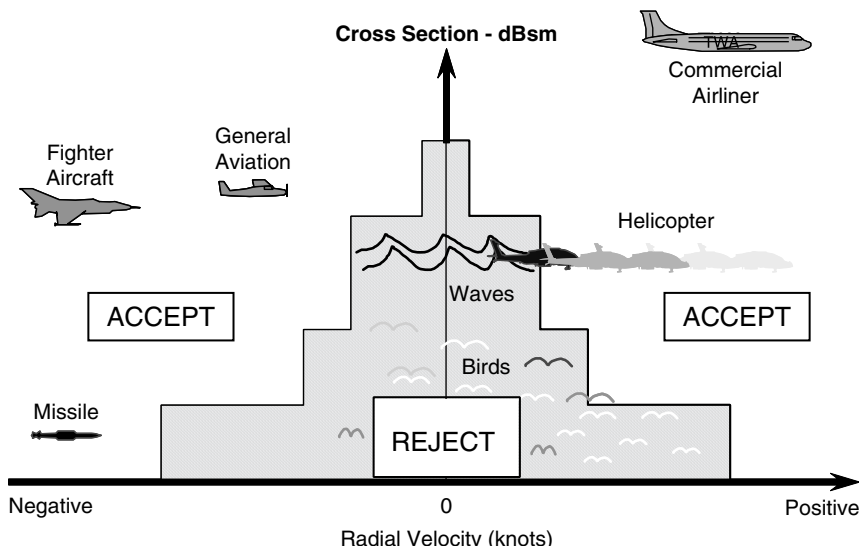


**FIGURE 2.93** Illustrative acceptance/rejection criteria of SVC

a bird flock (in a single radar resolution cell). Thus, discrimination requires a parameter in addition to the target RCS. The available parameter is target radial velocity. Birds typically fly at 40 knots or less, whereas targets of concern usually have airspeeds of 100 knots or more. If the radar can make unambiguous radar doppler measurements of, e.g.,  $\pm 160$  knots with a single CPI (coherent processing interval), the radar can determine the true radial velocity of each radar echo from returns of three or more consecutive CPIs at different PRFs.

The acceptance criteria of the SVC algorithm<sup>48</sup> relates to the type of target (aircraft, missile, bird, etc.) being accepted or rejected. In general, the criteria accepts large targets having low to high radial velocities. The smaller the apparent radar cross section of the target, the higher the true radial velocity must be for acceptance. The true radial velocity versus apparent radar cross section profile is intended to accept aircraft and missiles but reject birds. Therefore, threatening targets that have high radial velocities, but very small RCS, can be instantly identified, whereas returns from birds, with their slow radial velocities, can be censored. A typical SCV accept/reject algorithm is depicted in Figure 2.93.

To obtain the doppler space of  $\pm 160$  knots, ambiguous range PRFs must be used. This requires approximate PRFs of 1400 Hz at L band, 3,300 Hz at S band, and 11,000 Hz at X band (unambiguous ranges, respectively, 58 nmi, 27 nmi, and 5 nmi). The tradeoff for selecting PRFs is that in a dense target environment, when trying to resolve true radial velocity using different PRFs, “ghosts”<sup>§</sup> may be created.

<sup>§</sup> “Ghosts” occur when targets (or noise peaks) at different unambiguous ranges fold into the same, but incorrect, true range cell. The velocity resolution algorithm then gives an incorrect result, and the ghosts may be declared as threatening targets.

In addition to the “ghost” problem, multiple range ambiguities lead to targets having to compete with clutter at all ranges. In particular, targets at long distances have to compete with strong clutter returns in the first, or several, range intervals.

Because of the ghosting problem, in order to minimize range ambiguities while retaining adequate doppler space, RF frequencies of 1400 MHz or lower are best suited for the SVC unwanted target discrimination technique.

**Range- and Range Rate Ambiguity Resolution.** To apply the SVC algorithm, true range and radial velocity (range-rate) must be determined from the range-ambiguous and doppler-ambiguous waveform. This requires multiple detections from the same target. Assume a doppler filter bank of  $n$ -pulse FIR filters and assume a processing dwell that consists of three CPIs. The CPIs must use different PRFs and may also employ different RF frequencies. (The different RF frequencies change target RCS statistics from Swerling 1 to Swerling 2, and thus less radar energy is required for high probability of detection.) The CPIs must have (1) sufficient transmitted pulses so that  $n$  returns (enough to fill an  $n$ -pulse filter) will be received from the most distant target of interest and the most distant clutter and (2) one additional pulse to enable velocity determination (more on this later).

*True Range Determination.* The most straightforward way to detect a target and simultaneously determine its true range is to determine, on each CPI, all “primitive” detections at the output of the doppler filter bank. For this, it is assumed that each doppler filter output is processed through an appropriate clutter map threshold and cell-averaging CFAR to control the false-alarm rate. For each peak detection, adjacent amplitudes will be used to obtain an accurate ambiguous range estimate denoted  $\hat{r}_i$ , where the subscript refers to the CPI number. Also, from the specific doppler filter corresponding to the peak detection described above, the phase ( $\theta_{1i}$ ) of the return is saved. In addition, a corresponding phase ( $\theta_{2i}$ ) obtained from an identical second doppler filter bank trailing (or leading) the detection filter bank by one pulse repetition interval (PRI) is saved. This explains why a CPI of  $n + 1$  pulses is needed to implement the SVC concept. For each primitive detection in a CPI, calculate the set of all possible target ranges out to the maximum instrumented range  $R_{\max}$ :

$$\hat{R}_i = \hat{r}_i + m \cdot R_{\text{PRI},i} \quad m = 0, 1, 2, \dots, m_{\max} \quad (2.64)$$

where  $m_{\max} = \text{int}(R_{\max} / R_{\text{PRI},i}) + 1 \quad i = 1, 2, 3$

where  $R_{\text{PRI},i}$  is the ambiguous range interval corresponding to the  $i$ th CPI. After the primitive detections from all CPIs in the processing dwell have been processed, the values of  $\hat{R}_i$  from all CPIs are sorted into a single list. A final range detection and its true range is then found as a cluster of three primitive detections having possible ranges within an error window of two to three times the standard deviation of the ambiguous range estimate.

*True Radial Velocity Determination.* For each true target detection, an unambiguous radial velocity estimate must next be determined using a similar procedure to that described above for range. For this, an accurate estimate,  $f_{d,i}$ , of the ambiguous target radial velocity must be obtained at the range corresponding to the ambiguous primitive target detection on each CPI. This frequency estimation problem has been studied by many authors with the best approach being defined

by the maximum likelihood estimate.<sup>49</sup> For a single-pulse signal-to-noise ratio  $S_1$  and  $n$  pulses in a CPI, the Cramer-Rao lower bound for the accuracy of the doppler frequency estimate is

$$\frac{\sigma_f}{\text{PRF}} = \frac{\sqrt{6}}{2 \cdot \pi \cdot \sqrt{S_1 \cdot n \cdot (n^2 - 1)}} = \frac{0.3898}{\sqrt{S_1 \cdot n \cdot (n^2 - 1)}} \quad (2.65)$$

Since the maximum likelihood estimation procedure tends to require a tedious computational burden, a simplified approach for estimating the doppler frequency is highly desirable. One such approach using phase measurements of the doppler filter output at times separated by one interpulse period\* was presented in McMahon and Barrett.<sup>50</sup> The normalized doppler frequency estimate is

$$\frac{f_{d,i}}{\text{PRF}} = \frac{\theta_{1,i} - \theta_{2,i}}{2 \cdot \pi} \quad (2.66)$$

and the corresponding radial velocity is

$$\hat{v}_i = \frac{f_{d,i} \cdot \lambda}{2} \quad (2.67)$$

In most cases of interest, the accuracy of this estimate of doppler frequency is as good as the maximum likelihood procedure. Expressed in terms of the numerator of Eq. 2.65, which will be denoted by  $k$ , a simulation of the phase-difference estimator using different weighting functions for the doppler filter bank are summarized in Figure 2.94. It is noted that the performance of the phase-difference estimation procedure is best when moderate Taylor weighting functions are used. For uniform weighting, the procedure would be substantially inferior to the maximum likelihood approach. The increase in the constant  $k$  for the more severe weighting cases is the result of the SNR loss resulting from the use of weighting.

Using an approach similar to that used to resolve the range ambiguity, all possible radial velocities are then enumerated to the maximum negative and positive radial velocity of interest on each of the CPIs:

$$\hat{V}_i = \hat{v}_i + m \cdot V_{B,i} \quad m = -m_{\max}, -(m_{\max} - 1), \dots, 0, 1, 2, \dots, m_{\max} \quad (2.68)$$

where  $m_{\max} = \text{int}(V_{\max} / V_{B,i}) + 1 \quad i = 1, 2, 3$

In this equation,  $V_{B,i} = \text{PRF}_i \cdot \lambda / 2$  is the blind velocity for the  $i$ th CPI. The possible target radial velocities for all CPIs are then sorted into a single list, and the most likely true radial velocity is found where at least two possible velocities fall within an interval less than two or three times the standard deviation of the doppler frequency estimate. The tightness of the cluster of nearly identical velocities in conjunction with the number of CPIs contributing to the cluster can be utilized as a measure of reliability of the unambiguous radial velocity estimate.

---

\* This approach was first brought to the attention of the authors by Dr. Ben Cantrell of the U.S. Naval Research Laboratory.

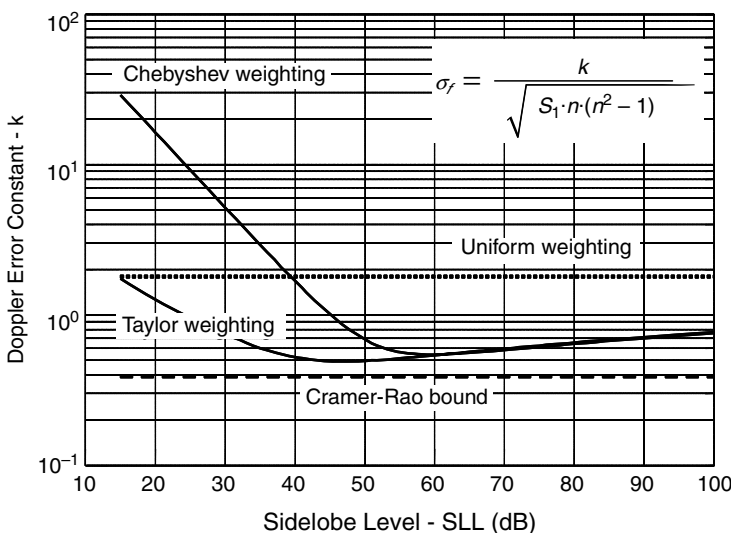


**FIGURE 2.94** Performance of phase-difference doppler frequency estimator for different weighting functions of the doppler filter bank

*Comments.* The above procedure for determining true range and true radial velocity has been described for a dwell of three CPIs and the assumption that each target will have a return for each of the three CPIs. In practice, this assumption is not always valid, and the actual implementation may choose, for example, to have the dwell consist of four or five CPIs, with the range and velocity determinations being based on the best grouping of three returns. The actual implementation must be based on the parameters of the system and permissible time allocated for each dwell.

The PRFs of the CPIs should be selected to minimize the chance of false radial velocity determinations. One method of selecting PRFs is similar to selecting pulse interval ratios for staggered PRF operation, as described in Section 2.8. For example, if operating at an average RF frequency of 1300 MHz, at an average PRF of 1400 Hz (ambiguous velocity of 312 knots), and covering a velocity range of interest of  $\pm 2500$  knots, there are approximately 16 doppler ambiguities to cover. Using the factors of  $-3, 2, -1, 3$ , as used in PRF stagger selection, the interpulse periods of the four different PRFs would be in the ratio of 13, 18, 15, 19. The average of these ratios is 16.25. The PRFs are calculated as  $16.25 \cdot 1400/13$ ,  $16.25 \cdot 1400/18$ ,  $16.25 \cdot 1400/15$ , and  $16.25 \cdot 1400/19$ . The PRFs would be about 1750, 1264, 1517, and 1197 Hz.

## 2.17 CONSIDERATIONS APPLICABLE TO MTI RADAR SYSTEMS

MTI radar system design encompasses much more than signal processor design. The entire radar system—transmitter, antenna, and operational parameters—must be keyed to function as part of an MTI radar. For example, excellent MTI concepts will not perform satisfactorily unless the radar local oscillator is extremely stable and the

transmitter has very little pulse-to-pulse frequency or phase jitter. In addition, the system must successfully operate in an environment that comprises many unwanted targets, such as birds, insects, and automobiles.

**Hardware Considerations.** In this section, rules and facts relating to MTI radar design, as developed during many years of work in the field, will be summarized:

The rules are as follows:

1. Operate at constant duty cycle.
2. Synchronize ac-dc and dc-dc power conditioners<sup>†</sup> to harmonics of the PRF.
3. Design the system to be fully coherent.<sup>‡</sup>
4. Provide IF Limiters prior to A/D converters.
5. Be wary of vibration and acoustic noise.

The facts are as follows:

1. The basic MTI concept does not require a long time on target to resolve targets from fixed clutter. Instead, MTI systems reject fixed clutter through a subtraction process while retaining moving targets.
2. Transmitter intrapulse anomalies have no affect on MTI performance if they repeat precisely pulse-to-pulse.

*Rule 1.* Operate at constant duty cycle. The transmitter (whether the transmitter is a single large tube or a distributed function as in an active phased array with many transmit-receive elements) should be operated at constant duty cycle. This permits the transmitter power supply transient effects to be identical pulse to pulse and also, particularly applicable to solid-state transmit devices, permits the device heating and cooling to be identical from pulse to pulse. Sometimes constant duty cycle operation is not possible, but there are various techniques that can be used to approach this desired condition. Consider an MTD waveform where a CPI consisting of  $n$  pulses is transmitted with a constant PRI. The next CPI uses a different PRI. Constant duty cycle can be maintained by changing the transmitted pulse length in proportion to the change in the PRI. If pulse compression is used, the range resolution of the compressed pulse can be maintained by changing the pulse compression waveform. If it is necessary to utilize precisely the same waveform and RF pulse length from CPI to CPI, with, for example, a klystron transmitter, the beam pulse of the klystron can be varied to maintain constant beam duty cycle while the RF pulse length is maintained constant. This wastes part of the beam pulse energy for the longer PRIs, but the average power loading on the power supply remains constant. The same technique can be utilized with solid-state devices by changing the drain voltage pulse duration, while holding the RF pulse constant. A second-order correction that has been utilized when changing between CPIs with different PRIs is to have a transition PRI that is the average of the two PRIs. With phased array radars, if the beam transition time between CPIs takes longer than a PRI, it is important to keep the transmitter pulsing at a constant duty cycle during the transition time. If constant duty cycle cannot be maintained, or when starting to radiate

---

<sup>†</sup> Power conditioners accept either ac or dc input and provide a regulated dc output.

<sup>‡</sup> “Fully coherent” is described under rule 3.

after dead time, the transmitter, power supply, and heating effects must be allowed to settle before good MTI performance can be expected. The duration of the settling time depends on the system parameters and the requirements.

*Rule 2.* Synchronize ac-dc and dc-dc power conditioners to harmonics of the PRF. When ac-dc and/or dc-dc power conditioners are used for voltages applied to transmitting devices, the frequency (and its harmonics) of the converter must be attenuated sufficiently so that they do not modulate the phase of the transmitted pulses. If the power conditioner frequencies cannot be sufficiently attenuated, their frequency should be synchronized to a multiple of the PRF of the CPI so that modulations repeat precisely pulse-to-pulse and thus will cancel like stationary clutter.

*Rule 3.* Design the system to be fully coherent. All frequencies and timing signals should be generated from a single master oscillator. Doing this makes the entire system coherent, and mixer products will be identical pulse-to-pulse and will, therefore, cancel in the MTI filters. When this coherence of all frequencies is not maintained, clutter residue will occur and must be quantified to determine if it is at an acceptable level. One of the prominent places in which residue caused by unsynchronized local oscillators has shown up is in pulse-compression sidelobes. If the pulse-compression sidelobes from fixed clutter returns vary from pulse to pulse, they do not cancel. This coherency issue has been further discussed by Taylor.<sup>51</sup>

*Rule 4.* Provide IF Limiters prior to A/D converters. MTI radars require that IF bandpass limiters exist prior to an A/D (analog/digital converter). The limiter prevents any clutter return from exceeding the dynamic range of the A/D. This requirement exists for either quadrature I, Q (in-phase, quadrature) sampling or direct sampling with the I and Q data constructed after the A/D. The limiter must be designed to minimize the conversion of amplitude to phase no matter how much the signal level exceeds the limit level. If clutter saturates the A/D, the I, Q data is significantly corrupted. When limiters prevent A/D saturation, the signals are limited in a controlled manner that still enables good clutter rejection about 90% of the time.

*Rule 5.* Be wary of vibration and acoustic noise. Many RF devices are susceptible to both vibration and acoustic noise. An air conditioner fan blowing on waveguide has caused degradation of improvement factor due to phase modulation of signals. Vibrations can cause phase modulation of an oscillator. Acoustic noise can originate from cooling fans, and vibrations can come from shipboard or airborne radar platforms. Components such as klystrons and solid-state modules can have unexpected susceptibility to vibration. RF connectors must be secure. Shock mounts can be used to isolate components from the cabinet structure. It is recommended that all RF components, in their operational configuration, be tested for phase stability in the vibration environment in which they will be used.

*Fact 1.* The basic MTI concept does not require sufficient time-on-target to resolve targets from fixed clutter using a linear time-invariant filter. Instead, MTI systems reject fixed clutter through a subtraction process while retaining moving targets. An MTI system using a two-pulse canceler requires the transmitter to transmit only two successive, identical pulses for the system to be able to reject stable fixed clutter. The radar returns from the second pulse are subtracted from the returns from the first pulse.

The result from this subtraction process is that the fixed clutter is removed, and moving targets are retained. The output from the first pulse is not used, making this type of MTI filter time-variant. Of course, the clutter filters may be more complex than a two-pulse canceler,<sup>§</sup> but the principle still remains that fixed clutter is rejected by the zeros in the canceler transfer characteristic. This enables phased array radars to have good clutter rejection with short dwells.\*

*Fact 2.* Transmitter intrapulse anomalies have no affect on MTI performance if they repeat precisely pulse to pulse. Transmitted pulses should be identical. It does not matter if there is intrapulse amplitude or frequency modulation of the transmitted pulse, as long as it repeats precisely from pulse to pulse. If the voltage of the transmitter power supply varies pulse to pulse, the transmitted pulses will not be identical, and the resulting variations must be quantified to determine if the limitations on improvement factor fall within the stability budget for the system. However, if the only difference between pulses is absolute phase (not intrapulse variations pulse to pulse), some mitigation is possible. One method of compensating for small variations in the phase of transmitter pulses follows. Lincoln Laboratory changed the original TDWR waveform to an MTD type waveform. (The original TDWR waveform was constant PRF during each antenna rotation, and processing was done with elliptic filters.) They then modified the system "...to achieve 65-dB clutter suppression using a nearby water tower for a target."<sup>52</sup> The TDWR uses a klystron transmitter tube. Typical phase pushing for a klystron due to modulator voltage change is 10° for 1% delta-E/E. The stability budget allocated a 75-dB limit on improvement factor to the transmitter, and this required that the rms pulse-to-pulse power supply voltage variation be less than 1 part in 100,000. The transmitter power supply could not meet this requirement when the radar changed PRF from CPI to CPI, as required by an MTD waveform. Therefore, the actual phase of each transmitted pulse was measured, and this measured value was used to correct the phase of the received signals for that PRI. This technique causes small perturbations in phase from weather signals received from ambiguous ranges, but does not interfere with velocity estimates. (It does degrade the improvement factor of clutter signals received from ambiguous ranges, but for the TDWR operation, that degradation was deemed acceptable.)

**Environmental Considerations.** This discussion contains essential information for those designing a modern surveillance radar to detect man-made airborne targets. The laws of physics combined with the environment make it impossible to design an MTI surveillance radar that does not have compromises. The problems are related to the unwanted returns from birds, insects, automobiles, long-range fixed clutter, and short- and long-range weather.<sup>53</sup> The current state-of-the-art of radar can ameliorate these problems, but not without some undesirable side effects. (Many unwanted point target returns have characteristics similar to the returns from wanted targets, and the unwanted returns may outnumber returns from desired targets by the thousands.)

---

<sup>§</sup> The clutter filters must be designed based on system parameters to reject the radial speed of the "fixed" clutter. See Sections 2.4 and 2.6.

\* It has been observed that some phased array radars have poor clutter rejection, which is often caused by failure to follow rule 1.

The problems are exacerbated when anomalous or ducted propagation occurs (*anomalous propagation*, as used herein, is when the radar energy follows the curvature of the Earth, thus causing detection of both fixed and moving clutter at long ranges). Figure 2.95 from Shrader<sup>53</sup> shows PPI photographs taken with an ARSR-2 radar mounted on a 50-ft tower in flat country near Atlantic City, New Jersey. With normal propagation, the expected line-of-sight is about 10 nmi, but the clutter actually goes out to 100 nmi. The bridges across the intracoastal waterway can be seen. On occasion, the unwanted long-range clutter and weather returns come from ambiguous ranges.

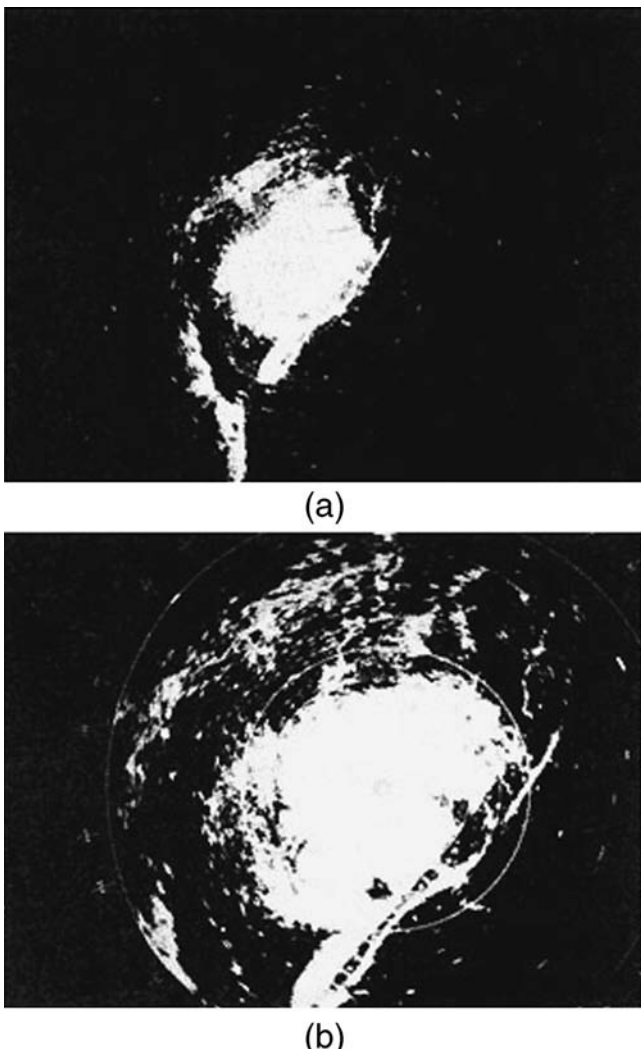


**FIGURE 2.95** Anomalous propagation (ducting): (a) 100-nmi maximum range and (b) 50-nmi maximum range

The radar system must have features to cope with these situations. For example, if pulse-to-pulse staggering is used, the ambiguous-range clutter will not cancel and either the PRI must be increased or the PRI must be made constant over the azimuth angles from which the ambiguous range clutter is received. And be forewarned of a pitfall into which many radar designers have fallen. For example, when presented with the requirement to track 20 targets, the designer may not realize that radar returns from the 20 targets of interest may be embedded in similar returns from thousands of unwanted targets.

A typical long-range air-traffic-control radar has sufficient sensitivity to detect a single large bird, such as a crow, seagull, or vulture (approximate RCS of 0.01 square meter) at a range of 50 miles. If there are many such birds in the resolution cell of the radar, then the composite RCS increases. Ten large birds in a resolution cell will have an RCS of 0.1 square meter. When multipath reflections occur, such as over the ocean when the radar beam is centered at the horizon, there can be up to a 12 dB enhancement of the RCS of the birds, giving an apparent RCS greater than one square meter to the flock of 10 birds. If there is 1 bird (or bird flock) per square mile, there will be about 3000 bird returns within 30 miles of the radar.

Techniques used to counter unwanted targets are as follows:

1. Sensitivity time control (STC) used for eliminating low RCS targets in low PRF radars—that is, radars that have no range ambiguities under normal operation
2. Enhanced high-angle gain antennas
3. Two-beam antennas—beam lifted above the horizon for short-range reception, and then lowered to horizon for long range
4. MTD techniques using clutter maps. Also counting detections in small range-azimuth sectors and increasing detection thresholds in each sector if too many detections occur.
5. PRFs high enough so that all targets with radial velocities below 40 knots can be censored
6. Sensitivity velocity control (SVC), which censors radially slow, small targets, while accepting radially fast targets and large targets

Combinations of techniques 1 through 4 are used in most air-traffic-control radars where the smallest targets of interest have an RCS of one-square meter or greater. Techniques 5 and 6 are used when the desired targets may have radar cross sections similar to, or smaller than, a bird.

*Technique 1.* STC is the traditional method of suppressing birds and insects in a radar with an unambiguous range PRF (a PRF low enough so that the range to targets and clutter is unambiguous). STC decreases the sensitivity of the radar at short range and then increases sensitivity, usually using a fourth-power law, as range increases. This has the effect of not permitting detection of targets with apparent radar cross sections of, say, less than 0.1 square meter. Figure 2.96 shows how effective STC can be against birds. These PPI photos were taken with an L band ARSR (air-route surveillance radar) in Oklahoma. Note that the majority of returns from birds were eliminated, but not 100%. Figure 2.97 shows the effect of STC against bats and insects.<sup>†</sup>

---

<sup>†</sup> Daytime bird returns and nighttime bat and insect returns can often be seen in real time—the extent depends on the weather and time of year—on the NEXRAD (WSR-88D) weather radar images on the NOAA Internet sites.

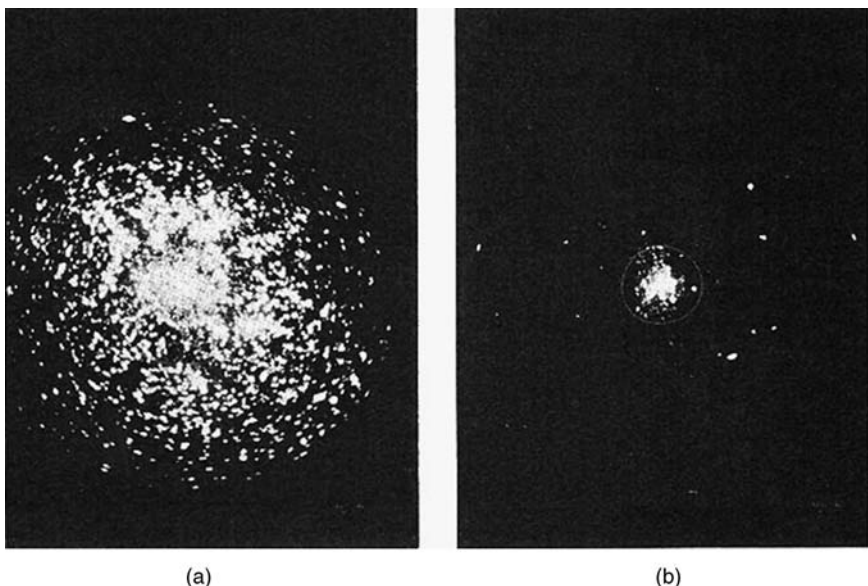


**FIGURE 2.96** STC can greatly reduce the number of birds displayed. Range 25 nmi. (a) Birds seen with MTI and (b) birds seen with MTI and STC.

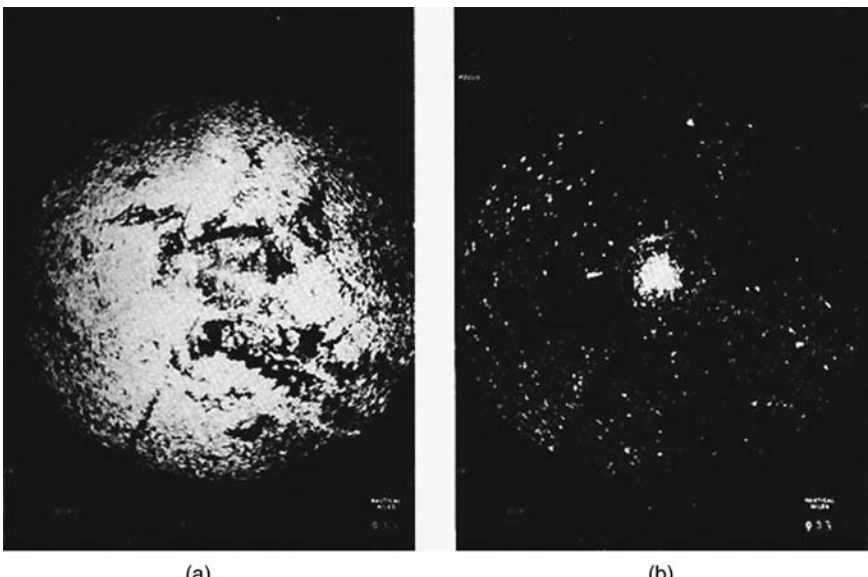


**FIGURE 2.97** Insects with and without STC and range 25 miles: (a) bats and insects seen with MTI and (b) bats and insects seen with MTI and STC

The typical doppler radar images presented by TV weather forecasters often have the birds and bats and insects removed by human intervention.

*Technique 2.* STC works quite well for unwanted biological returns near the peak of the radar beam, but when used with a cosecant-squared antenna beam it solves one problem but creates another: it also decreases sensitivity to desired targets at high elevation angles where the antenna gain is low. The solution to this problem is to boost the antenna gain at high elevation angles to be considerably higher than the requirement for the cosecant-squared pattern. Not only does this compensate for the use of STC, but also enhances the target-to-clutter signal ratio for targets at high elevation angles, thus improving MTI performance. The penalty for this solution is a loss in the peak antenna gain that can be achieved. An illustration of this approach is provided in Figure 2.98, which shows both the ARSR-2 antenna pattern and the corresponding free-space coverage.

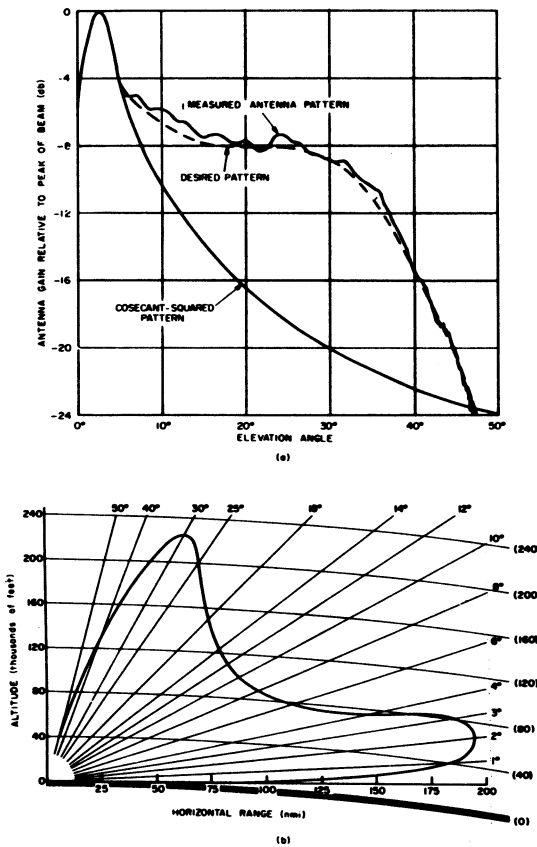


**FIGURE 2.98** Antenna elevation pattern for the ARSR-2 antenna:  
(a) compared with the cosecant-squared pattern and (b) free-space coverage diagram

The loss in peak gain for this example, due to the boost of coverage at high angles, was about 2 dB. The combination of STC with enhanced high-angle coverage does quite well for insects and birds, but does not eliminate automobile and truck returns. Vehicles have RCSs that equal or exceed the RCS of many desired aircraft targets.

*Technique 3.* The two-beam technique reduces the returns from very low elevation angles where vehicle traffic (and many birds, bats, and insects) is encountered. The radar transmits energy using the basic pattern, but uses a higher angle beam for reception at shorter ranges, and the basic antenna pattern for receiving at longer ranges. Figure 2.99 shows, underneath the transmitting feed horn, a second receive-only antenna feed horn for the high beam. The effective two-way antenna patterns are shown in Figure 2.100.

As previously mentioned, the above techniques (STC, two-beam antennas, and some variation of MTD) are currently used on many air-traffic-control radars. The two-beam antennas also utilize some high-angle gain enhancement to counter the high-angle effects of STC.

*Technique 4.* The MTD approach is described in Section 2.2.

*Technique 5.* A brute-force technique used to eliminate targets with radial velocities of less than approximately  $\pm 40$  knots resulting in a total rejection interval of 80 knots. To keep this rejection of velocities to no more than 25% of the doppler space available, the ambiguous velocity must be about 320 knots. This requires PRFs of 1,400 Hz at L band, 3,300 Hz at S band, and 11,000 at X band (unambiguous ranges, respectively, 58 nmi, 27 nmi, and 5 nmi). The main challenge with this technique is that fixed clutter returns from many range ambiguities, as well as all targets of interest, fold into the first range interval. Thus, excellent clutter rejection must be provided to prevent folded clutter from suppressing targets of interest, which may be at any true range.

*Technique 6.* SVC, as described in Section 2.16, is used when it is necessary to distinguish very low RCS targets from low velocity clutter, such as birds, insects, and sea. Somewhat lower PRFs can be used than those used for technique 5 because the

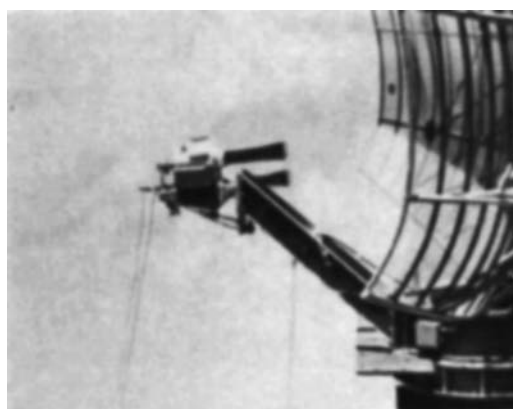


**FIGURE 2.99** Two-beam antenna

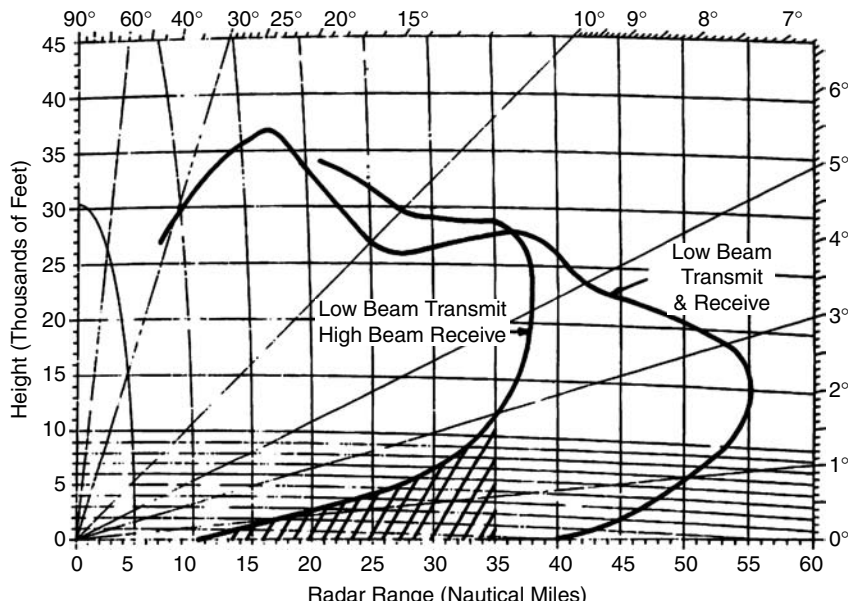


**FIGURE 2.100** Example of coverage obtained with a two-beam antenna

logic permits retaining many of the targets with smaller radial velocities if their RCS is large enough. SVC still rejects bird clutter, but retains, for example, the fast incoming, threatening low-RCS missile, while also retaining the larger cross-section aircraft with lower radial velocities.

## REFERENCES

---

1. S. Applebaum, "Mathematical description of VICI," General Electric Co., Syracuse, NY, Report No. AWCS-EEM-1, April 1961.
2. S. M. Chow, "Range and doppler resolution of a frequency-scanned filter," *Proc. IEE*, vol. 114, no. 3, pp. 321–326, March 1967.
3. C. E. Muehe, "New techniques applied to air-traffic control radars," *Proc. IEEE*, vol. 62, pp. 716–723, June 1974.
4. R. J. Purdy et al., "Radar signal processing," *Lincoln Laboratory Journal*, vol. 12, No. 2, 2000.
5. R. J. McAulay, "A theory for optimum MTI digital signal processing," MIT Lincoln Laboratory, Lexington, MA, Report no. 1972-14 Part I, Part II, Supplement I, February 22, 1972.
6. E. J. Barlow, "Doppler radar," *Proc. IRE*, vol. 37, pp. 340–355, April 1949.
7. W. L. Simkins, V. C. Vannicola, and J. P. Royan, "Seek Igloo radar clutter study," Rome Air Development Center, Report No. Rept. TR-77-338 (DDC AD-A047 897), October 1977.
8. W. Fishbein, S. W. Graveline, and O. E. Rittenbach, "Clutter attenuation analysis," US Army Electronics Command, Fort Monmouth, NJ, Report No. ECOM-2808, March 1967.
9. J. B. Billingsley, *Low-Angle Radar Land Clutter—Measurements and Empirical Models*, Norwich, NY: William Andrew Publishing, 2002.

10. F. E. Nathanson and J. P. Reilly, "Radar precipitation echoes—Experiments on temporal, spatial, and frequency correlation," The Johns Hopkins University, Applied Technology Laboratory, Report No. Tech. Memo TG-899, April 1967.
11. D. K. Barton, *Radar System Analysis*, Englewood Cliffs, NJ: Prentice-Hall, 1964.
12. D. K. Barton, "Radar equations for jamming and clutter," in *Supplement to IEEE Trans. AES-3, EASCON'67 Tech. Conv. Rev.*, November, 1967, pp. 340–355.
13. R. J. Doviak and D. S. Zrnic, *Doppler Radar and Weather Observations*, Orlando, FL: Academic Press, 1984.
14. H. R. Ward, "A model environment for search radar evaluation," in *EASCON '71 Convention Record*, New York, 1971, pp. 81–88.
15. IEEE, "IEEE Standard Radar Definitions," Radar Systems Panel, IEEE Aerospace and Electronics Systems Society, Report No. IEEE Std 686-1997, 1999.
16. D. K. Barton and W. W. Shrader, "Interclutter visibility in MTI systems," in *IEEE EASCON '69 Tech. Conv. Rec.*, New York, NY, October 1969, pp. 294–297.
17. D. K. Barton, *Modern Radar System Analysis*, Norwood, MA: Artech House, 2005, pp. 228–230.
18. L. Spafford, "Optimum radar signal processing in clutter," *IEEE Trans.*, vol. IT-14, pp. 734–743, September 1968.
19. L. A. Wainstein and Y. D. Zubakov, *Extraction of Signals From Noise*, New York: Dover, 1970.
20. J. Capon, "Optimum weighting functions for the detection of sampled signals in noise," *IRE Trans. Information Theory*, vol. IT-10, pp. 152–159, April 1964.
21. L. R. Rabiner et al., "Terminology in digital signal processing," *IEEE Trans. on Audio and Electroacoustics*, vol. AU-20, no. 5, pp. 322–337, December 1972.
22. M. I. Skolnik, *Introduction to Radar Systems*, 3rd Ed., New York: McGraw-Hill, 2001, p. 117.
23. H. Urkowitz, "Analysis and synthesis of delay line periodic filters," *IRE Trans. Circuit Theory*, vol. CT-4, no. 2, pp. 41–53, June 1957.
24. W. M. Hall and H. R. Ward, "Signal-to-noise ratio loss in moving target indicator," *Proc. IEEE*, vol. 56, pp. 233–234, February 1968.
25. W. W. Shrader and V. Gregers-Hansen, "Comments on 'Coefficients for feed-forward MTI radar filters,'" *Proc IEEE*, vol. 59, pp. 101–102, January 1971.
26. W. D. White and A. E. Ruvin, "Recent advances in the synthesis of comb filters," in *IRE Nat. Conv. Rec.* vol. 5, pt. 2, New York, NY, 1957, pp. 186–200.
27. R. H. Fletcher and D. W. Burlage, "Improved MTI performance for phased array in severe clutter environments," in *IEEE Conf. Publ. 105*, 1973, pp. 280–285.
28. A. V. Oppenheim and R. W. Schafer, *Digital Signal Processing*, Englewood Cliffs, NJ: Prentice-Hall, Inc., 1975, p. 223.
29. L. Zverev, "Digital MTI radar filters," *IEEE Trans.*, vol. AU-16, pp. 422–432, September 1968.
30. Ludloff and M. Minker, "Reliability of velocity measurement by MTD radar," *IEEE Trans.*, vol. AES-21, pp. 522–528, July 1985.
31. W. W. Shrader, "MTI Radar." Chap. 17 in *Radar Handbook*, M. I. Skolnik (ed.), New York: McGraw-Hill, 1970, pp. 17–19.
32. T. M. Hall and W. W. Shrader, "Statistics of clutter residue in MTI radars with IF limiting," in *IEEE Radar Conference*, Boston, MA, April 2007, pp. 01–06.
33. G. Grasso, "Improvement factor of a nonlinear MTI in point clutter," *IEEE Trans.*, vol. AES-4, November 1968.
34. H. R. Ward and W. W. Shrader, "MTI performance degradation caused by limiting," in *EASCON '68 Tech. Conv. Rec.*, (supplement to *IEEE Trans.* vol. AES-4), November 1968, pp. 168–174.
35. G. Grasso and P. F. Guarugnini, "Clutter residues of a coherent MTI radar receiver," *IEEE Trans.*, vol. AES-5, pp. 195–204, March 1969.
36. T. A. Weil, "Applying the Amplitron and Stabilotron to MTI radar systems," in *IRE Nat. Conv. Rec.*, vol. 6, pt. 5, New York, NY, 1958, pp. 120–130.

37. T. A. Weil, "An introduction to MTI system design," *Electronic Progress*, vol. 4, pp. 10–16, May 1960.
38. D. B. Leeson and G. F. Johnson, "Short-term stability for a doppler radar: Requirements, measurements, and techniques," *Proc. IEEE*, vol. 54, pp. 329–330, February 1966.
39. Hewlett Packard Product Note 11729B-1, March 1984.
40. R. Vigneri et al., "A graphical method for the determination of equivalent noise bandwidth," *Microwave Journal*, vol. 11, pp. 49–52, June 1968.
41. D. Steinberg, "Chaps.1–4 in *Modern Radar: Analysis, Evaluation, and System Design*, R. S. Berkowitz (ed.), New York, NY: John Wiley and Sons, 1966.
42. J. R. Klauder, "The theory and design of chirp radars," *Bell System Technical Journal*, vol. XXXIX, no. 4, pp. 745–809, July 1960.
43. W. Rice and K. H. Wu, "Quadrature sampling with high dynamic range," *IEEE Trans. Aerospace and Electronic Systems*, vol. AES-18, no. 4, pp. 736–739, November 1982.
44. R. Nitzberg, "Clutter map CFAR analysis," *IEEE Trans.*, vol. AES-22, pp. 419–422, July 1986.
45. V. Gregers Hansen, "Constant false alarm rate processing in search radars," in *Radar—Present and Future*, IEE Conf. Publ. no. 105, London, UK, October 1973.
46. N. Khoury and J. S. Hoyle, "Clutter maps: Design and performance," in *IEEE Nat. Radar Conf.*, Atlanta, GA, 1984.
47. G. V. Trunk et al., "False alarm control using doppler estimation," *IEEE Trans. Aerospace and Electronic Systems*, vol. AES-26, pp. 146–153, January 1990.
48. W. W. Shrader, inventor, "Sensitivity Velocity Control," U.S. Patent 5,134,410, July 1992.
49. C. Rife and R. R. Boorstyn, "Single-tone parameter estimation from discrete-time observations," *IEEE Trans. Information Theory*, vol. IT-20, no. 5, pp. 591–598, September 1974.
50. D. R. A. McMahon and R. F. Barrett, "An efficient method for the estimation of the frequency of a single tone in noise from the phases of discrete Fourier transforms," *Signal Processing*, vol. 11, pp. 169–177, 1986.
51. J. W. Taylor, "Receivers," Chap. 3 in *Radar Handbook*, 2nd Ed., M. I. Skolnik (ed.), New York: McGraw-Hill, 1990, pp. 323–325.
52. J. Y. N. Cho et al., "Range-velocity ambiguity mitigation schemes for the enhanced terminal doppler weather radar," in *31st Conference on Radar Meteorology*, Seattle, WA, 2003, pp. 463–466.
53. W. W. Shrader, "Radar technology applied to air traffic control," *IEEE Trans. Communications*, vol. 21, no. 5, pp. 591–605, May 1973.
54. W. W. Shrader, "MTI radar," Chap. 17 in *Radar Handbook*, M. I. Skolnik (ed.), New York: McGraw-Hill, 1970, pp. 17–56.